UNIVERSITY OF OKLAHOMA

GRADUATE COLLEGE

EARTHQUAKE SOURCE AND RUPTURE CHARACTERIZATION FROM MICROEARTHQUAKES TO MEGATHRUST EARTHQUAKES

A DISSERTATION

SUBMITTED TO THE GRADUATE FACULTY

in partial fulfillment of the requirements for the

Degree of

DOCTOR OF PHILOSOPHY

By

COLIN NATHANAEL PENNINGTON

Norman, Oklahoma

2020

EARTHQUAKE SOURCE AND RUPTURE CHARACTERIZATION FROM MICROEARTHQUAKES TO MEGATHRUST EARTHQUAKES

A DISSERTATION APPROVED FOR THE
SCHOOL OF GEOSCIENCES

BY THE COMMITTEE CONSISTING OF

Dr. Xiaowei Chen, Chair

Dr. Brett Carpenter

Dr. Michael Behm

Dr. Jacob Walter

Dr. Ahmad Ghassemi

Acknowledgements

First, I wish to express my gratitude to my research advisor, Professor Xiaowei Chen, for teaching me so much about seismology, earthquakes, and providing me with numerous opportunities to collaborate with other researchers. Second, I wish thank some of my amazing collaborators, such as Rachel E. Abercrombie, Taka Uchide, and Qimin Wu. Through their comments, input and explanations I have been able to grow immensely as a scientist and as a seismologist and I look forward to collaborating with them more in the future.

Third I would like to thank the friends I have made during my time here at OU. Especialy, Yan Qin, Raymond Ng, Prahshu Ratre and Deepankar Dangwal to name a few. The evenings we spent playing board games, at festivals, and our trip to New Mexico were some of the highlights of my time here in Oklahoma.

Lastly and most importantly I wish to thank my parents. Without their support I would not be where I am today. I especially want to thank my Dad for listening to me talk about earthquakes and seismology so much. I know he probably does not understand half of it, but I appreciate him always being there to listen.

Some of the chapters presented in this thesis are reformatted version of papers that are in preparation for submission to journals. Chapter 2 is a completed manuscript that will be submitted to *Journal of Geophysical Research: Solid*

Earth. Chapter 1 is being prepared for submission to *Journal of Geophysical Research: Solid Earth*, but is also dependent on the aforementioned study. Chapter 4-5 are in preparation to be submitted to *Geophysical Research Letters*. In all cases I am the fist author with guidance provided by co-authors in these studies.

TABLE OF CONTENTS

LIST OF FIGURES

LIST OF TABLES

0.1 Abstract of the Dissertation

The understanding of earthquake rupture processes is vitally important to the proper estimation of hazard. I examine earthquake ruptures from megathrust earthquakes down to microquakes (≤ 3 magnitude) in order to better understand the role fault properties, prior seismicity, and injection play in controlling earthquake ruptures and if they change with magnitude.

In order to understand if the characterization of earthquake ruptures using source parameters such as stress drop, rupture size, and moment produce consistent interpretation no matter the method used to obtain them. To determine the effects of data selection and the method used to remove site and path effects have on source parameter estimates I examine the 2011 Prague earthquake sequence using a combined catalog of 5,446 earthquakes. From this analysis I find that the stress drop values will be systematically biased to a certain degree depending on how site and path effects are removed from the earthquakes waveform, and will also vary depending on the wave type used (P-wave, S-wave), and with the window length used to select the data. However, the normalized stress drop values are consistent, meaning that spatial and temporal interpretations of stress drops will be consistent across methods. Based upon this observation we interpret spatial patterns observed across all results and find that stress drops are affect by local fault structure and geology and the largest events slip distribution. These results suggest that source parameter interpretations can be interpreted reliably and reveal important information about fault systems, however in order to ensure that no method or data bias is included a second method of estimation should be used for verification.

To understand the controls on earthquake rupture and if they change across magnitude scales I perform 3 different types of analyses. Through the use of a finite slip inversion method I examine the slip distribution of a small Mw 4.1 earthquake in Guthrie Oklahoma and quantify its rupture by the number of slip patches that occur within it. To quantify the ruptures of large earthquakes I estimate their rupture complexity by the roughness of their Source Time Functions (STF), which represent an earthquake slip history in time, utilizing a global STF catalog. I examine microearthquake rupture using the high resolution borehole network along the Parkfield segment of the San Andreas fault. Microearthquake rupture complexity and simplicity is quantified in the frequency and time domain separately in order to examine if these observations agree. For each region and magnitude range examined I find ruptures that exhibit multiple phases in their slip history, which correlates to heterogeneity in the spatial distribution of slip on the rupture plans surface. The factors that are responsible for these more heterogeneous ruptures vary with region, but the ones that show the strongest effects are prior seismicity, heterogeneity in fault properties, and fault structure. The combination of the results from each of this separate analyses indicates that rupture complexity is not limited to large magnitude events, and the factors that control such ruptures for large magnitudes also control them for small and microearthquakes.

Chapter 1

Introduction

Earthquakes and their destructive effects are one of the great hazards that exist on Earth. They have been documented throughout human history with the earliest records dating back to 1177 B.C. As for the cause of earthquakes, the first attempt at a natural explanation for them came from Aristotle who postulated that winds within the earth whipped up the occasional shaking of the earth's surface (Missiakoulis, 2008; van Straaten, 1952; Lee, 1952). It was only in the 20th century that the connection between fault's and the buildup of stress on them was determined to be the cause. However, throughout the history of humankind one of the primary goals of the study of earthquakes has always been the mitigation of their damaging effects. Our ability to mitigate this risk is dependent on not only an understanding of the physical processes behind earthquakes that lead to their occurrence, but also on a deep knowledge of the rupture process.

Multi-scale fault zone systems contain earthquakes that rupture microscopic scale features and others whose ruptures extend 100s of kilometers. These large events exhibit a wide range of failure behavior, with some rupturing at velocities faster than S-wave velocities (Bao et al., 2019), others rupturing large stuck portions of faults (Miyazaki et al., 2012), and others unzipping entire fault lengths through the cascading failure of multiple fault segments (Yoshimoto & Yamanaka, 2014). These events are exceedingly rare so our study of these fault systems and of earthquake physics are often dependent on smaller events. These small events have been able to provide insight into fault geometry and time dependent properties of fault zones. However, our understanding of these small events and their study often utilize models that make many simplifying assumptions.

In the following chapters I will focus on characterizing earthquake source processes and ruptures across magnitude scales. I do this to understand if the ruptures of these small events (magnitudes ≤ 5) can accurately provide information on fault systems and if their ruptures are similar to those of large events. Chapter 2 will focus on the reliability of methods used to characterize small earthquakes source processes. Chapter 3 is centered around the estimation of source parameters for a M4.1 complex rupture and the information detailed source characterization can provide. Chapter 4 focuses on understanding the causes of complexity in large (>M6) earthquakes. Chapter 5 will quantify if microearthquakes exhibit similar behavior to large events. From these combined analysis I hope to quantify the reliability of source parameter estimates and their interpretation and deepen our understanding of the factors that contribute to and control earthquake ruptures.

1.1 Source Parameter Estimation of Small Earthquakes

Early in the study of small earthquakes, insufficient number of seismometers, poor azimuthal coverage, and the low sample rate of waveform recordings made it challenging to characterize smaller earthquake sources. Due to these challenges, deriving small earthquake source parameters relies on dynamic rupture models (e.g., Brune, 1970a; Madariaga, 1976) to link observable frequency effects observed in the recorded waveform to its rupture area and from there to an estimate of static stress drop ($\Delta\sigma$), which is the average stress change over entire rupture surface caused by the earthquake (Abercrombie, 1995; Ide, 2003; Prieto et al., 2004; Shearer et al., 2006; Allmann & Shearer, 2007, 2009; Sumy et al., 2014). From this link, thousands if not millions of earthquakes have had estimates of static stress drop ($\Delta\sigma$), based upon the expression derived by Eshelby (1957) for an elliptical crack in a homogeneous medium, and a similar expression specifically applied to earthquakes by Keylis-Borok (1958) (Figure 1.2). These equations take the form of:

$$\Delta\sigma = C(a, b, v)\frac{M_0}{bS} \tag{1.1}$$

where M_0 is the seismic moment, S is rupture area and C is a constant close to 1 that depends on the shape of the ellipse that has a major axis with a length of a and minor axis with a length of b and the Poisson ratio, v, of the medium. Equation 1.1 still requires us to know the major and minor axis lengths, of which determining the minor axis is extremely challenging. To avoid this Brune (1970b) and Madariaga (1976) adapted this equation to be for a circular rupture patch

($a = b$) instead of an ellipse ($b < a$) (Figure 1.2). These models allow for the direct connection of the rupture area to the observable average corner frequency f_c through the expression:

$$\Delta\sigma = \frac{7}{16}\frac{M_0}{a^3}, f_c = k\frac{\beta}{a} \tag{1.2}$$

where k is a constant that is specific to a particular dynamic model (e.g., Sato & Hirasawa, 1973; Boatwright, 1984; Abercrombie, 1995; Prieto et al., 2004; Abercrombie & Rice, 2005; Imanishi & Ellsworth, 2006; Kwiatek & Ben-Zion, 2013; Kaneko & Shearer, 2014). These crack models are inherently overly simplified and therefore inaccurate and were only intended to be used as a rough measure of the true value. Now another important feature in equation 1.2 is that the area a is cubed. This means that a relatively small error in f_c like a factor of 2 (e.g. f_c of 2 vs 4 Hz) will result in an order of magnitude difference in stress drop estimate. The fitting of a model to real data will always produce some inherent uncertainty in f_c measurement, and due to assumptions of the models this is amplified by stress drop. If we do not use spectra and instead constrain the rupture geometry using another method such as using variation in the rupture duration with azimuth to invert for a elliptical source models length and width can dramatically decrease the the scatter of static stress-drop estimates(Boatwright, 1984). The problem is that such methods can rarely be applied to magnitudes smaller than 6.

Chapter 2 focuses on the reliability of f_c and $\Delta\sigma$ estimates from different methods. We demonstrate in the case study of the Prague 2011 earthquake sequence that, the absolute $\Delta\sigma$ values will vary by method or data type. Notably, though, if strict data quality requirements are used the relative differences between individual events stays consistent.

1.2 Estimating Source Parameters for Non-Simple Events

The source parameter estimates described above (e.g. stress drop, moment, rupture area, and corner frequency) and their accuracy all depend on the assumption that the events do not have complicated source processes. It is well understood that large earthquakes have complicated source processes, such as rupturing unilaterally, and this causes them to deviate from the simple circular model (McGuire et al., 2002; Atkinson & Silva, 1997; Schneider et al., 1993; Silva et al., 1998). The deviation from a circular model can happen for many reasons and include if an earthquake has a rectangular rupture instead of a circular rupture (Savage, 1972), a partial stress drop (Brune, 1970a), fault "roughness" (Gusev, 1983), barriers that slow or segment a rupture (Papageorgiou & Aki, 1984), multiple asperities failing during a rupture (S. H. Hartzell & Brune, 1979), or a preslip region failing around a strong asperity (Johnson & Nadeau, 2002, 2005).

Estimates made of stress drop, rupture area, or average slip made from a simple circular model will not be accurate if the event has a "complex" rupture that deviates from the simple circular model for any reason. To properly examine these complex ruptures other methods are required. The most widely known method for accurately describing a complex earthquakes rupture is by performing a Finite Fault slip inversion, which was first introduced by Haskell (Haskell, 1964). The spatio-temporal slip distribution on a fault plane is resolved by first dividing the fault plane into $M \times N$ sub-faults with length Δx and width Δy. The slip history on each subfault is described by a series of L triangle functions with rise time τ (Figure 1.3). Based upon this source model the synthetic seismic waveform generated for station j can be expressed by

$$W_j^{\mathrm{syn}}(t_i) = \textstyle\sum_{mnl} X_{mnl} g_{mnj}(t_i - (l-1)\tau - T_{mn}) + e_j, \tag{1.3}$$

where X_{mnl} is the slip at the mn^{th} subfault at the l^{th} timestep. $g_{mnj}(t)$ is the Green's function a point source at the mn^{th} subfault with a t_i being the sample point of the EGF waveform that aligns with l^{th} timestep. T_{mn} is the start time of the basis function at each subfault; e_j is assumed to be the Gaussian error with variance of σ_j. The slip distribution is solved for by minimizing the misfit between the predicted waveform and observed waveform for all stations. The Greens Function used in the inversion can either be synthetic or an empirical Green's Function (EGF) (S. Hartzell, 1978). The resolution of these models depends on the frequency range of the recorded waveform, and grid spacing on the fault. A majority of finite fault models utilize synthetic Green's functions, which are limited in frequency range and therefore limit their usage to large megathrust earthquakes. To resolve the slip of small events the EGF method is required, but even these results are often limited to magnitude 5 or above with only a few studies examining small earthquakes <4M (Dreger et al., 2007; Uchide & Ide, 2010). From these resolved slip models source parameters can be estimated, and these parameters are often considered to be better resolved than those obtained through those obtained from fitting an events spectra with a model. It should be noted though that such inversions often disagree with one another depending upon which data is utilized (e.g. teleseismic waveforms, strong motion, GPS, and InSAR) (Mai et al., 2016). Their parameters often disagree as much as the ones obtained from fitting an earthquakes spectra.

In Chapter 3, I focus on a Mw 4.1 2015 Guthrie, Oklahoma earthquake, which occurred in a swarm like sequence. Through the use of finite fault modeling I obtain the slip distribution of this event and compare it to other earthquakes of similar sizes in other swarm like sequences. Doing this I am able to quantify the heterogeneity of stress, geologic properties, and fault geometry in different regions have direct impacts on how earthquake ruptures manifest and grow.

1.3 What Controls Rupture Complexity?

There are many factors that can affect earthquake rupture and cause it to have multiple phases of slip, or heterogeneous rupture area making it complex compare to ruptures assumed to have more homogeneous slip distribution. Faults are complex structures, which exhibit geometrical complexity and heterogeneity on a variety of scales. This complexity as well as the surface roughness along a fault affect the dynamic stress perturbation induced during earthquake slip, which can lead to significant changes in earthquake nucleation and propagation (Chester & Chester, 2000; Campillo et al., 2001; Dieterich & Smith, 2009; Griffith et al., 2010). The effect of lithology and structure on inter-patch triggering during rupture was recently explored by Ye et al. (2018). In the study, they quantified megathrust earthquakes by the number of slip patches triggered during their respective ruptures. The hypothesis is that when a slip-patch fails, it produces a separate slip pulse, which appears as sub-event in the Source Time Function (STF), so complexity in the STF represents complexity in the rupture process. They used two separate parameters to quantify the complexity: radiated energy enhancement factor (REEF) based on radiated energy (i.e., including high-frequency energy radiation) and STF roughness (i.e., relatively smoothed and lower frequency). In their proposed framework, the simple events (low REEF and roughness) tend to occur within regions with more spatially uniform coupling along faults surfaces, while the complex ones (high REEF and roughness) tend to occur in regions with strong spatial heterogeneity of intrinsic coupling. Faulting regime also appears to have a strong effect on rupture complexity: strike-slip faulting events produced complex ruptures more often than other types of faulting (Danré et al., 2019).

In Chapter 4, I expand the analysis of Ye et al. (2018) by applying the REEF method to a Source Time Function catalog (SCARDEC) (Vallée & Douet, 2016) of large events across the world. From the results of this analysis I find that complexity varies with faulting regime, depth, and region. I find that strike-slip events are more often complex compared to other faulting regimes. Like Ye et al. (2018) I find that regions often exhibit a consistent style of failure. I observe an increase in normal faulting earthquake complexity with depth supporting previous observations (Houston et al., 1998; Persh & Houston, 2004). For strike-slip events I find faults in different regions tend to consistently display complex or simple failure indicating that geology and fault structure may strongly control rupture complexity.

1.4 Which Earthquakes are Complex?

The above observations are not limited to just large magnitude earthquakes. Wang et al. (2014) found many microearthquakes in Northern California to have STF's that contained a second subevent. These subevents often occurred to the SE direction and were hypothesized to be caused by the bi-material effect in Northern California. The observation of possible complex ruptures in small earthquakes is also supported by Uchide and Imanishi (2016), who found that 3-4.5M earthquakes in Japan deviated from the model of Brune (Brune, 1970a). These two forms of complexity were linked by Wu et al. (2019) who found that event's that exhibit STF complexity also exhibit spectral complexity. What remains unquantified is to what degree these two observations match over large populations. We also still do not know the ratio of simple to complex events for small magnitudes and if what controls their complexity is the same as large events.

In Chapter 5, I try to better understand the link between these two types of complexity and if the causes of small earthquake complexity are similar to those of large magnitudes. To do this, I examine the Parkfield segment of the San Andreas Fault and earthquakes that occur along it from 2001-2011 using the high-resolution borehole network and determine the ratio of simple to complex events for small magnitude events. I quantify the complexity of earthquakes in the frequency and time domain. From this analysis, I find that for >M2.5 earthquake that occur in regions with good azimuthal station coverage I find a high level of rupture complexity (80%). These observations are consistent across methods. I also observe regions of the fault exhibit a preference towards producing simple or complex rupture, which aligns with previously observed stress and geologic heterogeneity.

1.5 Summary and Structure

To summarize the objectives for each chapter and section:

- **Chapter 2**: *Source parameter estimates exhibit high level of disagreement, can we trust their interpretation?* The examination of the reliability of estimates for the 2011 Prague earthquake sequence using multiple data types and methods. This chapter is currently in prep for submission. Pennington, C., Chen, X., Abercrombie, R., McMahon, N.,(2020). Reliability of Source Parameter Estimation and Interpretation Across Methods: 2011 Prague, Oklahoma Earthquake Sequence. *Geophysical Research: Solid Earth*(In Prep)

- **Chapter 3**: *Does the interpretation of small magnitude event complexity matter?* Through the examination of the Mw 4.1 Guthrie earthquake I am able to quantify how faults in Oklahoma exhibit higher levels of stress heterogeneity compared to other regions. Pennington, C., Uchide, T., Chen, X., (2020). Finite Fault Inversion of Mw4.1 and its Implications for Induced Earthquake Ruptures. *Geophysical Research: Solid Earth*(In Prep)

- **Chapter 4**: *What controls the complexity of large magnitude events?* Using the STF of large magnitude events, I interpret that rupture complexity is controlled by geologic factors, earthquake depth, and faulting regime. This chapter is currently in prep for submission. Pennington, C., Chen, X., (2020). Control Factors of Earthquake Rupture Complexity from a Global Perspective. *Geophysical Research Letters.*(In Prep)

- **Chapter 5**: *Do small earthquakes exhibit the same level of complexity as large magnitude events?* Through the examination of the earthquakes along the Parkfield segment of the San Andreas fault, I find that small events exhibit high levels of complexity just like large magnitude events. This chapter is currently in prep for submission. Pennington, C., Chen, X.,

Wu, Q., Zhang, J. (2020). Quantifying Rupture Characteristics of Microearthquakes in the Parkfield Region Using a High-Resolution Borehole Network. *Geophysical Research Letters.*

References

Abercrombie, R. (1995). earthquake source scaling relationships from -1 to 5 Ml using seismograms recorded at 2.5-km depth. *J. Geophys. Res.*, *100*(B12), 24015–24036.

Abercrombie, R., & Rice, J. (2005, 8). Can observations of earthquake scaling constrain slip weakening? *Geophysical Journal International*, *162*(2), 406–424. Retrieved from `https://academic.oup.com/gji/article-lookup/doi/10.1111/j.1365-246X.2005.02579.x` doi: 10.1111/j.1365-246X.2005.02579.x

Allmann, B. P., & Shearer, P. M. (2007). A high-frequency secondary event during the 2004 Parkfield earthquake. *Science*, *318*(5854), 1279–1283. doi: 10.1126/science.1146537

Allmann, B. P., & Shearer, P. M. (2009, 1). Global variations of stress drop for moderate to large earthquakes. *Journal of Geophysical Research*, *114*(B1), B01310. Retrieved from `http://doi.wiley.com/10.1029/2008JB005821` doi: 10.1029/2008JB005821

Atkinson, G. M., & Silva, W. (1997). An empirical study of earthquake source spectra for California earthquakes. *Bulletin of the Seismological Society of America*, *87*(1), 97–113.

Bao, H., Ampuero, J.-P., Meng, L., Fielding, E. J., Liang, C., Milliner, C. W. D., ... Huang, H. (2019, 3). Early and persistent supershear rupture of the 2018 magnitude 7.5 Palu earthquake. *Nature Geoscience*, *12*(3), 200–205. doi: 10.1038/s41561-018-0297-z

Boatwright, J. (1984). Seismic estimates of stress release. *J. Geophys. Res.*, *89*(B8), 6961–6968.

Brune, J. N. (1970a, 9). Tectonic stress and the spectra of seismic shear waves from earthquakes. *Journal of Geophysical Research*, *75*(26), 4997–5009. Retrieved from `http://doi.wiley.com/10.1029/JB075i026p04997` doi: 10.1029/JB075i026p04997

Brune, J. N. (1970b, 9). Tectonic stress and the spectra of seismic shear waves from earthquakes. *J. Geophys. Res.*, *75*(26), 4997–5009. Retrieved from `http://doi.wiley.com/10.1029/JB075i026p04997` doi: 10.1029/JB075i026p04997

Campillo, M., Favreau, P., Ionescu, I. R., & Voisin, C. (2001). On the effective friction law of a heterogeneous fault. *Journal of Geophysical Research: Solid Earth*. doi: 10.1029/2000jb900467

Chester, F. M., & Chester, J. S. (2000). Stress and deformation along wavy frictional faults. *Journal of Geophysical Research: Solid Earth*. doi: 10.1029/2000jb900241

Danré, P., Yin, J., Lipovsky, B. P., & Denolle, M. A. (2019). Earthquakes Within Earthquakes: Patterns in Rupture Complexity. *Geophysical Research Letters*, *46*(13), 7352–7360. doi: 10.1029/2019GL083093

Dieterich, J. H., & Smith, D. E. (2009). Nonplanar faults: Mechanics of slip and off-fault damage. *Pure and Applied Geophysics*. doi: 10.1007/s00024-009-0517-y

Dreger, D., Nadeau, R. M., & Chung, A. (2007). Repeating earthquake finite source models: Strong asperities revealed on the San Andreas fault. *Geophysical Research Letters*, *34*(23), 1–5. doi: 10.1029/2007GL031353

Eshelby, J. D. (1957). The determination of the elastic field of an ellipsoidal inclusion, and related problems. *Proc. R. Soc. London, Ser. A,*, *241*, 376–396.

Griffith, W. A., Nielsen, S., Di Toro, G., & Smith, S. A. (2010). Rough faults, distributed weakening, and off-fault deformation. *Journal of Geophysical Research: Solid Earth*. doi: 10.1029/2009JB006925

Gusev, A. A. (1983). Descriptive statistical model of earthquake source radiation and its application to an estimation of short-period strong motion. *Geophysical Journal of the Royal Astronomical Society*, *74*(3), 787–808. doi: 10.1111/j.1365-246X.1983.tb01904.x

Hartzell, S. (1978, 1). Earthquake aftershocks as Green's functions. *Geophysical Research Letters*, *5*(1), 1–4. doi: 10.1029/GL005i001p00001

Hartzell, S. H., & Brune, J. N. (1979). The horse canyon earthquake of August 2, 1975—Two-stage stress-release process in a strike-slip earthquake. *Bulletin - Seismological Society of America*, *69*(4), 1161–1173.

Haskell, N. A. (1964). Total energy and energy spectral density of elastic wave radiation from propagating faults the Seismological Society of America. *Bulletin of the Seismological Society of America*.

Houston, H., Benz, H. M., & Vidale, J. E. (1998). Time functions of deep earthquakes from broadband and short-period stacks. *Journal of Geophysical Research: Solid Earth*. doi: 10.1029/98jb02135

Ide, S. (2003). Fracture surface energy of natural earthquakes from the viewpoint of seismic observations. *Bull. Earthq. Res. Inst.*, *78*, 59–65.

Imanishi, K., & Ellsworth, W. L. (2006). Source scaling relationships of microearthquakes at Parkfield, CA, determined using the SAFOD Pilot Hole Seismic Array. *Earthquakes: Radiated Energy and the Physics of Faulting, Geophys. Monogr. Ser.,*, *170*, 81–90. doi: 10.1029/170GM10

Johnson, L. R., & Nadeau, R. M. (2002). Asperity model of an earthquake:

Static Problem. *Bulletin of the Seismological Society of America*, *92*(2), 672–686.

Johnson, L. R., & Nadeau, R. M. (2005). Asperity model of an earthquake: Dynamic problem. *Bulletin of the Seismological Society of America*, *95*(1), 75–108. doi: 10.1785/0120030093

Kaneko, Y., & Shearer, P. M. (2014). Seismic source spectra and estimated stress drop derived from cohesive-zone models for circular subshear rupture. *Geophys. J. Int.*. doi: 10.1093/gji/ggu030

Keylis-Borok, V. (1958). On estimation of the displacement in an earthquake source and of source dimensions. *Annals of Geophysics*. doi: 10.4401/ag-4596

Kwiatek, G., & Ben-Zion, Y. (2013). Assessment of P and S wave energy radiated from very small shear-tensile seismic events in a deep South African mine. *Journal of Geophysical Research: Solid Earth*, *118*(7), 3630–3641. doi: 10.1002/jgrb.50274

Lee, H. D. P. (1952). Aristotle VII Meteorologica. *Harvard Univ. Press*.

Madariaga, R. (1976). Dynamics of an expanding circular fault. *Bull. Seismol. Soc. Am.*, *66*(3), 639–666.

Mai, P. M., Schorlemmer, D., Page, M., Ampuero, J., Asano, K., Causse, M., . . . Zielke, O. (2016). The Earthquake-Source Inversion Validation (SIV) Project. *Seismological Research Letters*, *87*(3), 690–708. Retrieved from `http://srl.geoscienceworld.org/lookup/doi/10.1785/0220150231` doi: 10.1785/0220150231

McGuire, J. L., Zhao, L., & Jordan, T. H. (2002). Predominance of unilateral rupture for a global catalog of large earthquake. *Bulletin of the Seismological Society of America*, *92*(8), 3309–3317. doi: 10.1785/0120010293

Missiakoulis, S. (2008). Aristotle and earthquake data: A historical note. *International Statistical Review*. doi: 10.1111/j.1751-5823.2007.00040.x

Miyazaki, S., McGuire, J. J., & Segall, P. (2012). Seismic and aseismic fault slip before and during the 2011 off the Pacific coast of Tohoku Earthquake. *Earth Planets and Space*, *63*(7), 637–642. doi: 10.5047/eps.2011.07.001

Papageorgiou, A. S., & Aki, K. (1984, 12). Specific barrier model for the quantitative description of inhomogeneous faulting and the prediction of strong ground motion. Part 2. Applications of the model. *International Journal of Rock Mechanics and Mining Sciences & Geomechanics Abstracts*, *21*(6), 221. Retrieved from `https://linkinghub.elsevier.com/retrieve/pii/014890628490500X` doi: 10.1016/0148-9062(84)90500-X

Persh, S. E., & Houston, H. (2004). Deep earthquake rupture histories determined by global stacking of broadband P waveforms. *Journal of Geophysical Research: Solid Earth*. doi: 10.1029/2003JB002762

Prieto, G., Shearer, P., Vernon, F., & Kilb, D. (2004). Earthquake source scaling and self-similarity estimation from stacking P and S spectra. *J. Geo-*

phys. Res., *109*(8), 1–13. Retrieved from `http://dx.doi.org/10.1029/2004JB003084` doi: 10.1029/2004jb003084

Sato, T., & Hirasawa, T. (1973). Body wave spectra from propagating shear cracks. *Journal of Physics of the Earth*, *21*(4), 415–431. doi: 10.4294/jpe1952.21.415

Savage, J. C. (1972). Relation of corner frequency to fault dimensions. *Journal of Geophysical Research*. doi: 10.1029/jb077i020p03788

Schneider, J. F., Silva, W. J., & Stark, C. (1993). Ground Motion Model for the 1989 M 6.9 Loma Prieta Earthquake Including Effects of Source, Path, and Site. *Earthquake Spectra*. doi: 10.1193/1.1585715

Shearer, P. M., Prieto, G. A., & Hauksson, E. (2006). Comprehensive analysis of earthquake spectral in southern California. *Journal of Geophysical Research-Solid Earth*, *111*(B6). doi: B0630310.1029/2005jb003979

Silva, W. J., Wong, I. G., & Darragh, R. B. (1998). Engineering characterization of earthquake strong ground motions in the Pacific Northwest. *US Geological Survey Professional Paper*.

Sumy, D. F., Cochran, E. S., Keranen, K. M., Wei, M., & Abers, G. A. (2014, 3). Observations of static Coulomb stress triggering of the November 2011 M 5.7 Oklahoma earthquake sequence. *Journal of Geophysical Research: Solid Earth*, *119*(3), 1904–1923. doi: 10.1002/2013JB010612

Tan, O., & Taymaz, T. (2006). Active tectonics of the Caucasus: Earthquake source mechanisms and rupture histories obtained from inversion of teleseismic body waveforms. *Special Paper of the Geological Society of America*. doi: 10.1130/2006.2409(25)

Uchide, T., & Ide, S. (2010). Scaling of earthquake rupture growth in the Parkfield area: Self-similar growth and suppression by the finite seismogenic layer. *Journal of Geophysical Research: Solid Earth*, *115*(11), 1–15. doi: 10.1029/2009JB007122

Uchide, T., & Imanishi, K. (2016). Small earthquakes deviate from the omega-square model as revealed by multiple spectral ratio analysis. *Bulletin of the Seismological Society of America*, *106*(3), 1357–1363. doi: 10.1785/0120150322

Vallée, M., & Douet, V. (2016). A new database of source time functions (STFs) extracted from the SCARDEC method. *Physics of the Earth and Planetary Interiors*, *257*, 149–157. doi: 10.1016/j.pepi.2016.05.012

van Straaten, M. (1952, 1). De Mundo. In *Panaetius rhodius* (pp. 19–25). BRILL. Retrieved from `https://brill.com/view/book/9789004320178/B9789004320178-s005.xml` doi: 10.1163/9789004320178{_}005

Wang, E., Rubin, A. M., & Ampuero, J.-P. (2014, 5). Compound earthquakes on a bimaterial interface and implications for rupture mechanics. *Geophysical Journal International*, *197*(2), 1138–1153. Retrieved from `http://academic.oup.com/gji/article/197/2/1138/`

`620011/Compound-earthquakes-on-a-bimaterial-interface-and` doi: 10.1093/gji/ggu047

Wu, Q., Chen, X., & Abercrombie, R. E. (2019). Source Complexity of the 2015 Mw 4.0 Guthrie, Oklahoma Earthquake. *Geophysical Research Letters*, *46*(9), 4674–4684. doi: 10.1029/2019GL082690

Ye, L., Kanamori, H., & Lay, T. (2018). Global variations of large megathrust earthquake rupture characteristics. *Science Advances*, *4*(3), 1–8. doi: 10.1126/sciadv.aao4915

Yoshimoto, M., & Yamanaka, Y. (2014). Teleseismic inversion of the 2004 Sumatra-Andaman earthquake rupture process using complete Green's functions. *International Aquatic Research*, *66*(1), 1–8. doi: 10.1186/s40623-014-0152-4

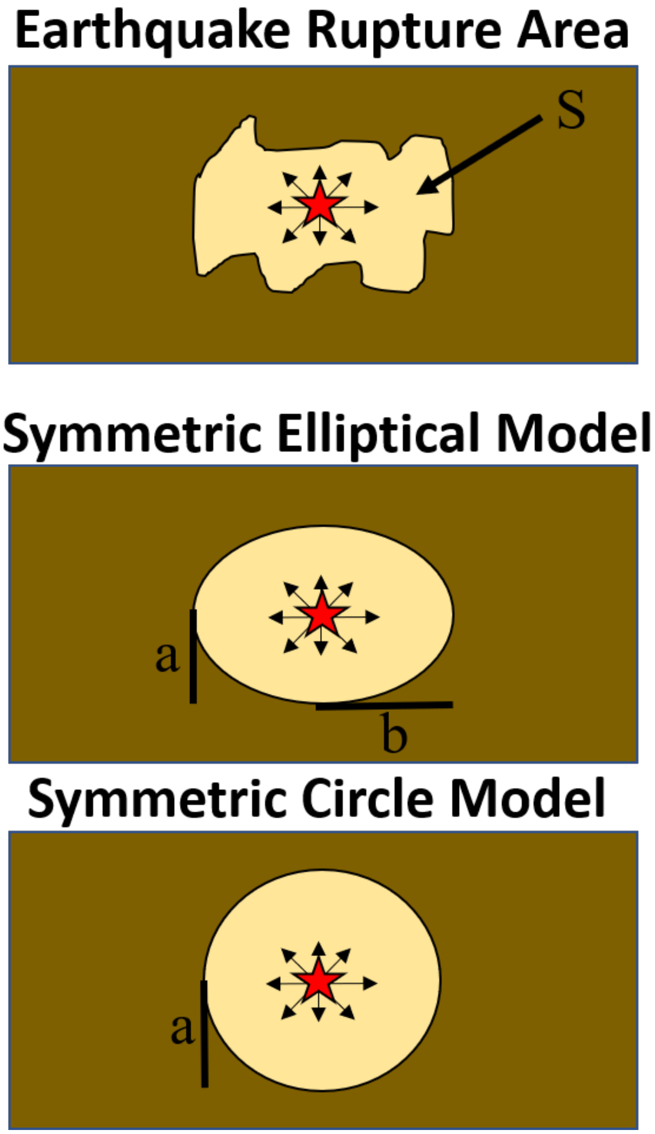

Figure 1.1: Examples of the models used to represent a earthquakes rupture. A theoretical earthquakes rupture (top) and its elliptical models representation (middle) and its circular rupture model representation (bottom).

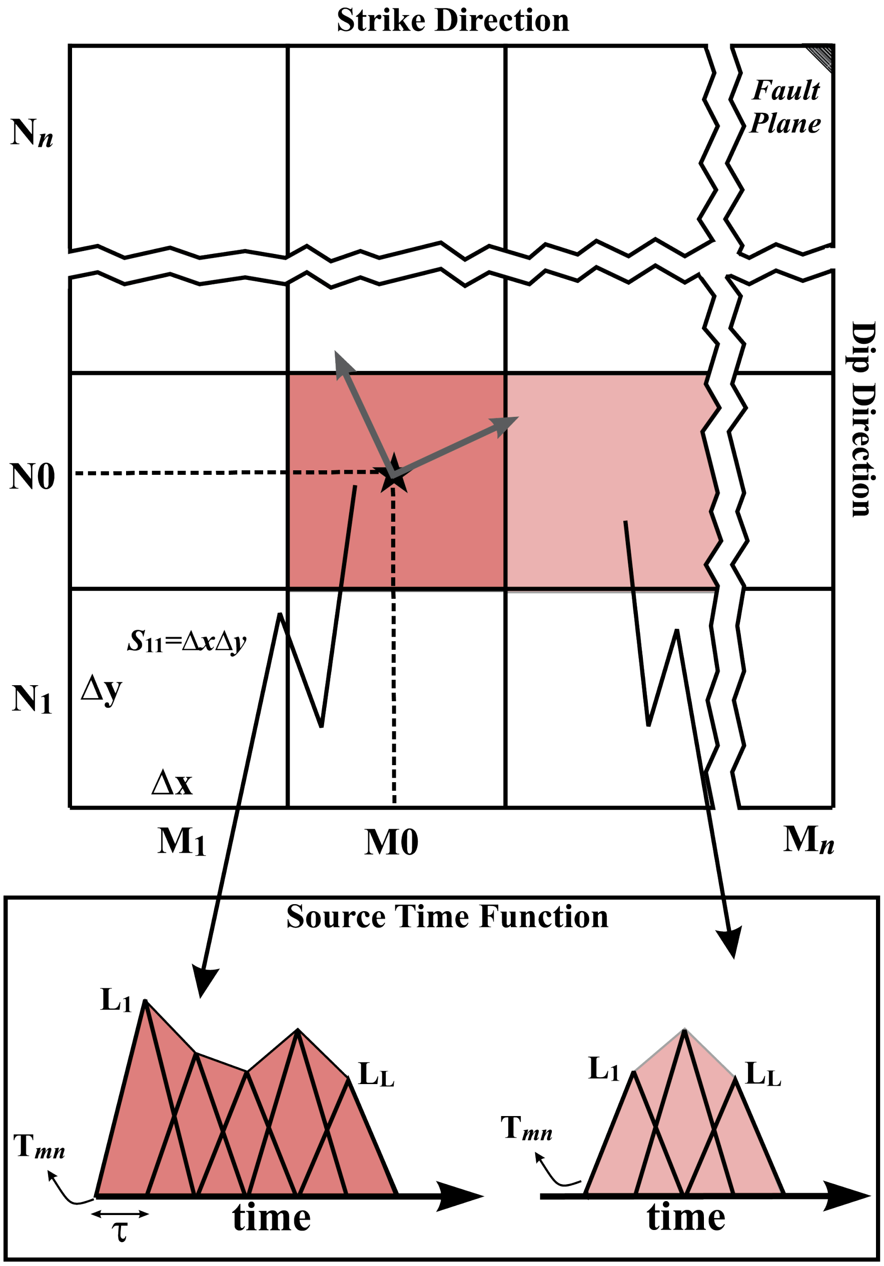

Figure 1.2: Parameterization of fault area used in slip distribution inversion. The star represents the initiation point of the rupture propagation. The rupture in each cell begins after T_{mn} time delay, which is depends on when the rupture reaches the cell based upon a constant rupture velocity. The Source Time Function for each cell is defined by L isosceles triangles. Figure Modified from Tan and Taymaz (2006)

.

Chapter 2

Reliability of Source Parameter Estimation and Interpretation Across Methods: 2011 Prague, Oklahoma Earthquake Sequence

2.1 Abstract

Earthquake source parameters provide insight into the processes occurring during earthquake rupture however, measurements for these parameters can vary. Such variance makes the interpretation of these values difficult and if these variations are due to method or data selection can have a direct impact on interpretations. The 2011 Prague earthquake is a prime example of this, where its source parameters have been interpreted to show the effects of injection. We examine the Prague earthquake sequence using single coherent catalog for all the events detected by Oklahoma Geologic Survey (OGS) and McMahon et al. (2017). We

use three principal approaches to estimate stress drop in order to understand the biases of each: a spectral decomposition method based on stacking, individual direct spectral fitting, and spectral ratio method based on individual event pairs. When comparing our results with previous studies for the Prague sequence, we find that the absolute values of stress drop often shift due to method, but that the relative patterns remain consistent. The only instances this does not hold is when low quality data is included. We interpret all methods results and observe that across them stress drops are dependent on the faults they occur on and are affected by past slip on fault. These results indicate that fault structure as well as past events play an important role in stress drop patterns.

2.2 Introduction

Earthquake source parameters provide important insight into the physical source processes occurring during earthquake rupture. The increase in seismicity rate within the central U.S. related to wastewater disposal from oil and gas production (Langenbruch & Zoback, 2016; Zhai et al., 2019) has led to a number of studies attempting to determine whether the source parameters of these induced earthquakes differ from those of tectonic earthquakes. Such a finding could allow for the identification of induced events from tectonic events within a sequence and would have important implications for the level of ground shaking to expect from induced events. The 2011 M5.7 Prague OK earthquake was the first large earthquake linked to the increase in wastewater injection (Keranen et al., 2013). Consequently, this earthquake sequence has been the subject of numerous source parameter studies aimed at resolving any differences between induced and tectonic earthquake sources.

Five high-volume wells injected in total 1.2e7 m^3 of wastewater into the Arbuckle formation in the area surrounding the Prague sequence (Figure 2.1) and their combined impact may have induced a Mw 4.8 earthquake on November 5, 2011 (Keranen et al., 2013; McGarr, 2014). Less than 24 hours later the combined effects of the movement of fluid through the Willzetta fault system and the positive Coulomb stress change due the M4.8 foreshock then triggered the largest event in the sequence a Mw 5.7 earthquake (Sumy et al., 2014; Norbeck & Horne, 2016). This event was then followed 2 days later by a Mw 4.8 aftershock that ruptured a previously unknown fault. The lower magnitude seismicity that followed these events is in both the crystalline basement and in the sedimentary layers above it (McMahon et al., 2017). This makes the Prague sequence unusual since most seismicity in Oklahoma occurs 2 to 5 km below the top of the basement (Mcnamara et al., 2015; Schoenball & Ellsworth, 2017).

Due to the potential of the sequence to reveal differences between induced and tectonic earthquake source parameters, as well as the intensity of shaking that could be expected from induced events, it has been the subject of 5 different source parameter studies (Yenier et al., 2017; Sumy et al., 2017; Wu et al., 2018; Boyd et al., 2017; Y. Huang et al., 2017). The prime focus of these studies was the estimation of stress drop, an estimate of stress released by the earthquake, since it directly links the high frequency radiation to strong ground motion (e.g., Baltay et al., 2019). These studies reached very different conclusions on the dependence of stress drop on triggering mechanism, some finding low stress drops (e.g., Sumy et al., 2017), while others did not (e.g., Boyd et al., 2017; H.-H. Huang et al., 2017). When comparing stress drop values from the various studies the difference between estimates for common events can be as great as 1-2 orders of magnitude for a sequence that is less than 20 km in length. The wide variations in estimates of stress drops for single events places any interpretation based upon them in considerable doubt.

The cause for such variation in estimates between studies could be due to many factors, since source parameter estimation is often subject to significant uncertainties (Abercrombie & Rice, 2005; Prieto et al., 2006; Kaneko & Shearer, 2015; Abercrombie, 2015). These uncertainties can lead to biases in interpretations, such as scaling relationships, and spatiotemporal changes (Abercrombie, 2014; Ide et al., 2011; Shearer et al., 2019). Differing interpretations for the same data set in the past has been attributed to differences in the data selection or the method used (e.g., Abercrombie, 2013; Baltay et al., 2010). These differences are probably the cause of the wide variations of source parameter estimate for the same events in the Prague sequence. What is not understood is whether such variation in observations is systematic or random, because it is difficult to separate the variations due to method from the natural variation due to geology or triggering process.

In this study, we attempt to separate the systematic effects of the applied method from those effects due to geology, and injection. We start by obtaining a single coherent catalog for all the events detected by Oklahoma Geological Survey (OGS) and McMahon et al. (2017). We relocate all these events and consider local geologic structure to determine the geometry of individual seismogenic faults. We then examine the spatial and temporal variations of stress drops observed on these different faults. We use three principal approaches to estimate stress drop in order to understand the biases of each: a spectral decomposition method based on stacking, individual direct spectral fitting, and spectral ratio method based on individual event pairs. We compare our results with previous studies for the Prague sequence, to distinguish between real stress drop variation and method-dependent effects, and hence investigate the seismogenic processes of the sequence. We first focus on the smaller earthquakes recorded by the temporary stations. Then also consider the largest events recorded by the regional network. Through this analysis we find that when the dataset is consistent, different methods can obtain similar results. Observations of depth dependence, magnitude dependence, relative patterns and interpretations are consistent across them. Based upon these findings we interpret the spatiotemporal patterns present in the Prague sequence.

2.3 Data

To construct a detailed view of the seismicity at Prague, we need a catalog of earthquakes that accurately captures the seismicity on distinct faults and in specific geologic units. To do this we combine the Oklahoma Geological Survey (OGS) earthquake catalog (742 earthquakes magnitude completeness M2.4 from 2010 to 2016) and the subspace-detected catalog from McMahon et al. (2017) (5,446 earthquakes magnitude completeness M-0.8 from November 4, 2011 to December 4, 2011). This merged catalog of 6,399 events contains only earthquakes that fall within the area of 35.4° to 35.6° latitude and -96.9° to -96.7° longitude. The sub-space catalog only has S-arrivals, so we pick the P-arrival using the phase picker of Li and Peng (2016) and the 1D velocity model from Keranen et al. (2013). Both P-wave and S-wave picks are later refined by clustering highly correlated waveforms at each station and picking the stack waveform of clustered events using the PphasePicker (Kalkan, 2016).

The network we use in this analysis was primarily deployed in the week that followed the Mw 4.8 foreshock. During this time period 31 continuously recording, three-component seismometers were deployed around the sequence. These instruments came from the Program for Array Seismic Studies of the Continental Lithosphere (PASSCAL), Rapid Array Mobilization Program (RAMP), the University of Oklahoma (OU), and the United States Geological Survey (USGS) (Sumy et al., 2014). For the examination of the small magnitude events, we use stations with a sampling rate of 250HZ (LC stations from OU and OKR stations from USGS) for a total of 23 stations available for certain time periods of the aftershock sequence. For the largest events ($M \geq 4.5$) in the sequence we also use the lower sampling rate seven EarthScope Transportable Array (TA) stations and USGS NetQuakes accelerometers that are only triggered by M>3.0 earthquakes.

2.4 Relocation and Seismogenic Faults

We relocate the earthquakes in the combined catalog using both the catalog phase pick derived differential times and cross-correlation differential times, for P and S-waves at 250 Hz sampling rate stations within 100 km of the sequence (Figure 2.1) using HypoDD (Waldhauser & Ellsworth, 2000). The cross-correlation differential times were obtained through the cross-correlation of all events based upon a time window of 0.5 seconds before and 1.3 second after the picked arrival time for the LC and OKR stations . Due to the low magnitude of most events in the catalog, we bandpass filter the waveforms between 3 and 20 Hz before cross-correlation. Only differential times of pairs with a cross correlation coefficient ≥ 0.7 are used in the relocation. The relocation was performed using the velocity model of Keranen et al. (2013) but modified to contain the finer shallow velocity structure obtained from well logs detailed in Isken and Mooney (2017) (Figure 2.2 a).

We obtain new location estimates for 5109 earthquakes. To estimate relative location errors, we apply a bootstrap approach for which the phase pick and correlation differential travel times are randomly resampled 200 times. For each earthquake, the location error is defined as the 80% of the 200 estimates of absolute location change between the bootstrap resampled location and the final location. 80% of the earthquakes in the relocated catalog have relocation errors of ±0.22 km vertically and ±0.07 km horizontally or less (Figure 2.2 b).

To determine if the seismicity is occurring in the crystalline basement or in the sedimentary layers above, we need an accurate depth for the top of the basement across the region. A single value would be inaccurate due to the offset that occurs at the Willzetta fault (Way, 1983). To obtain an accurate depth surface we create surface maps of the depth to the top of the Arbuckle and Hunton formations from well logs and electrical logs using the ArcGIS ordinary Kriging geoprocessing tool. These two formations are chosen because they are the ones primarily used for wastewater disposal in the Prague area (Keranen et al., 2013). The surface is created using 3235 measurements of the Hunton formation (Figure 2.3 a) and 76 of the Arbuckle formation that fall within the range of 35.23° to 35.64° latitude and -97.02° to -96.51° longitude (Figure 2.3 b). The location of the top of basement is less certain, and we constrain it by assuming that the Arbuckle has a roughly uniform thickness across the study region. It is located at 2.6 km depth in the NE and 2.8 km depth in the SW (Figure 2.1 d).In contrast previous interpolated isopach maps of the top of basement indicate little offset across the Willzetta fault with in the study area, which is likely due to limited number of basement top well measurments (Crain & Chang, 2018)

Based on the relocation performed in this study, and previous relocation studies (Sumy et al., 2014; Cochran et al., 2020) the fault system is composed primarily of 3 main fault segments, each associated with one of the three large events (Figure 2.1 a). The fault segment that hosted the M4.8 foreshock is part of the original Willzeta fault system (denoted as FF). The fault that hosted a majority of events was activated by the M5.7 mainshock (denoted as MF). The fault on which the M4.8 aftershock occurred is oriented E-W (denoted as AF). Only the MF is optimally oriented for failure based upon stress orientation, while the E-W and FF are 30 and 25 degrees off from optimal orientation (Cochran et al., 2020). Many events that occurred within the shallow sedimentary layers are located along the MF, therefore, we separate MF into basement (BMF) and sediment (SMF) segments (Figure 2.1d).

2.5 Spectral Analysis

We use three different approaches to estimate the stress drops of the earthquakes in the Prague sequence, which allows us to distinguish between method-dependent variability and real differences among events. These methods are the (1) a spectral decomposition method based on stacking (referred as "SNSS"), (2) individual spectral direct spectral fitting (referred to as "JS"), and (3) spectral ratio method based on individual event pairs (referred to as "SR") (Chen & Abercrombie, 2020; Abercrombie et al., 2017).

Each of these methods is focused on the accurate retrieval of the signal produced by the earthquake, also known as the source term ($E(t)$). This can be difficult, because the instrumental recorded ground motion is the convolution of the source term ($E(t)$), propagation term ($P(t)$), and site response term ($S(t)$):

$$D(t) = E(t) * P(t) * S(t) \tag{2.1}$$

In the frequency domain, the convolution can be simplified to multiplication of the event spectrum ($E(f)$), propagation spectrum ($P(f)$), and site spectrum ($S(f)$):

$$D(f) = E(f) \times P(f) \times S(f) \tag{2.2}$$

The propagation spectrum can be expressed as:

$$P(f) = \frac{1}{R^{\eta}} e^{-\frac{\pi f R}{Qc}} = \frac{1}{R^{\eta}} e^{-\pi f t^{*}} \tag{2.3}$$

where η is the assumed constant geometric spreading factor, and R is the source-receiver distance, Q is the assumed frequency independent quality factor, and t^* is the integral of the attenuation effect along the ray path.

The station-site spectrum can be typically represented with:

$$S(f) = I(f)A(f)e^{-\pi \kappa_s f} \tag{2.4}$$

where $I(f)$ is the instrument response, which can be obtained from the station metadata, $A(f)$ is the site amplification effect, and κ_s describes frequency-dependent near-surface attenuation (Anderson & Hough, 1984). Both parameters are related to the type of site, e.g., hard rock versus soft-sediment. Sometimes, the near-surface attenuation and the propagation effect are combined, as the formula is similar for equations 2.4 and 2.3. In this case:

$$e^{-\pi(\kappa_s + t^{*})f} = e^{-\pi \kappa f} \tag{2.5}$$

If this is the case, we will observe distance-dependent κ (Hough et al., 1988): To obtain the event spectrum E(t) in equation 2.2 multiple methods can be used, but once it is obtained it can be expressed as $\omega - square$ Brune-type spectrum (Brune, 1970):

$$E(f) = \frac{M_0\Phi}{4\pi\rho c^3}\frac{(2\pi f)^t}{[1+(f/f_c)^n\gamma]^{\frac{1}{\gamma}}} \tag{2.6}$$

where Φ is the radiation pattern term, c is the wave velocity, ρ is the density, f_c is the corner frequency, and M_0 is the seismic moment. t represents the data type, with $t = 0$, 1, or 2 corresponding to displacement, velocity or acceleration spectra, respectively (Kilb, Biasi, et al., 2012). n is the high frequency fall off rate and γ is a constant that controls the sharpness of the corner in the spectrum. The Brune (1970) model uses $n = 2$, and $\gamma = 1$, however $\gamma = 2$ can also be used to produce the Boatwright model (Boatwright, 1980). Stress drop can be calculated from corner frequency f_c and seismic moment M_0 following Eshelby (1957) and Brune (1970):

$$\Delta\sigma = \frac{7M_0}{16}(\frac{f_c}{k\beta})^3 \tag{2.7}$$

β is rupture velocity and k is a scaling factor. The scaling factor depends on which theoretical relationship is used to relate corner frequency to the source, and such relationships depend on the assumed source geometry (e.g. circular or elliptical), rupture style (e.g. symmetric or asymmetric), and rupture speed (e.g., Sato & Hirasawa, 1973; Boatwright, 1984; Abercrombie, 1995; Prieto et al., 2004; Abercrombie & Rice, 2005; Imanishi & Ellsworth, 2006; Kwiatek & Ben-Zion, 2013; Kaneko & Shearer, 2014).

2.5.1 Data Preparation

Due to the low magnitude of the events being examined, we use stations with sampling rates of 250 Hz. For the P-waves, we calculate the spectra over a window that begins 0.1 s before the P arrival and extends to 0.5-1 s depending on the S-arrival time. A noise window of similar length is selected before the P-wave to be used for an estimation of the Signal-to-Noise Ratio (SNR). For the S-wave we calculate the spectra over a 1.5 s window starting 0.1 s before the S arrival. A number of previous studies of Oklahoma earthquakes performed their analyses using longer S-wave windows (Sumy et al., 2017; Yenier et al., 2017) or on the Coda (Wu et al., 2018). To examine the effect of using a longer window on the resulting source parameter estimates we also calculate spectra using a 10 second window that starts 0.1s before the S arrival (hereafter referred to as "S10"). For all methods the spectra are calculated using a multi-taper algorithm (Prieto et al., 2009). We then compute the velocity spectra for the signal and noise windows, convert to displacement, and resample all spectra to equal log-spacing between 0.5 and 95 Hz. For the P-wave analysis we only use the vertical channel, and for the S and S10 data we use the geometrical mean of the two horizontals. We use different SNR criteria (Table 2.8.1) for each method. Except for the spectral ratios (SR method), the SNR criteria are only applied to the P-wave and we assume that if the P-wave spectra meet the criterion then so do the S-wave and S10.

In order to calculate the moment for each event we calibrate the relative seismic moment Ω_0 to the absolute moment M0 using the local magnitude ML following Shearer et al. (2006). We define Ω_0 using the mean amplitude over the $1-3$ Hz band, then fit a linear relationship between log Ω_0 and ML: ML $=$ 1.0 log Ω_0 $+$ 2.19. The events used in the fitting are only events from the original OGS catalog, due to the systematic magnitude difference between the OGS catalog and the subspace-detected catalog (Figure 2.4). We assume ML=Mw at ML=3.0, and calculate Mw from the relative moments for all available events using: $Mw =$

$2/3 \times log(M0) - 10.7$.

2.5.2 Stacking "SNSS" Approach: Spectral Decomposition and ECS Calculation

The spectral decomposition approach developed by Shearer et al. (2006) is based on the theory that if there are enough event-station pairs, equation 2.2 becomes an over-determined system of equations. The recorded spectra D_{ij} for an event will have the common features of the event's spectra E_i and the recording at each station will all have the same site/station effects S_j across all earthquakes. To solve for the propagation effects which are also part of the recorded spectra, we need to separate events into groups that have similar paths. This is done by placing events with similar travel times into bins at 0.2 second increment $P_{(k(i,j))}$, where k refers to the index of the travel-time bin. Note that by doing so, a constant attenuation structure (Q-value) is assumed for the dataset. Following Chen and Abercrombie (2020), the Brune model is used for "SNSS" approach. With these, equation 2.2 can be rewritten as a linearized system in log-domain:

$$D_{ij} = E_i + P_{(k(i,j))} + S_j + R_{ij} \tag{2.8}$$

where R_{ij} is a residual error term. In order to mitigate the influence of outliers, an iterative method is used to solve for $P_{(k(i,j))}$, S_j, E_i, which is performed for each frequency point independently (Shearer et al., 2006).

This decomposition only obtains the relative shapes of the event term. Some near source attenuation could be absorbed into event terms, and an additional correction is required to obtain the event spectral shapes. The correction is referred to as the Empirical Correction Spectrum (ECS) in this study, and is referred to as the global-EGF by Shearer et al. (2019). To calculate the ECS we follow the procedure denoted as “SNSS” (Stacking-No-assumption-of-Self-Similarity) in Chen and Abercrombie (2020). This procedure follows these steps: (1) Stack the estimated spectrum E_i into 0.2 magnitude bins. (2) Go through trial stress drop values and for each calculate the predicted spectrum using equation 2.7 for the lowest magnitude bin and calculate the misfit between the prediction and the observation (3) Use the misfit as the initial ECS to correct the stacked spectra in the other magnitude bins. (4) Fit the initial ECS corrected spectra for all the magnitude bins and estimate their overall misfit. (5) The initial ECS for the trail stress drop that produces the lowest misfit for all magnitude bins is then used as the ECS to correct all earthquakes. Unlike the method used by Shearer et al. (2006), which assumes self-similarity that requires all magnitudes to have the same stress drop, we instead allow it to vary. For detailed method validations from synthetic tests, refer to Chen and Abercrombie (2020).

Using a single ECS assumes an attenuation correction with a constant Q. If a significant percentage ($> 10\%$) of events occur in differing lithologies or if they occur over a large area (>50km) where attenuation would be expected to vary a constant attenuation would not appropriately account for path effects. The earthquakes in our catalog occur in two different lithologies, with earthquakes occurring in sedimentary lithology and in the granitic basement (Figure 2.1 d). The effects this differing lithology has on the waveforms of earthquakes can be when examining events from different depths (Figure 2.1 b). To account for this we calculate two ECS, one for events shallower than 3 km, which is 400 m deeper than deepest estimate for basement depth, and those greater than 3km. Due to the limited number of events in the shallow region the ECS for this region will be less constrained.

For an event to be used in the calculation of the ECS we require it to have good quality spectra at a minimum of 5 stations for stability. The magnitude ranges used to calculate the ECS vary depending on the quantity of the data. For shallow events M1.5-M2.5 bins are used for the P, S and S10 data. For deeper earthquakes the ECS is estimated over magnitude ranges of 1.3-2.7, 1.5-2.7, 1.5-2.5 for P,S and, S10 data respectively with a higher lower magnitude limit chosen for the S and S10 data due to the possibility of high frequency noise affecting the lowest magnitude bins. We then use these estimated ECS's to correct the individual event spectra. Following Viegas et al. (2010) we perform a grid search to find the best fitting value of f_c, and its uncertainties ($f_{c_{max}}$, ($f_{c_{min}}$) defined by the 95% confidence limits using $\chi - square$ distribution and the region of variance increase that is within 5%. We then only accept f_c estimates that are below our maximum frequency range (60 Hz), have 6 stations, and the estimated error is $((f_{c_{max}} - f_{c_{min}})/f_c = f_{c_{err}} \leq 0.2)$. For the P, S, and S10 data 417, 476, and 425 events respectively have f_c estimates that meet our criteria, of which 351 are in common across all data types.

2.5.3 Individual Joint Spectral Fitting "JS"

Combining the fundamental equations of $P(f)$ (eq. 2.3), $S(f)$ (eq. 2.4,2.5) and $E(f)$ based on the $\omega - square$ Brune-type spectrum (eq. 2.6) we obtain the following equation which is individual to the Joint Spectral Fitting method:

$$D(f) = \frac{1}{R^{\eta}} \frac{M_0 \Phi}{4\pi \rho c^3} I(f) A(f) \frac{(2\pi f)^t}{[1 + (f/f_c)^n \gamma]^{\frac{1}{\gamma}}} e^{-\pi \kappa f} \tag{2.9}$$

Based upon this theoretical equation it is possible to estimate f_c by applying a joint inversion to individual spectra to find the best fitting f_c and κ. This type of joint inversion can be used to obtain source parameters for either individual earthquakes (e.g., H. Zhang et al., 2016), or nested earthquake clusters (e.g., Sumy et al., 2017; Neighbors et al., 2017). Such inversions are subject to trade-off between f_c and κ (Kwiatek, Goebel, & Dresen, 2014; Kilb, Peng, et al., 2012). For small magnitude events with higher f_c values the amount of bandwidth available becomes more limited, making the estimation of κ unreliable. This causes the tradeoff between κ and corner frequency to be more severe for smaller magnitudes events, which make up a large number of events in the Prague Sequence. We include the approach here to better understand the observations of Sumy et al. (2017).

Following Sumy et al. (2017) and (Chen & Abercrombie, 2020) we calculate the horizontal and vertical (H/V) spectral ratio correction for each earthquake at each station for both the S-wave and S10 spectrum using the same stations and spectra utilized in the SNSS analysis. We remove the median H/V ratio at each station, which effectively removes the frequency-dependent site amplifications and resonances ($I(f)\ A(f)$) from the horizontal channels. For each individual earthquake at each station, we estimate both κ and f_c and their uncertainties using the method developed by Viegas et al. (2010) and detailed above in the decomposition section. We estimate the overall f_c measurement of an event by taking median corner frequency of all its stations measurements. We obtain f_c estimates for 230 events for both the S and S10 data that pass the criterion of having 6 or more stations.

2.5.4 Spectral Ratios

We follow the approach developed by Abercrombie (2014); Abercrombie et al. (2017); Ruhl et al. (2017) to analyze all the earthquakes recorded by the higher sample rate stations, using the values assumed in Abercrombie et al. (2017) unless otherwise specified. We use a fixed time window of 0.75 s so as to include P waves from close stations (and avoid S wave energy). All 3 components, P and S are considered. We require EGF pairs to be within 1 km epicentral distance and a magnitude difference > 1 based upon the calibrated magnitudes. We then calculate the cross-correlation between each pair of seismograms, low-pass filtered at the expected corner frequency of the target event, assuming constant stress drop (3.3 Hz at M3.5, 10 Hz at M2.5). This is because large and small earthquakes are not expected to cross-correlate well at high frequencies (e.g., Abercrombie, 2015). We calculate the spectral ratios for each pair of seismograms.

As in the spectral decomposition approach, stacking large numbers of ratios is an efficient way of increasing the signal and decreasing uncertainty. We select and stack all normalized ratios corresponding to a range of minimum cross-correlation threshold values; using a lower threshold increases the benefits of stacking more ratios, but requires including less-appropriate EGFs which can lead to increased uncertainties. The results presented here are for 0.8, but we try other values 0.7-0.9. We first stack all EGF and components at each station, then stack all the mean station ratios so as to weight stations equally (Shearer et al., 2006). The need for both well-recorded target and EGF events means that this analysis is limited to a relatively small number of the larger events. Of the 81 M$\geq$ 2.3 analyzed, 8 (M2.5-3.4) meet strict selection criteria. Each have 5-12 stations (median 6) and 10-25 EGFs.

We fit the log-sampled spectral ratios, using use the sharper-cornered (Boatwright, 1980) model, with $\gamma = 2$ (eq. 2.6). We only fit the frequency range in which (at each sample) the signal of both the large and small events is at least three times the spectral amplitude level in a noise window immediately preceding, and of the same length as, the respective signal window. The noise windows for the S waves include the P wave coda, preventing contamination of the S spectra with P wave energy at higher frequencies. To avoid the ambiguity noted by Shearer et al. (2019), we constrain f_{c2} by assuming the EGF stress drop is between 1.5 and 40 MPa, using the median moment-magnitude of the EGFs.

We use the selection criteria developed by Abercrombie et al. (2017) to identify the best resolved ratio fits. We require the variance to have a parabola shape with a clear minimum (variance ≤ 0.005) at the preferred corner frequency. We set the limit in the corner frequency uncertainty to be a factor of 2 ($(f_{c_{max}} - f_{c_{min}})/f_c = f_{c_{err}} \leq 2$). This is larger than the uncertainty used for the spectral decomposition results and is due to the bumpy and irregular nature in spectral ratios. To limit the effect of bumps and irregularity in the spectral ratios, we use only measurements where the difference in amplitude of the high and low frequency levels in the fit is greater than 2 (fit-amp-ratio ≥ 2).

The use of a variance threshold excludes the spectral ratios most poorly fit by the assumed source model, but some of the remaining ratios exhibit clear evidence of more complex sources (Uchide & Imanishi, 2016). These are supported by the relative source time functions calculated as part of the inversion (Abercrombie et al., 2017).

2.6 Results

We describe and compare our results in the context of those from previous studies to identify the features that are due to data selection and method biases. Table 2.2 lists the studies, the method, type of data used (e.g. P,S or S10), frequency range examined when specified, and SNR criteria when specified. To briefly summarize the studies, we will compare our results to: Yenier et al. (2017) who uses ground motion analysis to fit a regional model for the Prague area and derive stress drops from the event terms (referred as "Y17"). Sumy et al. (2017) who jointly inverts for κ and f_c using a non-linear inversion method (referred as "S17"). Wu et al. (2018) used spectral ratios estimated from multiple coda windows and more distant stations with 100 Hz sampling rates (referred as "W18"). Results obtained in this study include: individual joint spectral fitting analysis for the S and S10 data (referred as "JS S" and "JS S10", respectively); SNSS stacking based analysis method results for the P, S and S10 (referred as "SNSS-P","SNSS-S", and "SNSS-S10", respectively); individual-pair EGF spectral ratio analysis performed on the P-wave (referred as "SR-P").

To allow for the direct comparison of results across studies we use the f_c values estimated by each method and from each study, and calculate the stress drops for each event using equation 2.7. To remove potential biases due to inconsistency in seismic moment among different studies, we also use the seismic moment derived from our moment calibration process for each event. We observe a mean f_{c_p}/f_{c_s} ratio of roughly 1.2 (Figure 2.5 (a)), which is significantly smaller than the ratio found by Madariaga (1976), making the k value estimated in there model in appropriate. In order to allow our estimates to align we assume the values obtained by Kaneko and Shearer (2015) for a symmetrical circular model with a rupture velocity of 0.7β. This model has a k= 0.32 for P-waves and, k = 0.26 for S-wave. We prefer this model as it makes P and S waves comparable in our data sets and has been found by previous studies with similar f_{c_p}/f_{c_s} ratios (Abercrombie et al., 2017; Ruhl et al., 2017). We use k=0.26 for all datasets and studies that use S-wave or S-coda data. The Yenier et al. (2017) (Y17) does not provide f_c estimates but the stress drop values should be comparable to a Brune model with a k of 0.372 (Gail Atkinson, personal communication, 2017). To align these values with our results we multiply Y17 estimates by 2.928 to align them with S-wave k value due to their data using 40 s windows. For the initial comparison due wanting to stay consistent with the estimates of Y17 we use a constant rupture velocity of 3.4 km/s for all events. A comparison of f_c and $\Delta\sigma$ estimates for those events in common between all results and our S-wave estimates is shown in Figure 2.5, and discussed below.

2.6.1 Effect of Different Wave Types

When examining the range of stress drop values obtained by studies and how the choice of data window can affect it, the most prominent features that can be observed in Figure 2.5 is how the values of S17 and JS-S10 in general strongly deviate from the other results. In contrast to these results those results obtained from those studies that analyze P-waves (SR-P and SNSS-P) have stress drops that have the same trends with those observed for the S-wave (SNSS-S and JS-S) and in general align fairly well. Those methods that rely on longer windows (S17, SNSS-S10, JS-S10,Y17), to study the S-wave coda tend to have lower stress drop values with the exception of SNSS-S10, Y17, and the lower f_c estimates of W18. The study of W18 uses fairly short windows and high SNR criteria (Table

2.2) when studying the S-wave coda, which might explain why it aligns fairly well with the other observations with the exception of it's high f_c estimates. Y17 does not purely focus on the S-wave and its coda but on the entire waveform with its 40 s window starting at the P arrival. The reason why the JS-S10 and JS-S so strongly disagree is likely do with the long window length and its focus purely on the S-wave and its coda and the less strict SNR criteria placed on them, which appears to have less of an effect on the shorter window S-wave data.

Using long time windows for the small events in the sequence risks the windows extending beyond the point where the signal merges back into the background noise. This will have a greater impact on joint spectral fitting methods that invert for an attenuation correction directly from the spectra. This attenuation correction (κ from eq. 2.5) is obtained from the decay of high frequency energy above the corner frequency. The inclusion of noise in this range will make the estimation of a κ value unreliable. The use of such long windows is preferred when studying >5M events as in the study by Anderson and Hough (1984) that introduced the method, because these large events radiate most of their energy at lower frequencies, and their larger amplitudes mean that their coda waves last longer. When examining smaller magnitude events such as M3.5 window ranges of around 2-5 s are often used (Neighbors et al., 2017; Kaiser et al., 2012; Zuyuan Liu et al., 1994). The use of shorter windows (1.5 s) like those used in the JS-S results produces results that better align with other observations (Figure 2.5 a,b).

A possible indication of noise being included at high frequencies is the strong divergence between JS-S and JS-S10 κ measurements. The JS-S κ values at short distance ranges (3-6km) show a decrease while J-S10 κ values do not for small magnitudes (Figure 2.6 b). This indicates that in the JS-S result κ is accounting for both site and path effects at close distances (Anderson & Hough, 1984), while S10 is not. Another strong indication that the spectra of S10 are somehow systematically different than S is that the f_c estimates diverge significantly between the two (Figure 2.6 a). In order for them to align the κ correction of the JS-10 would need to be much higher than the JS-S estimate. These features are only present for small magnitudes, larger magnitudes (≥ 2.5) show better correlation between JS-S10 and JS-S indicating that the differences between spectra are strongest for small magnitudes(Figure 2.6 c-d). This magnitude dependence supports the idea that the divergence in estimates between JS-S10 and JS-S are caused by noise at high frequencies, which is amplified with the use of long windows for small magnitude events. The results of the S17 study also might suffer from such an issue due to the usage of windows that extend well beyond 10s (Sumy et al., 2017).

2.6.2 Effect of Different Methods

For the spectral ratio and stacking analysis results that estimate corner frequencies from the P-waves we find high levels of agreement between results with only a few outliers (Figure 2.5 a). The SR-P f_c are higher than those of the SNSS-P by roughly 4-40% and due to their lower corner frequencies, these deviations translate to changes of 11-168% in $\Delta\sigma$ (Figure 2.5 (b-c). The small difference in f_c (<20%) between the SR-P and SNSS-P estimates, which use the same data is likely caused by the preservation of individual events small complexities and deviations either in the spectrum of the target or EGF event when using the individual EGF method. The results of Y17 which used an extended P-wave window also generally align with these results. This could be due to the GMPE method or that it included the entire waveform in its analysis.

In general, there is good agreement in the trend and proximity of the estimates of JS-S and SNSS-S (Figure 2.5). The JS-S f_c results are higher by on average 29% in some frequency ranges and exhibit a larger degree of variance from the SNSS-S results. A possible cause for this difference is that the f_c estimates from the JS method are obtained from individual spectra with the final f_c estimate being the median of the individual estimates. This makes the JS method more susceptible to bumps and complexities in the spectra to higher degree than the SR method. In contrast the SNSS method is designed to suppress spectral complexity. In past studies the reliability of estimates from the JS method are observed to decrease if the f_c exceeds 1/3 of the modeled frequency range (Chen & Abercrombie, 2020). We do not observe this in our results, we observe similar trends in the f_c estimates for SNSS-S and JS-S for f_c estimates past 30 Hz. For this reason, we will not restrict the JS results to those below 30 Hz and will instead interpret all their estimates. This will allow us to judge the reliability of interpretations that are solely based on such values.

The results from SNSS-S10 in general align with the other wave types, however it does not align with JS-S10 (Figure 2.5 a-b). Unlike the JS fitting results, the SNSS-S10 seem to be unaffected by the poor SNR quality of their data. This may be attributed to how the ECS correction is calculated. Multiple magnitude bins are used to constrain the ECS, this reduces the impact of smaller magnitudes, which are more effected by high frequency noise. This results in a majority of the SNSS-10 f_c estimates aligning with the other results with only the highest f_c starting to deviate.

2.6.3 Comparison of Large Magnitude Events

To examine the largest events, we apply the SR-P analysis approach (with same constraints/assumptions) to the three largest events using the regional lower sample rate stations (Figure 2.1 b), scaled window parameters to align with their magnitudes (17-30s) and expanded the search range (< 10 km) for EGFs for the mainshock (Abercrombie et al., 2017). Our final corner frequency estimates for these events are based on spectral ratios from 9-13 stations using 10-35 EGFs each. We compare these results to previously published studies (Table 2.8.1 (e.g.,C17, Y17, S14, W18, B17,H17)).To ensure direct comparison, we recalculate the stress drops, using the published corner frequencies and the estimated moments of 3.55×10^{16}, 3.98×10^{17}, and 3.55×10^{16} Nm for the foreshock, mainshock, and aftershock respectively, and assumed a Brune source model (k=0.372) in order to match the value of Yenier et al. (2017). For the rupture velocity we select the value based upon the velocity model, which might cause systematic deviations from the studies which only present final $\Delta\sigma$ estimates (e.g. S16 and Y17). The only variable that was adjusted between calculations was the f_c value. For the studies of Yenier et al. (2017) and X. Sun and Hartzell (2014), which directly calculated the stress drop, we use the published stress drop estimate.

There is real variability between the different studies (Figure 2.8), but there are also clear relative trends, and method-based explanations for some of the differences. On average, the four studies that obtain f_c estimates from spectral ratios (e.g., SR-P, H17,B17,W18) in general agree with one another, except for B17. The studies that do agree find that the largest foreshock and aftershock both have higher stress drop (order of 10 MPa) than the mainshock, which is significantly lower than 10 MPa in all but two studies. B17 has a similar values for the mainshock to the other spectral ratio studies, but significantly lower stress drops for the foreshock and aftershock. The reason for the underestimation of the foreshock and aftershock stress drops could be because they are measured as the denominator in the ratio. Abercrombie (2013) found that corner frequencies determined for events in the denominator are systematically biased to be lower than those of the numerator when compared to when the denominator event is in the numerator.

The finite slip inversion result of S14 is the average stress drop over all areas of slip, but observes peak stress drops near the hypocenter of 7-9 MPa (X. Sun & Hartzell, 2014). This range of values places this estimate in the same magnitude range as the spectral ratio determined values. The finite fault inversion method makes fewer assumptions compared to those estimates from spectral ratios, but the final stress drop estimates is dependent on the size of the grids the inversion is calculated over. The ground motion study of Y17 finds similar estimates to the other studies for the foreshock and aftershock they however obtain a stress drop estimate of over 10MPa for the mainshock, which is high but it still falls within a magnitude range of the other estimates. C17 obtains similar results to the other spectral ratio studies for the foreshock and aftershock, but a significantly higher value for the mainshock. C17s estimates rely on the hand picking of the f_c from the peak of the tangential component of the velocity spectrum, and intentionally exclude the lowest frequencies that control the corner frequency in the other studies, which could explain the difference between its f_c estimate for the mainshock compared to the other studies (Cramer, 2017). C17s estimates for the aftershock and foreshock do align with the other results.

If we take into account these method dependent biases and examine the pattern we observe that the relative patterns across results remains fairly stable.

With the major interpretation we can draw from them that the mainshock had a lower stress drop than the foreshock and the aftershock.

2.6.4 Reliability of Stress Drop Interpretations

To understand how method or data type might affect the final interpretations of a study we examine the spatial patterns, depth, and magnitude dependence of the stress drops calculated for the smaller events by each study and method. We only include studies with over 100 events to allow for statistically significant comparison. In order to account for the possibility of changing rupture velocity with depth we recalculate all the stress drop estimates using the same parameters used in the initial comparison at the start of the Results section, but now use a depth dependent rupture velocity based upon the 1D velocity shown in Isken and Mooney (2017).

Depth Dependence

A common observation made from source parameter studies is the depth dependence of stress drop and if stress drop scales with moment (e.g., Hardebeck & Aron, 2009; Allmann & Shearer, 2007; Baltay & Hanks, 2017; Shearer et al., 2006; Trugman et al., 2017). These depth dependence may relate to along depth variation of frictional strength. However, these depth dependences can also be method related, previous observations of depth dependence were reduced when using a depth dependent ECS (Q. Zhang et al., 2017), suggesting some of the trend could be due to trade-off with other parameters. We have attempted to correct for this by using two different ECS (one for the events in the sediments, and one for those in the basement), but calculation of the ECS requires a large number of events and so results obtained using a small number as in the shallow region could be less reliable.

To examine the possible depth dependence patterns, we examine the ratio of the median stress drop for specific depth bins to the median stress drop for the entire depth range (Figure 2.7 a). All approaches find negligible depth dependence from 3-6 km of depth. At greater depths (>7km) the SNSS and JS-S10 results exhibit a large increase in stress drop, with the SNSS-P JS-S10 showing the strongest change. At shallow depth's the SNSS ranges show good agreement with the median value except for at 2.5-3 km depth range. In contrast to these findings, the JS-S results can obtain stress drops that generally align with the median from 3-7.5 km of depth, but observe higher stress drops for shallow events and lower stress drop for deepest events. At the greatest depths the patterns of deviation from the median all generally match between results (higher than median values). However, the patterns of deviation do not agree for the shallowest events, and therefore stress drops that fall in this region should be considered unreliable.

Magnitude Dependence

To examine if there is any scaling relationship between stress drop and moment, we examine the events that occur in 3-6 km of depth, in order to avoid bias due to depth dependence. We fit a linear model to an expanding range of magnitudes and the median stress drop observed in each magnitude bin, in order to investigate where slope of the fitted model stabilizes, and if magnitude dependence occurs for different magnitude ranges (Figure 2.7 (b-c)). The slope of the linear model fit for the SNSS-S, SNSS-S10, and JS-S shows no strong dependence with magnitude range when examining the magnitude range of 1.5 to 2-2.5M .

In contrast, both SNSS-P and JS-S10 do show a scaling relationship with magnitude with a slope of 0.5 and 0.8 respectively. This implies that the magnitude relationship will depend on the data and methods used. For example, if we only examined the P-wave with the SNSS method we could conclude a scaling relationship exists, however based on all the results most of them agree that there is no scaling relationship. This result is consistent with the large uncertainty and lack of resolution most studies have for such scaling relationships (e.g., Shearer et al., 2019; Chen & Abercrombie, 2020).

Spatial Variation

The first spatial interpretation we will examine for consistency between results is the distribution of stress drop along the surface of the MF and on each individual fault group. The stability of such interpretations is vital in the interpretation of spatial pattern of stress drop, since it has important implications for the hazard that differing faults pose. For all the studies with significant numbers of events to examine, we examine their patterns along the MF and these are shown in Figure 2.9. We generally find that the regions with high and low stress drops agree between studies. All studies find that the earthquakes that occured directly to the south (10-7.5 km along strike and 5 km depth) of the mainshocks hypocenter have higher stress drops than those occurring to the north of the hypocenter (7-6 km long strike and 5 km depth). The majority of them also find that the slip patch located above the hypocenter (10-5 km along cross section and 3-5 km of depth) is often surrounded by high stress drop events, while the slip patch is the focus of relatively lower stress drops. The one exception to this is JS-S10, which has more uniform patterns for those regions, which is likely due to its significantly divergent stress drops estimates discussed in the sections above. The lack of agreement in the shallow portion of the fault (2.5-0 km) can be attributed to the instability of estimates in this depth range. However, below this depth range the patterns generally agree, so even when estimates vary systematically by method (e.g. JS-S and SNSS-S10) their spatial patterns agree.

This finding is supported when we examine the distribution of stress drops in each of the fault groups identified in section 3 and locations are shown in Figure 2.1. All methods and datasets find that the AF fault exhibits a higher median stress drop than the other fault groups (Figure 2.10). The median value changes with method and data, but the AF consistently remains higher than the other faults. The values of the other fault groups generally fall close to one another except for the results of SNSS-P and JS-S10. The cause of the difference observed for shallow events in SNSS-P can be attributed to the general instability of the ECS calculation. The results of the JS-S10 show the most variability, and as explained in the previous sections are considered the least reliable.

2.7 Discussion

By estimating source parameters using a variety of methods and data types we are now able to identify spatio-temporal patterns that can be considered reliable enough to investigate geologic or triggering processes. We first examine the possible causes for the relative stress drop levels observed for each fault group. Second, we examine whether any strong relationship exists between the spatial stress drop pattern and the slip of the mainshock. Lastly, as in previous studies, we investigate whether we can resolve the effects of injection on the spatio-temporal patterns of stress drop.

2.7.1 Geological and Structural Controls: Comparison of Different Fault Groups

Interpreting possible geologic controls on stress drop can be best done by examining the stress drops of the different fault groups (Figure 2.10). The effects of geologic formation (e.g. sedimentary rocks and basement) cannot be confidently interpreted given the difficulty of resolving the trade-off between stress drop and attenuation in the shallow sedimentary layers, but in general they appear to exhibit similar levels of stress drop in the basement if the results of the SNSS and JS results are correct. The higher stress drop of the AF is the strongest signal of some geologic effect playing a role in the sequence. The cause of this higher stress drop is hard to isolate, since there are multiple forces effecting it. These include the lower shear stress that should be experienced by this fault as it is parallel to the regional SHmax based on the stress analysis of Walsh and Zoback (2016); Cochran et al. (2020). Second, the fault lies in the stress shadow of the mainshock rupture (Sumy et al., 2014). Third, past studies have observed events occurring in the damage zone as well as on the linear fault surface, indicating two populations of events (Savage et al., 2017). Lastly the interactions between the AF (left-lateral rupture) and the MF (right-lateral rupture), are not well understood. All these factors could have led to the observed higher stress drop for this fault segments.

2.7.2 Effect of Coseismic Slip

Past studies have found that the slip in a large earthquake effects the location of aftershocks, and that such effects are more significant when the distribution of slip is heterogeneous like observed in Prague (Woessner et al., 2006). Slip can also reduce stress drops of aftershocks, due to these events rerupturing incompletely healed parts of the fault (Smith & Priestley, 1993; Shaw et al., 2015; Wang et al., 2018). Many of the results shown in Figure 2.9 exhibit lower stress drops at locations where significant coseismic slip occurred (>40 cm) during the mainshock, indicating a similar effect could be occurring here. Observations like these inherently depend on the resolution of the slip model, and the accurate relocation of events relative to the mainshock slip. Due to this instead of using the absolute location of an earthquake in relation to the slip model we use the 3D distance of an earthquake from slip patches of certain slip amounts. In order to remove possible bias due to depth dependence we divide each event's stress drop by the median stress drop observed for event's whose depths fall within 1.5 km of the target event's depth to obtain a stress drop ratio (SDR) relative to its respective depth range. For each event we find its distance to the closest 40 cm and 60 cm slip patch. For 15 logarithmically spaced distance bins between 0.01 km to 5 km we calculate the median SDR for distance ranges with 10 or more events and the results are shown in Figure 2.11 a,b.

For the 40 cm and 60 cm slip patches we observe a clear increase in stress drop with distance from the respective slip patch. With the closest events (<100 m) having stress drops 25% lower than the median observed in their respective depth ranges. At ranges of 100 m-1 km we observe events having stress drops that align with the median and at distances of >1 km stress drops are consistently higher than the median. To test the possible bias in each bin we perform 100 bootstraps to determine the standard deviation of each bins median estimate. For most methods these error bars due not extend above the median for their depth range making the observation statistically stable. Exceptions are the JS and S10 estimates, but their stress drops findings often are less accurate than others. For the 40 cm slip patch estimates we observe the most stability in our observations, with both the JS results also observing an increase in stress drop. It should also be noted that we also observe high stress drop regions occurring at the edges of high slip patches in Figure 2.9, similar to the finding of Shearer et al. (2006) and Ruhl et al. (2017).

2.7.3 Effects of Injection

Previous interpretations suggest that lower stress drop for sequences in the central US could be caused by injection saturating a fault system (Sumy et al., 2017; Trugman et al., 2017). High pore pressure from injection has been found to lower crustal strength and Coulomb stresses on a fault (Bell & Nur, 1978), which can lead to lower stress drop (Kanamori & Anderson, 1975; Pearson, 1981; Goertz-Allmann et al., 2011). This effect can be observed by examining the trend of stress drop versus distance from the injector. If there is a relationship one would observe a correlation between the two with low stress drop occurring at close distances and high stress drop at further distances from the well (Chen & Shearer, 2011; Goertz-Allmann et al., 2011; Kwiatek, Bulut, et al., 2014).

To determine if we observe any such correlation, we perform a similar analysis to that done to examine the relationship to slip. Instead of the distance to slip we instead examine the distance from the hypocenter location to the bottom of the Wilzetta injection well, which injected a majority of the wastewater in the area, and the stress drops observed for the FF fault group (Figure 2.1 a). This fault group is where the foreshock occurred and is the fault closest to the injector and would have experienced the strongest effects of injection. We find that events closest to the injection well do not have lower stress drops compared to more distant events (Figure 2.11 c). If injection was playing a strong role we would expect to observe some relationship. It is possible that the earthquakes are too far from the injector to observe any spatial pattern. Goertz-Allmann et al. (2011) observations of lower stress drop were within 500 m.

An explanation for the lack of an observation of the effect of injection is the finding by (Staszek et al., 2017) that temporal stress drop variations are inversely related to injection rate and stress drops return to previous levels once the injection rate is reduced. If the requirement for lower stress drop estimates is a constant high pore pressure, which only occur during periods of high injection the effect on stress drops at Prague might be minimal. It could still have an effect if the injected fluid became trapped within the fault system, a scenario which is suggested for the cause of the foreshock (Keranen et al., 2013).

The average stress drops across all results with the exception of JS-S10 find stress drops comparable to tectonic earthquake sequences. Fluid injection may cause lower stress drop during early stages of fault activation, as observed in Chen and Abercrombie (2020) and Yoshida et al. (2017). However, due to lack of station coverage prior to the largest foreshock of the Prague sequence, we cannot assess whether fluid injection affected fault activation.

2.8 Conclusion

Using a single coherent relocated catalog of the events detected by the Oklahoma Geological Survey (OGS) and McMahon et al. (2017) we separate events based upon their fault structure. Through the examination of these events source processes using a variety of methods and wave types we separate the source parameter variations that are due to data selection and method and those that can be attribute to rupture processes and fault properties. From this analysis we draw the following conclusions:

- Stress drop values in general fall within factor of 2 of one another when similar data are used, independent of the method. The relative spatial and temporal patterns observed across these results is broadly consistent lending support for their interpretation.
- The interpretation of the absolute stress drop values and there usage as exact measures of a earthquakes stress drop should be done with extreme skepticism. The usage of these values for such a purpose assumes that these earthquake have a circular rupture area with a symmetric rupture. Variability in source geometry, rupture directivity, and rupture speeds could cause a deviation up to a factor of 8 from the true stress drop measure assuming that there is no bias due to improper path or site correction (Kaneko & Shearer, 2014).
- We find that stress drops for the Prague sequence are similar to values estimated for tectonic events in the Central U.S. (Y. Huang et al., 2017). Such findings are consistent across methods and datasets, with the exception of those results obtained using data with windows greater than 10 s in combination with joint spectral fitting.
- We find no correlation between injection and stress drops estimates for all methods and datasets; the earthquakes are further from injection sources than in previous studies that found any correlation. We also lack observations prior to the largest foreshock of the Prague sequence, so we assess whether fluid injection effect on fault activation.

- Aftershocks closer to areas of higher slip in the mainshock have relatively high stress drops; those within 100 m of coseismic slip of $\geq$ 40 cm have stress drops roughly 25% lower than other earthquakes.

In summary, our comparative study shows that using only one method to estimate stress drop will probably result in some systematic bias; using a range of methods and looking for the stable features across them allows for the identification of features that can be attributed to rupture processes and not method. This verification of observations is especially important when examining large earthquake catalogs that extend over broad spatial, temporal, depth, and magnitude ranges. This can be done for a subset of events. This verification of source parameters results can help identify method biases or data problems, such as improper attenuation corrections, noisy data. This will help prevent their interpretation in results.

2.8.1 Acknowledgments

We thank the Oklahoma Geological Survey (OGS) and USGS for continuous monitoring earthquake activities in Oklahoma. The catalogs for earthquake and fault plane solutions are obtained from OGS which can be downloaded from `https://ogsweb.ou.edu/eq_catalog/` (Walter et al., 2020). The earthquake waveforms are downloaded from IRIS DMC. A statewide wastewater disposal well database is available from the Oklahoma Corporation Commission (OCC) website (`http://www.occeweb.com/`).

References

Abercrombie, R. (1995). earthquake source scaling relationships from -1 to 5 Ml using seismograms recorded at 2.5-km depth. *J. Geophys. Res.*, *100*(B12), 24015–24036.

Abercrombie, R. (2013). Comparison of direct and coda wave stress drop measurements for the Wells, Nevada, earthquake sequence. *Journal of Geophysical Research: Solid Earth*. doi: 10.1029/2012JB009638

Abercrombie, R. (2014). Stress drops of repeating earthquakes on the San Andreas Fault at Parkfield. *Geophysical Research Letters*, *41*(24), 8784–8791. doi: 10.1002/2014GL062079

Abercrombie, R. (2015). Investigating uncertainties in empirical Green's function analysis of earthquake source parameters. *Journal of Geophysical Research : Solid Earth*, *120*, 1–15. doi: 10.1002/2015JB011984.Received

Abercrombie, R., Bannister, S., Ristau, J., & Doser, D. (2017, 1). Variability of earthquake stress drop in a subduction setting, the Hikurangi Margin, New Zealand. *Geophysical Journal International*, *208*(1), 306–320. Retrieved from `https://academic.oup.com/gji/article-lookup/doi/10.1093/gji/ggw393` doi: 10.1093/gji/ggw393

Abercrombie, R., & Rice, J. (2005, 8). Can observations of earthquake scaling constrain slip weakening? *Geophysical Journal International*, *162*(2), 406–424. Retrieved from `https://academic.oup.com/gji/article-lookup/doi/10.1111/j.1365-246X.2005.02579.x` doi: 10.1111/j.1365-246X.2005.02579.x

Allmann, B. P., & Shearer, P. M. (2007). A high-frequency secondary event during the 2004 Parkfield earthquake. *Science*, *318*(5854), 1279–1283. doi: 10.1126/science.1146537

Anderson, J. G., & Hough, S. E. (1984). A model for the shape of the fourier amplitude spectrum of acceleration at high frequencies. *Bulletin of the Seismological Society of America*, *74*(5), 1969–1993. Retrieved from `http://www.bssaonline.org/content/74/5/1969.short`

Baltay, A., & Hanks, T. (2017). Stress drop variability and its relation to GMPEs. *Seismol. Res. Lett.*, *submitted*.

Baltay, A., Hanks, T., & Abrahamson, N. (2019, 4). Earthquake Stress Drop and Arias Intensity. *Journal of Geophysical Research: Solid Earth*, *124*(4), 3838–3852. doi: 10.1029/2018JB016753

Baltay, A., Prieto, G., & Beroza, G. C. (2010). Radiated seismic energy from coda measurements and no scaling in apparent stress with seismic moment. *Journal of Geophysical Research: Solid Earth*, *115*(8), 1–12. doi: 10.1029/2009JB006736

Bell, M. L., & Nur, A. (1978). Strength changes due to reservoir-induced pore pressure and stresses and application to Lake Oroville. *Journal of Geophysical Research*, *83*(B9), 4469. Retrieved from `http://dx.doi.org/10.1029/JB083iB09p04469http://doi.wiley.com/10.1029/JB083iB09p04469` doi: 10.1029/JB083iB09p04469

Boatwright, J. (1980). A spectral theory for circular seismic sources; simple estimates of source dimension, dynamic stress drop and radiated seismic energy. *Bulletin of the Seismological Society of America*, *66*(3), 1271–1302. Retrieved from `http://www.bssaonline.org/cgi/content/abstract/66/3/639`

Boatwright, J. (1984). Seismic estimates of stress release. *J. Geophys. Res.*, *89*(B8), 6961–6968.

Boyd, O. S., McNamara, D. E., Hartzell, S., & Choy, G. (2017, 4). Influence of Lithostatic Stress on Earthquake Stress Drops in North America. *Bulletin of the Seismological Society of America*, *107*(2), 856–868. Retrieved from `http://www.bssaonline.org/lookup/doi/10.1785/0120160219https://pubs.geoscienceworld.org/bssa/article/107/2/856-868/354168` doi: 10.1785/0120160219

Brune, J. N. (1970, 9). Tectonic stress and the spectra of seismic shear waves from earthquakes. *J. Geophys. Res.*, *75*(26), 4997–5009. Retrieved from `http://doi.wiley.com/10.1029/JB075i026p04997` doi: 10.1029/JB075i026p04997

Chen, X., & Abercrombie, R. E. (2020). Improved approach for stress drop estimation and its application to an induced earthquake sequence in Oklahoma. *Geophysical Journal International*, *223*(1), 233–253. doi: 10.1093/gji/ggaa316

Chen, X., & Shearer, P. M. (2011, 9). Comprehensive analysis of earthquake source spectra and swarms in the Salton Trough, California. *Journal of Geophysical Research*, *116*(B9), B09309. Retrieved from `http://doi.wiley.com/10.1029/2011JB008263` doi: 10.1029/2011JB008263

Cochran, E. S., Skoumal, R. J., McPhillips, D., Ross, Z. E., & Keranen, K. M. (2020). Activation of optimally and unfavourably oriented faults in a uniform local stress field during the 2011 Prague, Oklahoma, sequence. *Geophysical Journal International*, *222*(1), 153–168. doi: 10.1093/gji/ggaa153

Crain, K. D., & Chang, J. C. (2018). Elevation map of the top of the crystalline basement in Oklahoma and surrounding states. *Oklahoma Geol. Surv. Open-File Rept. OF1-2018*.

Cramer, C. H. (2017, 7). Brune Stress Parameter Estimates for the 2016 M w 5.8 Pawnee and Other Oklahoma Earthquakes. *Seismological Research Letters*, *88*(4), 1005–1016. Retrieved from `https://pubs.geoscienceworld.org/srl/article/88/4/1005-1016/354109` doi: 10.1785/0220160224

Eshelby, J. D. (1957). The determination of the elastic field of an ellipsoidal inclusion, and related problems. *Proc. R. Soc. London, Ser. A,*, *241*, 376–396.

Goertz-Allmann, B. P., Goertz, A., & Wiemer, S. (2011, 5). Stress drop variations of induced earthquakes at the Basel geothermal site. *Geophysical Research Letters*, *38*(9), 1–5. doi: 10.1029/2011GL047498

Hardebeck, J. L., & Aron, A. (2009, 6). Earthquake Stress Drops and Inferred Fault Strength on the Hayward Fault, East San Francisco Bay, California. *Bulletin of the Seismological Society of America*, *99*(3), 1801–1814. Retrieved from `http://www.bssaonline.org/content/99/3/1801.abstracthttps://pubs.geoscienceworld.org/bssa/article/99/3/1801-1814/350168` doi: 10.1785/0120080242

Hough, S. E., Anderson, J. G., Brune, J., Vernon, F. I. I. I., Berger, J., Fletcher, J., . . . Baker, L. (1988). Attenuation near Anza, California. *Bull. Seismol. Soc. Am.*, *78*(2), 672–691.

Huang, H.-H., Aso, N., & Tsai, V. C. (2017). Toward automated directivity estimates in earthquake moment tensor inversion. *Geophysical Journal International*. Retrieved from `http://academic.oup.com/gji/article/doi/10.1093/gji/ggx354/4085269/Toward-automated-directivity-estimates-in` doi: 10.1093/gji/ggx354

Huang, Y., Ellsworth, W. L., & Beroza, G. C. (2017, 8). Stress drops of induced and tectonic earthquakes in the central United States are indistinguishable. *Science Advances*, *3*(8), e1700772. Retrieved from `http://advances.sciencemag.org/lookup/doi/10.1126/sciadv.1700772` doi: 10.1126/sciadv.1700772

Ide, S., Baltay, A., & Beroza, G. (2011). Shallow Dynamic Overshoot and Energetic Deep Rupture in the 2011 Mw 9.0 Tohoku-Oki Earthquake. *Science*, *332*. doi: 10.1126/science.1207020

Imanishi, K., & Ellsworth, W. L. (2006). Source scaling relationships of microearthquakes at Parkfield, CA, determined using the SAFOD Pilot Hole Seismic Array. *Earthquakes: Radiated Energy and the Physics of Faulting, Geophys. Monogr. Ser.,*, *170*, 81–90. doi: 10.1029/170GM10

Isken, M. P., & Mooney, W. D. (2017, 4). Relocated Hypocenters and Structural Analysis from Waveform Modeling of Aftershocks from the 2011 Prague, Oklahoma, Earthquake Sequence. *Bulletin of the Seismological Society of America*, *107*(2), 553–562. Retrieved from `https://pubs.geoscienceworld.org/bssa/article/107/2/553-562/354156` doi: 10

.1785/0120160150

Kaiser, A., Holden, C., Beavan, J., Beetham, D., Benites, R., Celentano, A., . . . Zhao, J. (2012). *The Mw 6.2 Christchurch earthquake of February 2011: Preliminary report.* doi: 10.1080/00288306.2011.641182

Kalkan, E. (2016). An Automatic P-Phase Arrival-Time PickerAn Automatic P-Phase Arrival-Time Picker. *Bulletin of the Seismological Society of America.* doi: 10.1785/0120150111

Kanamori, H., & Anderson, D. L. (1975). Theoretical basis of some empirical relations in seismology. *Bulletin of the Seismological Society of America*, *65*(5), 1073–1095.

Kaneko, Y., & Shearer, P. M. (2014). Seismic source spectra and estimated stress drop derived from cohesive-zone models for circular subshear rupture. *Geophys. J. Int.*. doi: 10.1093/gji/ggu030

Kaneko, Y., & Shearer, P. M. (2015, 2). Variability of seismic source spectra, estimated stress drop, and radiated energy, derived from cohesive-zone models of symmetrical and asymmetrical circular and elliptical ruptures. *Journal of Geophysical Research: Solid Earth*, *120*(2), 1053–1079. Retrieved from `http://doi.wiley.com/10.1002/2014JB011642` doi: 10.1002/2014JB011642

Keranen, K. M., Savage, H. M., Abers, G. A., & Cochran, E. S. (2013). Potentially induced earthquakes in Oklahoma, USA: linkes between wastewater injection and the 2011 Mw5.7 earthquake sequence. *Geology*, *41*(6), 699–702. doi: 10.1130/G34045.1

Kilb, D., Biasi, G., Anderson, J., Brune, J., Peng, Z., & Vernon, F. L. (2012). A comparison of spectral parameter kappa from small and moderate earthquakes using southern california ANZA seismic network data. *Bulletin of the Seismological Society of America*, *102*(1), 284–300. doi: 10.1785/0120100309

Kilb, D., Peng, Z., Simpson, D., Michael, A., Fisher, M., & Rohrlick, D. (2012). Listen, Watch, Learn: SeisSound Video Products. *Seismol. Res. Lett.*, *83*(2), 281. doi: 10.1785/gssrl.83.2.281

Kwiatek, G., & Ben-Zion, Y. (2013). Assessment of P and S wave energy radiated from very small shear-tensile seismic events in a deep South African mine. *Journal of Geophysical Research: Solid Earth*, *118*(7), 3630–3641. doi: 10.1002/jgrb.50274

Kwiatek, G., Bulut, F., Bohnhoff, M., & Dresen, G. (2014). High-resolution analysis of seismicity induced at Berlín geothermal field, El Salvador. *Geothermics*, *52*, 98–111. Retrieved from `http://dx.doi.org/10.1016/j.geothermics.2013.09.008` doi: 10.1016/j.geothermics.2013.09.008

Kwiatek, G., Goebel, T. H. W., & Dresen, G. (2014). Seismic moment tensor and b value variations over successive seismic cycles in laboratory stick-slip experiments. *Geophysical Research Letters*, *41*, 5838–5846. doi: 10.1002/

2014GL060159

Langenbruch, C., & Zoback, M. D. (2016). How will induced seismicity in Oklahoma respond to decreased saltwater injection rates ? *Science advances*, *2*(e1601542), 1–10. doi: 10.1126/sciadv.1601542

Li, Z., & Peng, Z. (2016). An Automatic Phase Picker for Local Earthquakes with Predetermined Locations: Combining a Signal-to-Noise Ratio Detector with 1D Velocity Model Inversion. *Seismol. Res. Lett.*, *87*(6). doi: 10.1785/0220160027

Madariaga, R. (1976). Dynamics of an expanding circular fault. *Bull. Seismol. Soc. Am.*, *66*(3), 639–666.

McGarr, A. (2014). Maximum magnitude earthquake. *J. Geophys. Res.*, *119*, 1008–1019. doi: 10.1002/2013JB010597

McMahon, N. D., Aster, R. C., Yeck, W. L., McNamara, D. E., & Benz, H. M. (2017, 7). Spatiotemporal evolution of the 2011 Prague, Oklahoma, aftershock sequence revealed using subspace detection and relocation. *Geophysical Research Letters*, *44*(14), 7149–7158. Retrieved from `http://doi.wiley.com/10.1002/2017GL072944` doi: 10.1002/2017GL072944

Mcnamara, D. E., Benz, H. M., Herrmann, R. B., Bergman, E. A., Earle, P., Holland, A., ... Gassner, A. (2015). Earthquake hypocenters and focal mechanisms in central Oklahoma reveal a complex system of reactivated subsurface strike-slip faulting. *Geophys. Res. Lett.*, *42*(8), 2742–2749. doi: 10.1002/2014GL062730

Neighbors, C., Cochran, E. S., Ryan, K. J., & Kaiser, A. E. (2017). Solving for Source Parameters Using Nested Array Data: A Case Study from the Canterbury, New Zealand Earthquake Sequence. *Pure and Applied Geophysics*, *174*(3), 875–893. doi: 10.1007/s00024-016-1445-2

Norbeck, J. H., & Horne, R. N. (2016, 12). Evidence for a transient hydromechanical and frictional faulting response during the 2011 M w 5.6 Prague, Oklahoma earthquake sequence. *Journal of Geophysical Research: Solid Earth*, *121*(12), 8688–8705. doi: 10.1002/2016JB013148

Pearson, C. (1981, 9). The relationship between microseismicity and high pore pressures during hydraulic stimulation experiments in low permeability granitic rocks. *Journal of Geophysical Research: Solid Earth*, *86*(B9), 7855–7864. Retrieved from `http://doi.wiley.com/10.1029/JB086iB09p07855` doi: 10.1029/JB086iB09p07855

Prieto, G., Parker, R., Vernon, F., Shearer, P., & Thomson, D. (2006). Uncertainties in earthquake source spectrum estimation using empirical Green functions. In (pp. 69–74). Retrieved from `http://www.agu.org/books/gm/v170/170GM08/170GM08.shtml` doi: 10.1029/170GM08

Prieto, G., Parker, R., & Vernon III, F. (2009). A fortran 90 library for multitaper spectrum analysis. *Computers & Geosciences*, *35*, 1701–1710.

Prieto, G., Shearer, P., Vernon, F., & Kilb, D. (2004). Earthquake source scaling and self-similarity estimation from stacking P and S spectra. *J. Geophys. Res.*, *109*(8), 1–13. Retrieved from `http://dx.doi.org/10.1029/2004JB003084` doi: 10.1029/2004jb003084

Ruhl, C., Abercrombie, R., & Smith, K. D. (2017). Spatiotemporal Variation of Stress Drop During the 2008 Mogul, Nevada, Earthquake Swarm. *Journal of Geophysical Research: Solid Earth*(1), 8163–8180. Retrieved from `http://doi.wiley.com/10.1002/2017JB014601` doi: 10.1002/2017JB014601

Sato, T., & Hirasawa, T. (1973). Body wave spectra from propagating shear cracks. *Journal of Physics of the Earth*, *21*(4), 415–431. doi: 10.4294/jpe1952.21.415

Savage, H. M., Keranen, K. M., P. Schaff, D., & Dieck, C. (2017, 6). Possible precursory signals in damage zone foreshocks. *Geophysical Research Letters*, *44*(11), 5411–5417. Retrieved from `http://doi.wiley.com/10.1002/2017GL073226` doi: 10.1002/2017GL073226

Schoenball, M., & Ellsworth, W. L. (2017, 12). A Systematic Assessment of the Spatiotemporal Evolution of Fault Activation Through Induced Seismicity in Oklahoma and Southern Kansas. *Journal of Geophysical Research: Solid Earth*, *122*(12), 189–10. Retrieved from `http://doi.wiley.com/10.1002/2017JB014850` doi: 10.1002/2017JB014850

Shaw, B. E., Richards-Dinger, K., & Dieterich, J. H. (2015, 11). Deterministic Model of Earthquake Clustering Shows Reduced Stress Drops for Nearby Aftershocks. *Geophys. Res. Lett.*, *42*(21), 9231–9238. Retrieved from `http://www.nature.com/doifinder/10.1038/368624a0http://doi.wiley.com/10.1002/2015GL066082` doi: 10.1002/2015GL066082

Shearer, P. M., Abercrombie, R. E., Trugman, D. T., & Wang, W. (2019). Comparing EGF Methods for Estimating Corner Frequency and Stress Drop From P Wave Spectra. *Journal of Geophysical Research: Solid Earth*, *124*(4), 3966–3986. doi: 10.1029/2018JB016957

Shearer, P. M., Prieto, G. A., & Hauksson, E. (2006). Comprehensive analysis of earthquake spectral in southern California. *Journal of Geophysical Research-Solid Earth*, *111*(B6). doi: B0630310.1029/2005jb003979

Smith, K. D., & Priestley, K. F. (1993). Aftershock Stress Release Along Active Fault Planes of the 1984 Round Valley, California, Earthquake Sequence Applying a Time-Domain Stress Drop Method. *Bulletin of the Seismological Society of America*, *83*(1), 144–159. doi: 10.1073/pnas.0703993104

Staszek, M., Orlecka-Sikora, B., Leptokaropoulos, K., Kwiatek, G., & Martínez-Garzón, P. (2017). Temporal static stress drop variations due to injection activity at The Geysers geothermal field, California. *Geophysical Research Letters*, *44*(14), 7168–7176. doi: 10.1002/2017GL073929

Sumy, D. F., Cochran, E. S., Keranen, K. M., Wei, M., & Abers, G. A. (2014, 3). Observations of static Coulomb stress triggering of the November 2011

M 5.7 Oklahoma earthquake sequence. *Journal of Geophysical Research: Solid Earth*, *119*(3), 1904–1923. doi: 10.1002/2013JB010612

Sumy, D. F., Neighbors, C. J., Cochran, E. S., & Keranen, K. M. (2017, 5). Low stress drops observed for aftershocks of the 2011 M w 5.7 Prague, Oklahoma, earthquake. *Journal of Geophysical Research: Solid Earth*, *122*(5), 3813–3834. Retrieved from `http://doi.wiley.com/10.1002/2016JB013153` doi: 10.1002/2016JB013153

Sun, L., Zhang, M., & Wen, L. (2016). A new method for high-resolution event relocation and application to the aftershocks of Lushan Earthquake, China. *J. Geophys. Res.*, *121*, 2539–2559. doi: 10.1002/2016JB012840

Sun, X., & Hartzell, S. (2014). Finite-fault slip model of the 2011 Mw 5.6 Prague, Oklahoma earthquake from regional waveforms. *Geophysical Research Letters*, *41*(12), 4207–4213. doi: 10.1002/2014GL060410

Trugman, D. T., Dougherty, S. L., Cochran, E. S., & Shearer, P. M. (2017). Source Spectral Properties of Small to Moderate Earthquakes in Southern Kansas. *Journal of Geophysical Research: Solid Earth*, *122*(10), 8021–8034. doi: 10.1002/2017JB014649

Uchide, T., & Imanishi, K. (2016). Small earthquakes deviate from the omega-square model as revealed by multiple spectral ratio analysis. *Bulletin of the Seismological Society of America*, *106*(3), 1357–1363. doi: 10.1785/0120150322

Viegas, G., Abercrombie, R. E., & Kim, W. Y. (2010). The 2002 M5 Au Sable Forks, NY, earthquake sequence: Source scaling relationships and energy budget. *Journal of Geophysical Research: Solid Earth*, *115*(7), 1–20. doi: 10.1029/2009JB006799

Waldhauser, F., & Ellsworth, W. L. (2000). A Double-difference Earthquake location algorithm: Method and application to the Northern Hayward Fault, California. *Bulletin of the Seismological Society of America*, *90*(6), 1353–1368. doi: 10.1785/0120000006

Walsh, F. R., & Zoback, M. D. (2016, 12). Probabilistic assessment of potential fault slip related to injection-induced earthquakes: Application to north-central Oklahoma, USA. *Geology*, *44*(12), 991–994. Retrieved from `http://geology.gsapubs.org/lookup/doi/10.1130/G38275.1https://pubs.geoscienceworld.org/geology/article/44/12/991-994/195082` doi: 10.1130/G38275.1

Walter, J. I., Ogwari, P., Thiel, A., Ferrer, F., Woelfel, I., Chang, J. C., ... Holland, A. A. (2020, 3). The Oklahoma Geological Survey Statewide Seismic Network. *Seismological Research Letters*, *91*(2A), 611–621. doi: 10.1785/0220190211

Wang, H., Ren, Y., & Wen, R. (2018). Source parameters, path attenuation and site effects from strong-motion recordings of the Wenchuan aftershocks (2008-2013) using a non-parametric generalized inversion technique. *Geo-*

physical Journal International. doi: 10.1093/gji/ggx447

Way, H. S. K. (1983). *Structural study of the Hunton Lime of the Wilzetta Field, T12–13N, R5E, Lincoln County, Oklahoma, pertaining to the exploration for hydrocarbons [M.S. thesis]: Stillwater, Oklahoma State University* (Unpublished doctoral dissertation). Oklahoma State University.

Woessner, J., Schorlemmer, D., Wiemer, S., & Mai, P. M. (2006). Spatial correlation of aftershock locations and on-fault main shock properties. *Journal of Geophysical Research: Solid Earth*, *111*(8), 1–17. doi: 10.1029/2005JB003961

Wu, Q., Chapman, M., & Chen, X. (2018). Stress-drop variations of induced earthquakes in Oklahoma. *Bulletin of the Seismological Society of America*, *108*(3), 1107–1123. doi: 10.1785/0120170335

Yenier, E., Atkinson, G. M., & Sumy, D. F. (2017, 2). Ground Motions for Induced Earthquakes in Oklahoma. *Bulletin of the Seismological Society of America*, *107*(1), 198–215. Retrieved from `https://pubs.geoscienceworld.org/bssa/article/107/1/198-215/351033` doi: 10.1785/0120160114

Yoshida, K., Saito, T., Urata, Y., Asano, Y., & Hasegawa, A. (2017). Temporal Changes in Stress Drop, Frictional Strength, and Earthquake Size Distribution in the 2011 Yamagata-Fukushima, NE Japan, Earthquake Swarm, Caused by Fluid Migration. *Journal of Geophysical Research: Solid Earth*, *122*(12), 379–10. doi: 10.1002/2017JB014334

Zhai, G., Shirzaei, M., Manga, M., & Chen, X. (2019). Pore-pressure diffusion, enhanced by poroelastic stresses, controls induced seismicity in Oklahoma. *Proceedings of the National Academy of Sciences*. doi: 10.1073/pnas.1819225116

Zhang, H., Eaton, D. W., Li, G., Liu, Y., & Harrington, R. M. (2016). Discriminating induced seismicity from natural earthquakes using moment tensors and source spectra Hongliang. *J. Geophys. Res.*, *121*, 972–993. doi: 10.1002/2015JB012603

Zhang, Q., Lin, G., Zhan, Z., Chen, X., Qin, Y., & Wdowinski, S. (2017). Absence of remote earthquake triggering within the Coso and Salton Sea geothermal production fields. *Geophysical Research Letters*. Retrieved from `http://doi.wiley.com/10.1002/2016GL071964` doi: 10.1002/2016GL071964

Zuyuan Liu, Wuenscher, M. E., & Herrmann, R. B. (1994). Attenuation of body waves in the central New Madrid seismic zone. *Bulletin - Seismological Society of America*.

Method	Data	Minimum SNR	Frequency Range
Stacking Method	$P, S, S10$	≥ 3	$2-60$
Joint Spectral Fitting	$S, S10$	≥ 3	$2-80$
Spectral Ratio	P, S	≥ 3	Varies

Table 2.1: Data criteria for each method

Name	Method	Phase Window	Freq Range (Hz)	SNR	Reference
SNSS	Stacking Method	P,S,S10	$2-60$	min ≥ 3	This Study
JS	Joint Spectral Fitting	S,S10	$2-80$	min ≥ 3	This Study
SR	Spectral Ratio	P,S	Varies	≥ 3	This Study
Y17	GMPE^a	P $\geq 40s$	Varies	$\geq$ 2 for any 8 Hz bandwidth	Yenier et al. (2017)
S17	Joint Spectral Fitting	S $\geq 10s$	Varies	Ends of bandwidth ≥ 3 and ≥ 2 any for 8 Hz bandwidth	Sumy et al. (2017)
W18	Spectral Ratios	S-Coda	80% Nyquist	Min ≥ 3	Wu et al. (2018)

Table 2.2: Datasets being compared to this studies results. ^{a} generic ground-motion prediction equation.

Name	Method	Phase Window	Freq Range (Hz)	SNR	Reference
Y17	GMPE^a	P $\geq 40s$	Varies	$\geq$ 2 for any 8 Hz bandwidth	Yenier et al. (2017)
B17	Spectral Ratios	S-Coda	$0.1 - 10$	≥ 2	(Boyd et al., 2017)
C17	Direct f_c	P+S	Varies	Visual Examination	(Cramer, 2017)
S14	FFM^b	P and/or S	$0.2-3.0$ Hz	NA	(X. Sun & Hartzell, 2014)
H17	Spectral Ratio	S 5-15s	0.1-15	NA	(H.-H. Huang et al., 2017)

Table 2.3: Datasets with large f_c estimates for the Foreshock,Mainshock, and Aftershock. ^{a} generic ground-motion prediction equation. ^{b} Finite Fault Model

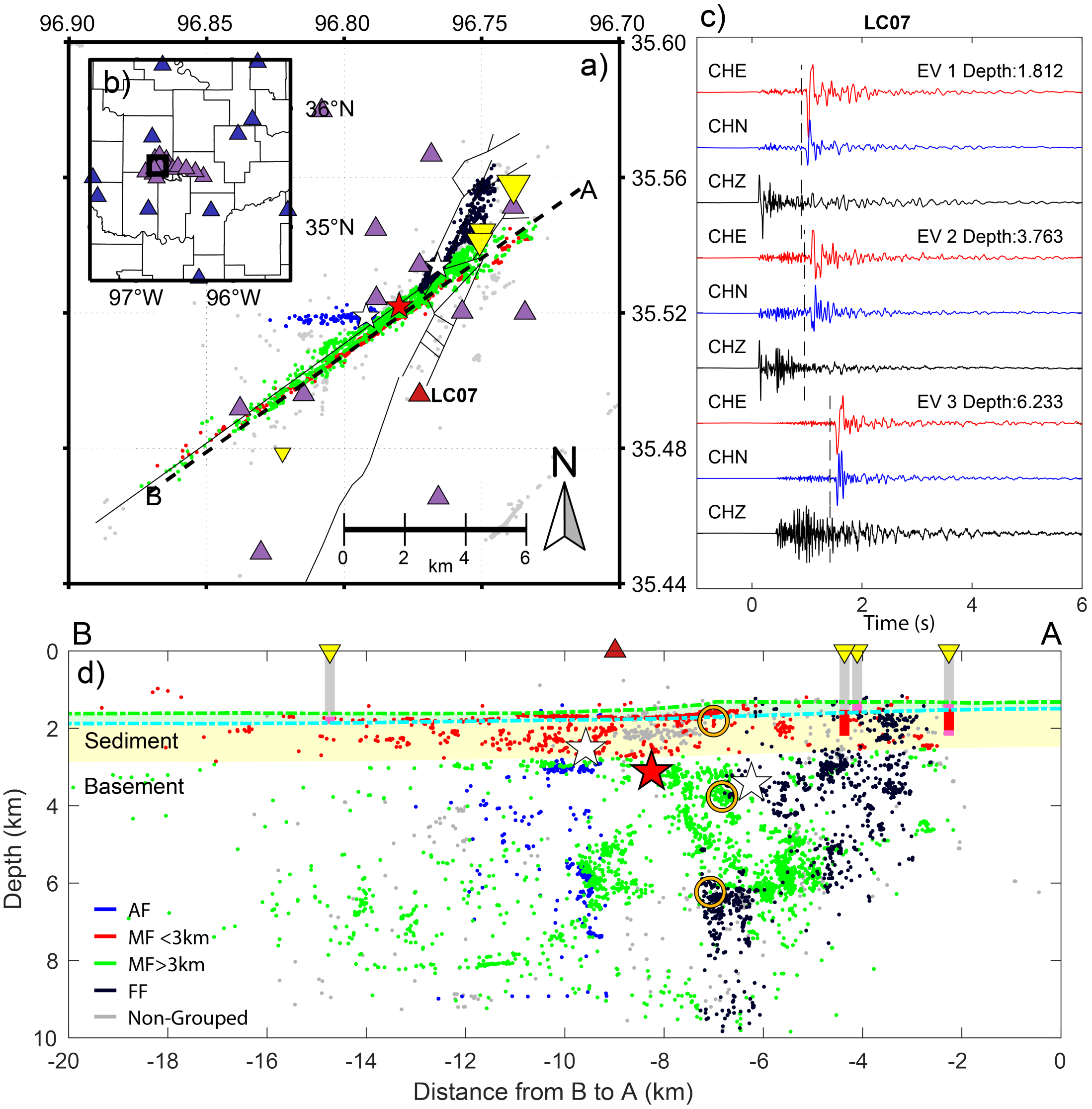

Figure 2.1: (a) Mapview of relocated earthquakes colored by the fault group with which they are associated with the groups being Foreshock fault (FF), Mainshock fault (MF) which is divided between the sediment and basement, and Aftershock Fault (AF) (see legend in (d) for color of each group). 250 Hz stations are purple, lower sampling rate stations are blue. Disposal wells are the inverted yellow triangles, which are scaled by total injected volume. Interpreted faults are drawn with solid lines(black). White stars are the M4.8 foreshock and aftershock, and the red star is the mainshock. (b) Larger map view with location of the study area shown by black square. (c) Example waveforms for earthquakes at different depths at station LC07 (red triangle on map and cross-section). (d) Cross section A-B showing the depth of the Hunton group (green), and the Arbuckle (yellow) sediments; gray rectangles are injection wells with the red portions representing the reported Arbuckle intersection. Orange circles identify the location of the example earthquakes shown in (c).

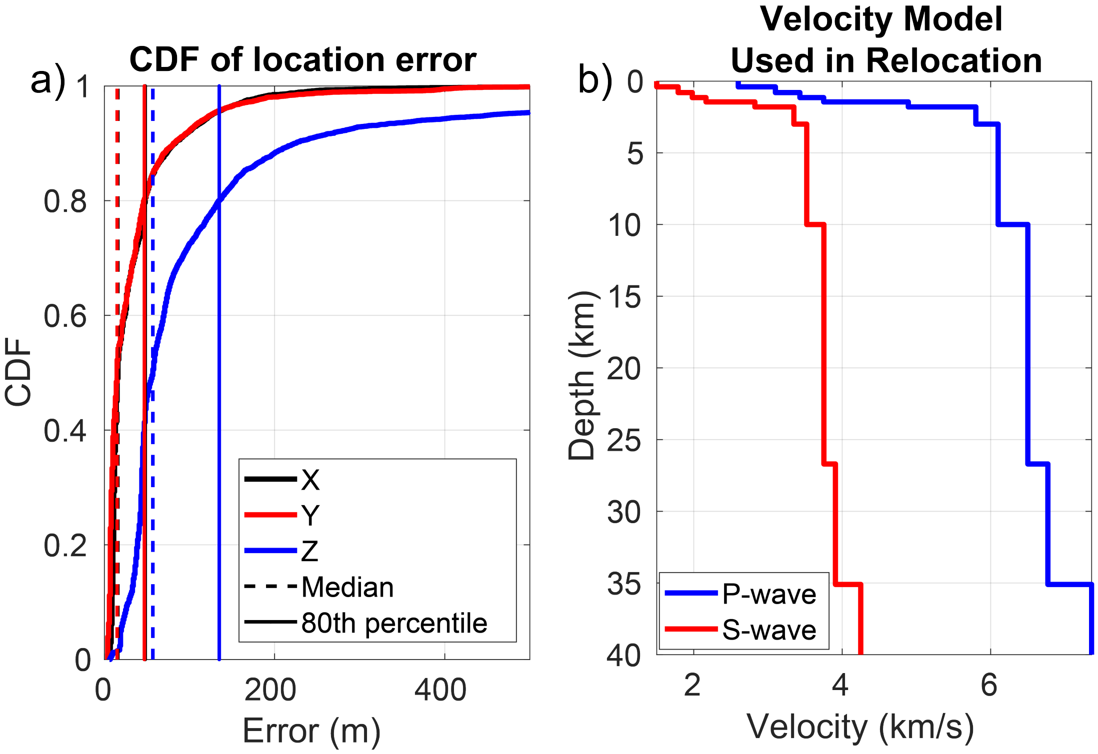

Figure 2.2: (a) Velocity model used in the relocation. See legend for different velocities. (b) CDF plot of relocation error. See legend.

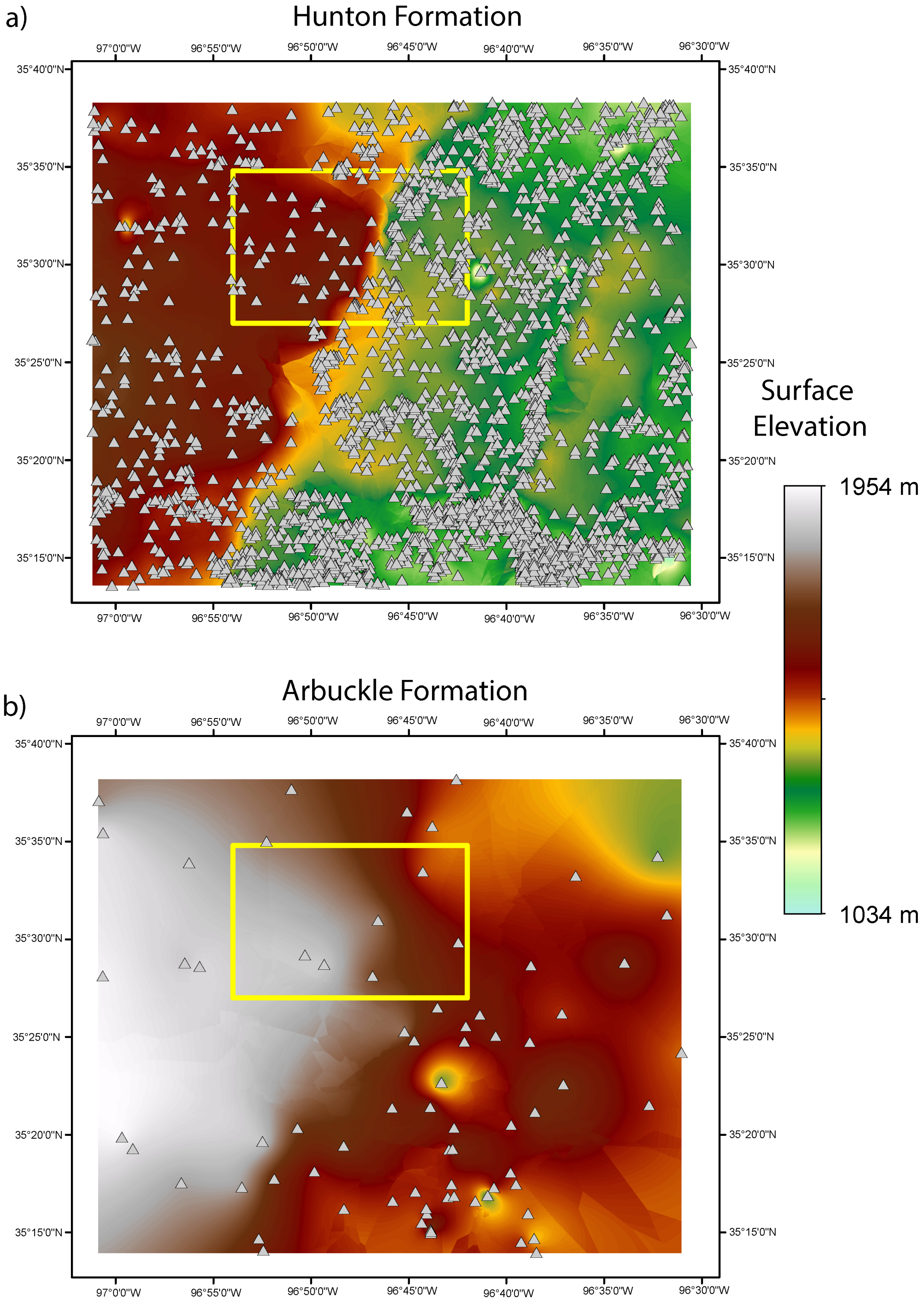

Figure 2.3: Formation depth surfaces generated from wells.(a)Wells used for the Hunton formation depth surface.(b)Wells used for the Arbuckle formation. Wells denoted to as gray triangles and yellow box indicates study area.

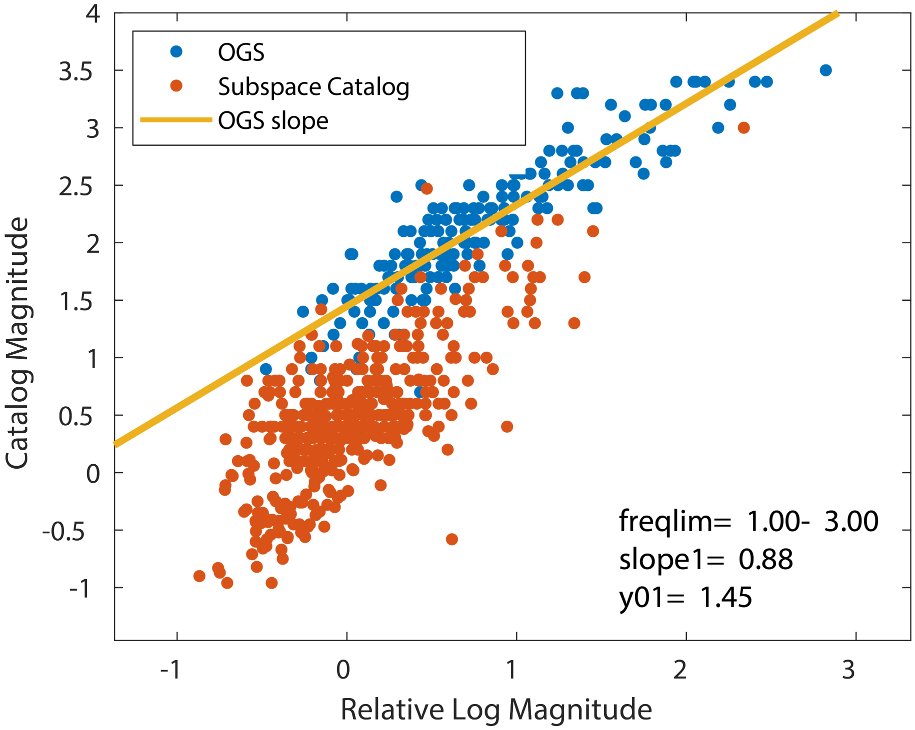

Figure 2.4: Magnitude calibration based upon the OGS values. See legend for description of symbols on figure.

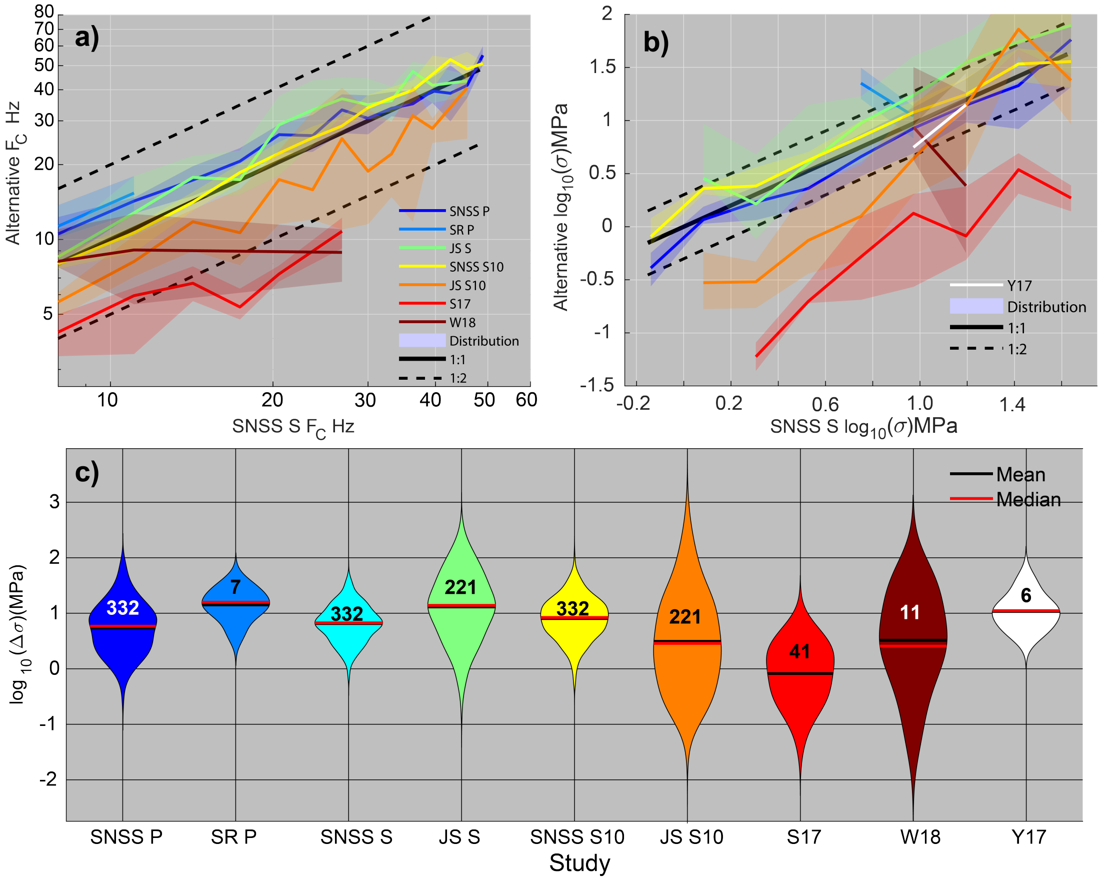

Figure 2.5: Comparison figure of all results and studies with events in common. (a) Comparison of f_c of other results to f_c obtained from the SNSS S method for the same event, line is the median of f_c ranges and transparent region is 75 and 25 quantiles of distribution. See legend for the study associated with the color. Comparison of $\Delta\sigma$ values of other studies vs. SNSS-S estimate. (c) Violin plots showing distributions of stress drops for common events

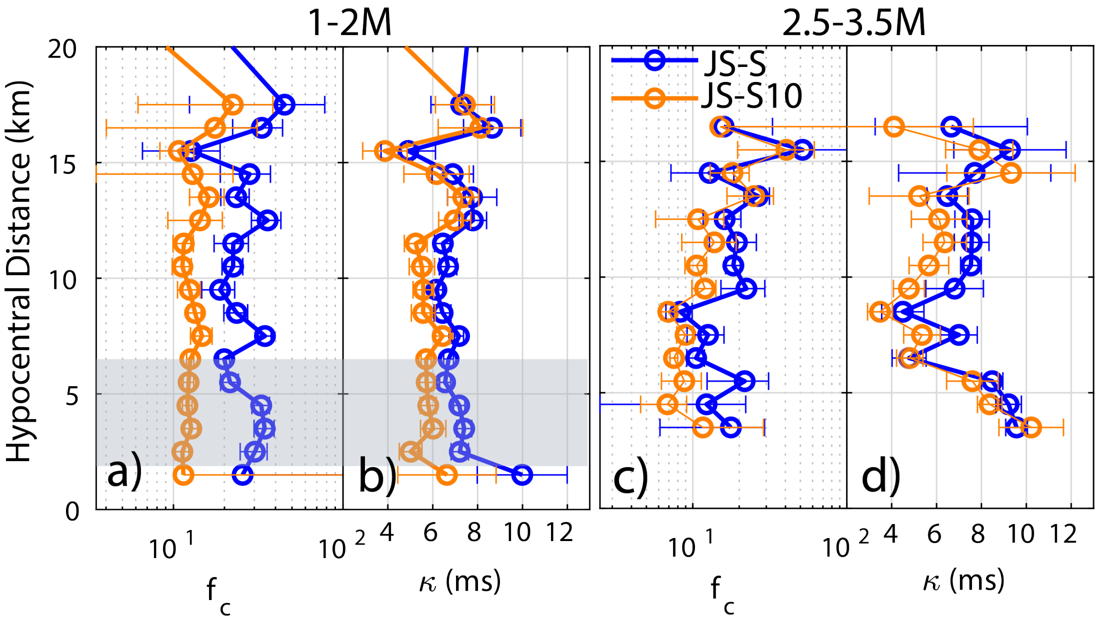

Figure 2.6: The effect of hypocenter distance on f_c and κ for different magnitudes. (a) f_c and κ (b) obtained from JS for the magnitude range of 1-2M plotted against hypocentral distance to station. f_c and κ for the magnitude range of 2.5-3.5 are in (c),(d). Error bars are the 80th and 20th percentile observed for a region while the central dot is the median value. See legend for each line's associated data.

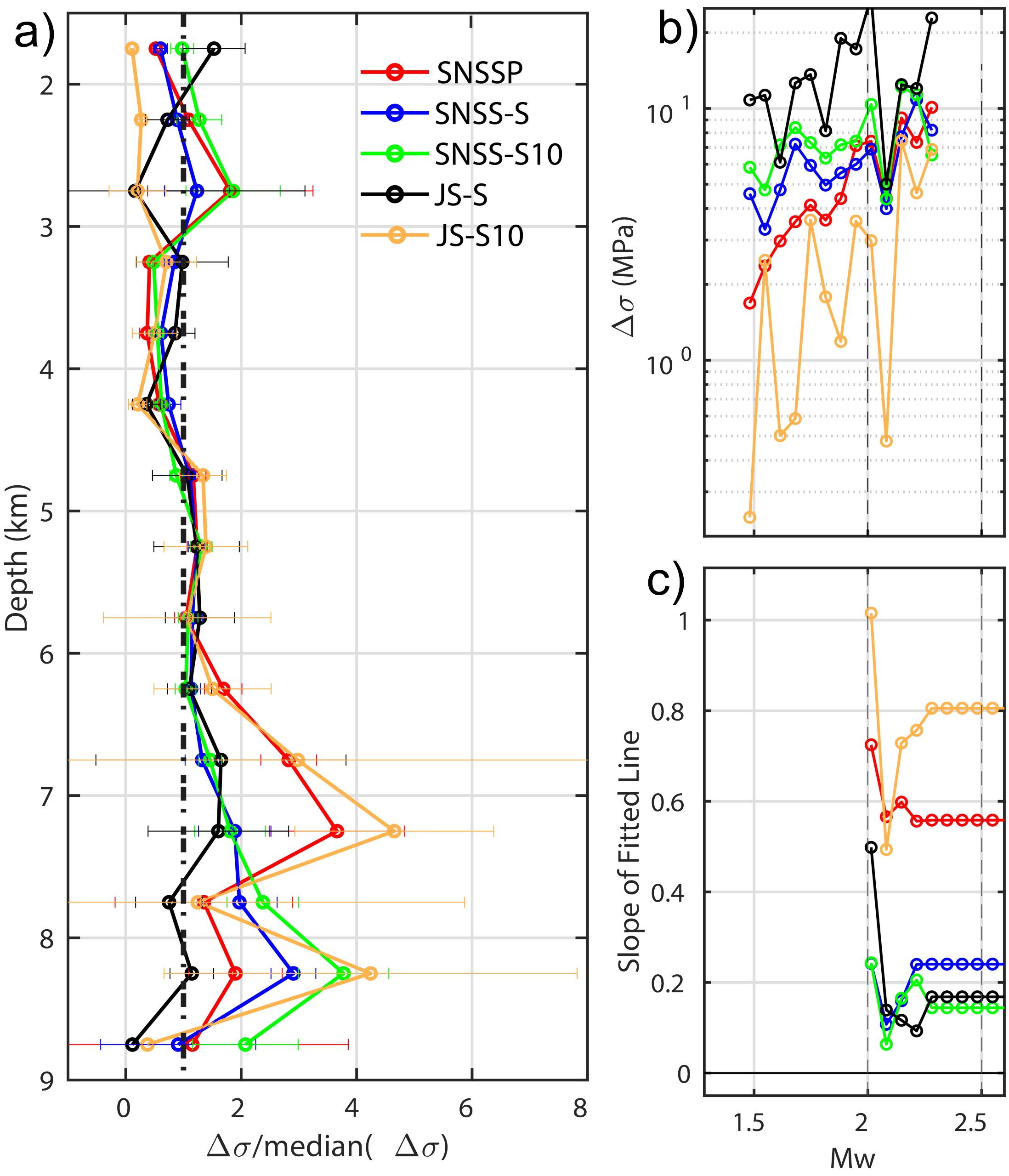

Figure 2.7: Magnitude and depth dependence observed for the stress drop values estimated by this study. (a) Relative change in the stress drops compared to median stress drop for the methods and data sets denoted in the legend. Median stress drop observed in each 0.5 km wide depth bin divided by the median stress drop for the entire sequence (squares).The standard deviation of 100 bootstraps is shown as the error bars. See legend for the associated method/dataset for each line. (b) Median stress drops for each magnitude bin. (c) Slope of a linear model fitted to magnitude range. First data point represents slope of the line fitted to the first 4 points in (b) last point represents model fitted to all points in (b).

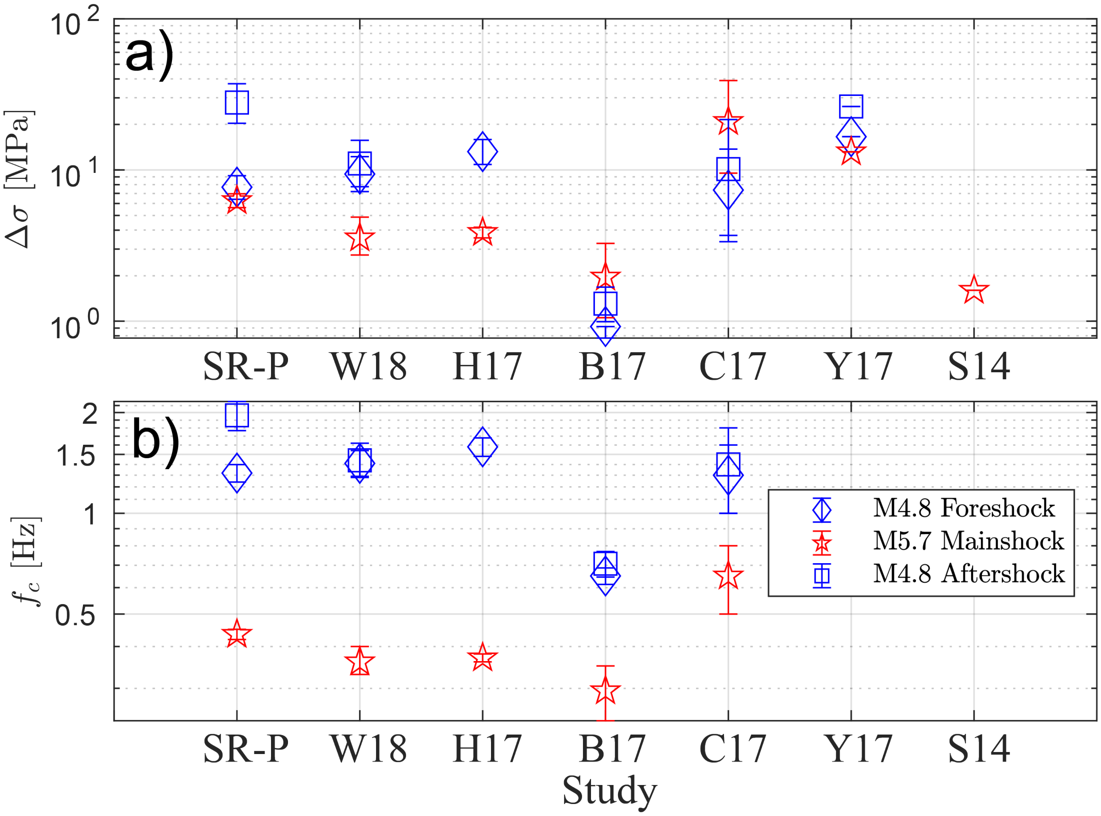

Figure 2.8: Stress drops (a) and corner frequencies (b) for the M4.8 foreshock (diamond) and aftershock (square), and the M5.7 mainshock (star) obtained by this study and previous studies. For those studies that provide an estimation of error for corner frequency estimates this error is represented by the error bars for each group. For each studies citation see Table 2.8.1.

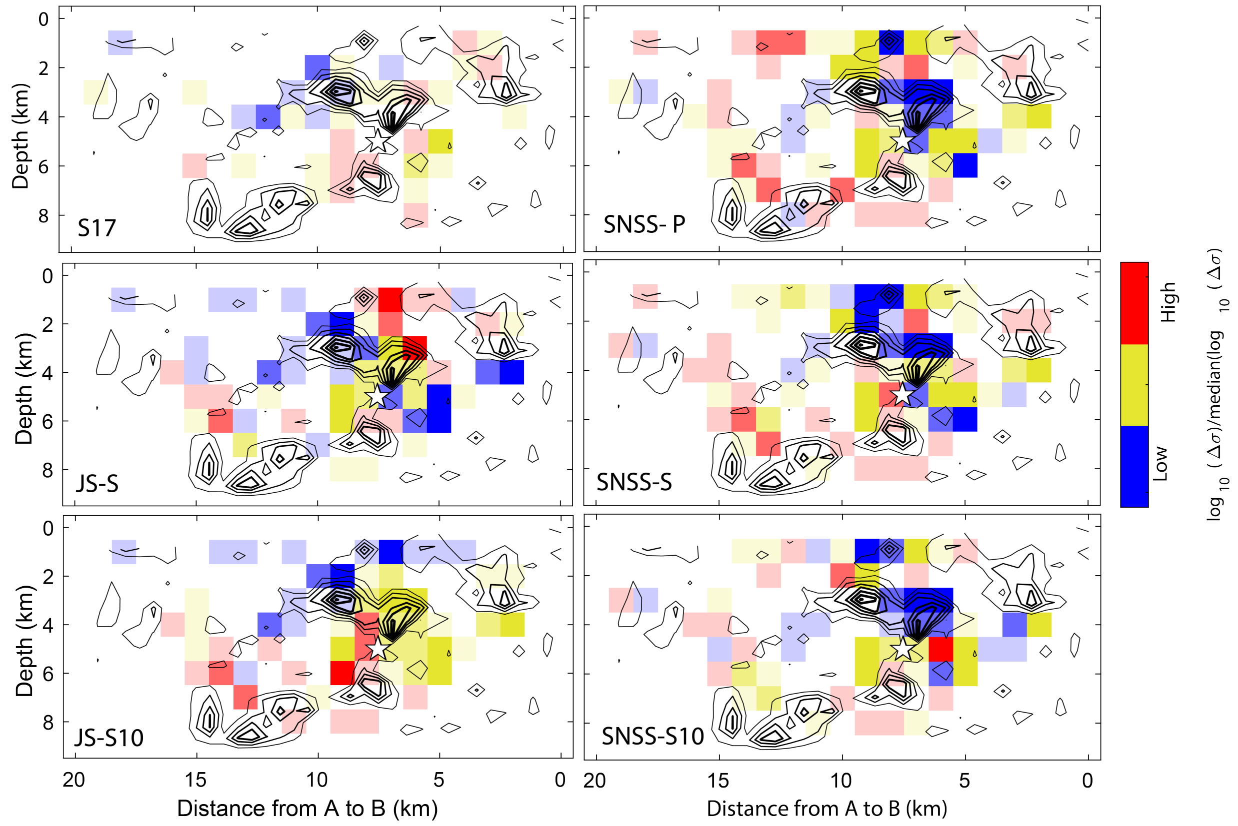

Figure 2.9: Spatial patterns obsereved for normalized stress drops along the mainshocks fault. Each panel compares the results of one stress drop analysis (labeled in bottom left) with the mainshock slip distribution (L. Sun et al., 2016). Grid color is determined by the median value of events inside of the respective grid divided by the median of the entire population. Those grids with more than 5 events are dark in color. Those with less than 5 events are light in color. The median stress drop in each grid is divided by the median value observed for the entire result. Events examined here must be within 400m of cross section A-B in Figure 2.1.

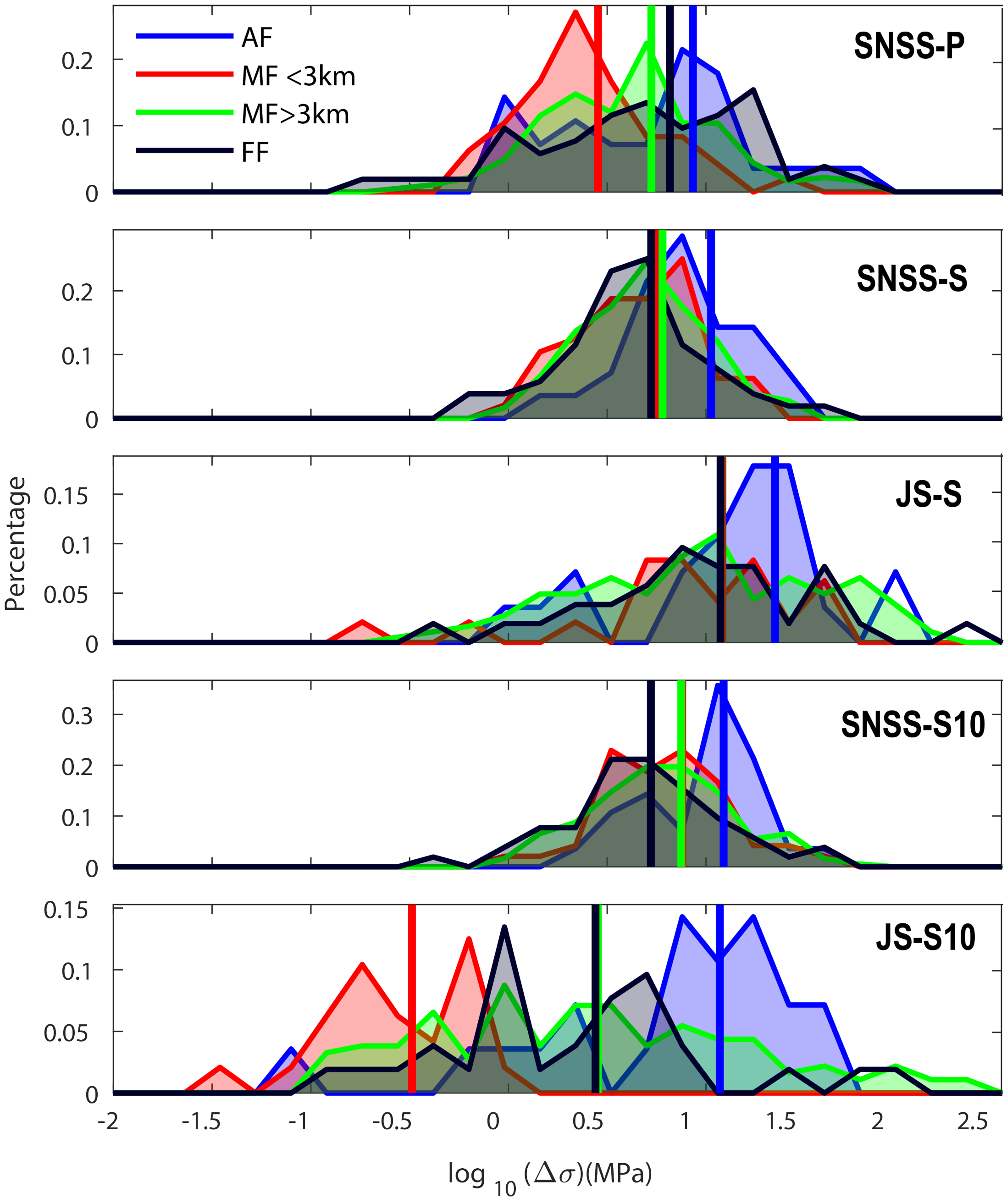

Figure 2.10: Histograms for the stress drop distributions for each fault group shown in Figure 2.1 for the events in common to JS-S,JS-S10, SNSS-P,SNSS-S,SNSS-S10. Median value for each group is denoted by line of the associated color. See legend for the fault group associated with each color

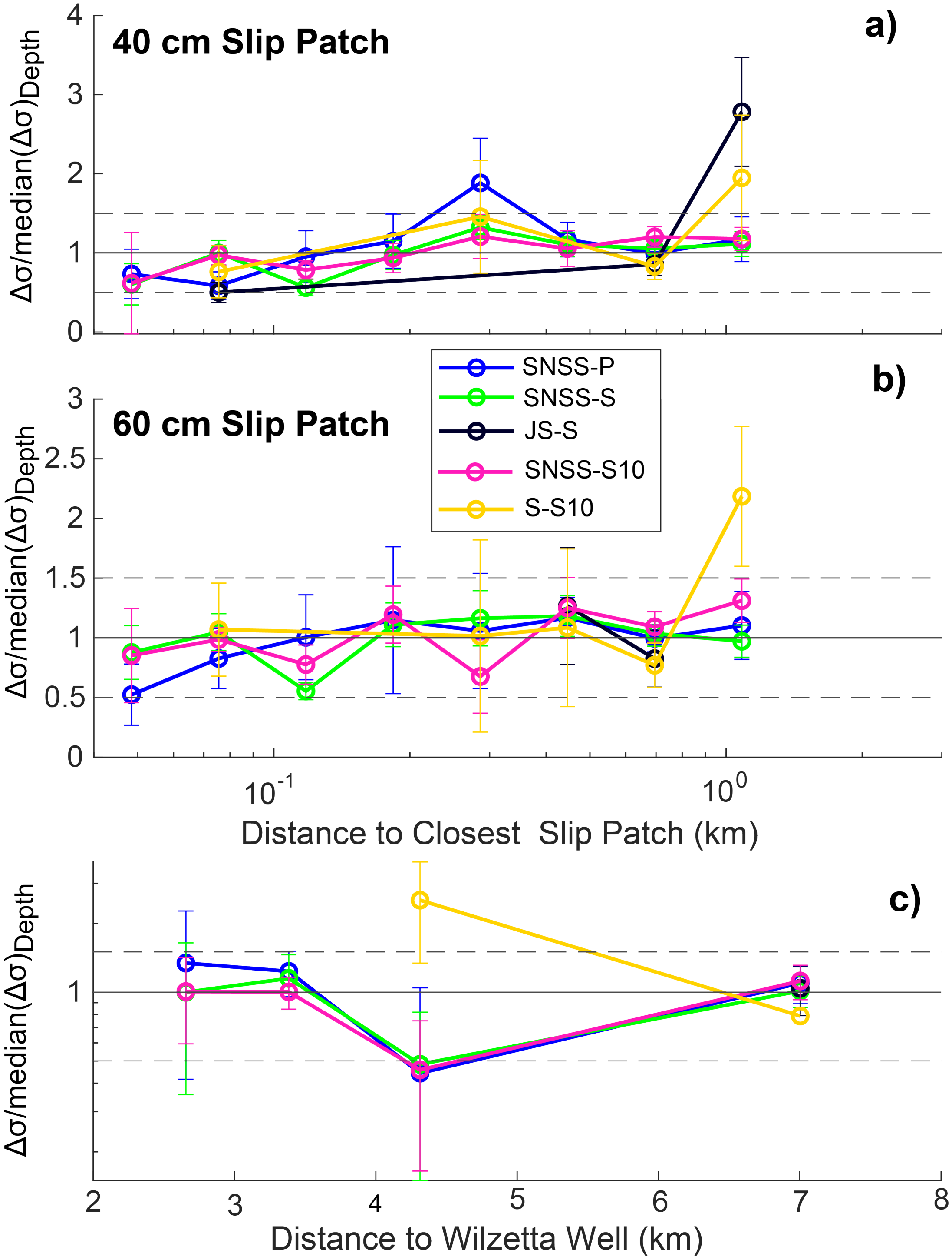

Figure 2.11: Distance from slip patches or injectior vs. the median SDR for a distance range. Error bars are the standard deviation of 100 bootstraps of each bins median estimate.(a) Distance to 40 cm slip patch for events in the MF fault group. (b) Distance to 60cm slip patch for events in the MF fault group. (d) Distance from the Wilzetta injection wells well bottom for events in the FF fault group. See legend for respective study and method.

Chapter 3

Finite Fault Inversion of Mw4.1 and its Implications for Induced Earthquake Ruptures.

3.1 Abstract

To better quantify how injection, prior seismicity and fault properties control a earthquake rupture's growth and propagation we perform a finite-fault slip inversion for a M_w 4.1 earthquake that occurred in a waste-water driven earthquake sequence near Guthrie, OK in April 2015. The slip inversion reveals a complex rupture with multiple slip patches which are anti-correlated to the slip of prior seismicity. This indicates that M_w 4.1 earthquake likely ruptured relatively strong locked segment of the fault, while earlier seismicity, which is likely driven by pore pressure changes, occurred in weaker areas. When comparing Oklahoma earthquake slip patterns to events in swarm like sequences in other regions, intraplate earthquakes in Oklahoma have a higher number of well separated slip patches,

indicating a difference in fault characteristics between regions. From these observations we conclude that both pore pressure perturbations, earthquake interactions, and fault characteristics control rupture propagation in moderate size earthquakes in Oklahoma, with the latter likely the dominant factor.

3.2 Introduction

The central United States has experienced a significant increase in seismicity rates since 2009, which has been largely attributed to waste-water injection (Ellsworth, 2013; Keranen et al., 2014). It is well understood that the stress perturbations produced from waste-water injection reactivate pre-existing faults, which leads to an increase in earthquake occurrence. Fault structure, stress changes due to injection, and stress interactions between earthquakes play major roles in the spatiotemporal evolution of individual sequences (M. Brown & Ge, 2018; Pennington & Chen, 2017; Qin et al., 2018; Sumy et al., 2014). What is not well understood is how these factors affect the nucleation and rupture growth of future earthquakes within individual induced earthquake sequences. Investigation of their roles in controlling the propagation of future ruptures in a sequence is needed to not just better understand the underlying physics that govern rupture growth, but also the proper assessment of seismic hazard.

Previous investigations of coseismic slip for induced earthquakes have observed both spatial and temporal phases in slip growth. The 2011 Prague earthquake contained multiple slip patches (X. Sun & Hartzell, 2014), and rupture models of the 2016 Pawnee earthquake showed multiple peaks of slip and moment release (Grandin et al., 2017; Moschetti et al., 2019). Previous studies have shown that the nucleation of these events was affected by prior seismicity and injection, so these two factors could play a role in these events' rupture processes (Sumy et al., 2014; Pennington & Chen, 2017; Chen et al., 2017; Norbeck & Horne, 2016). Due to lack of significant prior seismicity on the fault plane for both of these events, it makes it difficult to assess the relationship between prior seismicity and coseismic slip. Moreover an examination by (Moschetti et al., 2019) of the Pawnee earthquake did not find agreement between modeled pore pressure change along the fault and the location of its slip patches. On the other hand, the non-induced intraplate 2011 M_w 5.8 Mineral Virginia earthquake also has multiple slip patches (Hartzell et al., 2013). This indicates that the fault properties of these long dormant faults might also play an important role controlling coseismic slip patterns.

To better quantify how pore pressure and earthquake interactions affect earthquake rupture propagation, we examine the largest earthquake (M_w 4.1) of the Guthrie sequence that occurred about nine months following fault reactivation. The sequence shows overall temporal correlation with the injection rate of nearby wells, indicating that injection could be driving the sequence (Chen et al., 2018; Haffener et al., 2018). The subevent modeling by Wu et al. (2019) of the M_w 4.1 indicates a complex failure that contains 5 subevents, which indicates a complex triggering and rupture process. In this study, we model the spatial and temporal evolution of the M_w 4.1 earthquake rupture and its relationship with prior seismicity to better understand the nucleation and triggering of large events during induced earthquake sequences. We quantify the distribution of asperities based on spatial gridding analyses and compare with other M4-5 earthquakes in both induced and natural earthquake sequences, to better constrain the control factors of earthquake rupture complexity from different tectonic environments.

3.3 Data:

The sequence is comprised of 936 events which were analyzed in detail and relocated by Chen et al. (2018); Chen and Abercrombie (2020). The sequence started in early 2014 and intensified in July 2014 following an injection rate increase from nearby disposal wells, and gradually decreased in activity following the shut-in of nearby wells in May 2015. A majority of the sequence occurred on two parallel 4 km long SE tending faults, which are bisected by an orthogonal fault trending to the NE (Benz et al., 2015; Chen et al., 2018) (Figure 3.1a). The M_w 4.1 occurred on April 8,2015 at 16:51:13 (UTC) along the main fault trending to SE, 10 months after seismicity began on that fault.

Due to the small magnitude of the target event a smaller magnitude co-located earthquake is chosen to be used as an empirical Greens Function (EGF) (Hartzell, 1978). The EGF event chosen is a M3.1 earthquake that occurred on September 15, 2014 at 00:10:38 (UTC), which has similar focal mechanism with the target event and was previously used in the temporal deconvolution of Wu et al. (2019). We download waveform data from Incorporated Research Institutions for Seismology (IRIS) data management center for 23 stations within 75 km of the target event and manually pick both P and S phases. Data utilized in the inversion are required to have: >2 s S-P travel time, an impulsive first motion, $\geq$ 100 Hz sampling rate, and a signal to noise ratio $\geq$ 10. 11 out of the original 23 stations pass these criteria and are utilized in the inversion (Figure 3.1c).

Only the P-wave is used for the finite slip inversion analysis of the target earthquake. This is based on the results from Wu et al. (2019) that the small initial sub-event is masked in the S-wave arrival by the P-wave's coda. The waveforms for the target and the EGF earthquakes are integrated to displacement, band-pass-filtered between 1 and 10 Hz, resampled to 100 Hz, and normalized by the maximum absolute value of the target earthquake for each component. The data was cut 0.5 seconds before the P arrival and 2.5 seconds after, with the exception of STN03 which was closer in distance to the target event and was cut to 2.2 seconds. The channels utilized in the inversion process are the vertical component and the horizontal channel with highest amplitude. Due to the horizontal channels having lower signal to noise they are given half of the weight of the vertical components in the inversion.

3.4 Method:

To constrain the slip of the M_w 4.1 earthquake, we apply a linear slip inversion method (Hartzell & Heaton, 1986; Uchide & Ide, 2007) based on empirical Green's Function (EGF) (Hartzell, 1978). The workflow from Uchide and Song (2018) is followed to perform the inversion:

1. The creation of the fault model over which the spatio-temporal slip distribution will be calculated. We estimate the fault orientation using the target earthquakes focal mechanism and the distribution of aftershocks and find a strike, dip and rake of 301° , 81° , and -10° respectively, which agrees with the directivity estimate of 126.3° (Wu et al., 2019). We base the extent of the fault model on the locations of the sub-events found in the modeling by Wu et al. (2019), and refine it through trial and error. The final fault model is 4 km long (along strike) and 4 km wide (along dip), and the earthquake hypocenter is located 0.5 km along strike and 2 km along dip (Figure 3.2a).
2. A linear cubic B-spline function is chosen as the basis function to describe

the spatiotemporal slip-distribution. The basis function has spatial nodes along the fault at intervals of 0.25 km and at 0.1 s intervals in time. The expansion coefficients controlling the amplitude of the basis function are the unknown parameters and will be estimated during the inversion. To reduce the number of parameters that are being solved for, the start time of the first temporal basis function at each grid point is set to a time when the rupture reaches that point and is restricted to 0.5 s in length. This assumes a causality between the rupture front and onset of slip and introduces the unknown parameter of hypothetical rupture velocity V_{hr}.

3. The determination of a hypothetical rupture velocity V_{hr}. The V_{hr} controls when the rupture arrives at a grid point and therefore should be faster than the true rupture velocity. In order to determine the optimal V_{hr} we perform the inversion with multiple velocities from 1.6 km/s to 4.4 km/s at an interval of 0.2 km/s. The model performance is measured by the variance reduction observed between the synthetic and observed waveforms defined as $1 - Var(d_{obs} - d_{syn})/Var(d_{obs})$, where Var is variance and d_{syn} and d_{obs} are the synthetic observed waveforms.

4. In the final step we solve for the unknown expansion coefficients controlling the amplitude of the basis function using a non-negative least squares algorithm (Lawson & Hanson, 1987). In order to reduce the difference between the coefficients of spatio-temporally neighboring basis functions and aid in the convergence toward a solution, we introduce a temporal smoothing constraint. This assumes that the rupture process progresses in a relatively smooth manner. The intensity of this smoothing constraint we consider a hyperparameter in Bayesian modeling and find through the minimization

of Akaike's Bayesian information criterion (Akaike, 1980; Ide, 2001; Uchide & Ide, 2007; Uchide & Song, 2018; Yabuki & Matsu'ura, 1992).

3.5 Results:

Figure 3.2 depicts the results for the M_w 4.1 earthquake. The estimated models produce good agreement between observed and the generated synthetic waveforms with a variance reduction of 73.9%. This result was obtained using a V_{hr} of 3.2 km/s, which is the velocity where improvement in variance reduction is < 0.01. This value falls within the range of 3.0 km/s and 3.5 km/s found in other studies using the same method (Uchide & Song, 2018), but is higher than the 1.6 - 1.8 km/s found for this event by Wu et al. (2019).

The resolved moment is 3.25×10^{15} Nm, which is equivalent to a M_w 4.3. The seismic moment and amount of fault slip are estimated as relative values to the EGF event's moment and would decrease if it had a lower magnitude. To test the robustness of the moment, alternative M2.1 EGF was tested, which produced a similar seismic moment and slip distribution but had lower variance reduction.

The source time function shown in Figure 3.2c has a total duration of 1.1 seconds and 3 distinct moment rate pulses. Figure 3.2d shows detailed spatiotemporal evolution of the rupture process: (1) rupture initiated around the hypocenter with the first small pulse; (2) after a gap of 0.1 s, the 2nd larger slip patch starts with 250 m of the first, which gradually propagate along strike; (3) at about 0.5 s, rupture propagates to a 3rd slip patch at deeper depth; (4) at about 0.7 s, a 4th slip patch adjacent to the 2nd patch is activated. The along-strike locations of these slip patches closely align with the previous sub-event modeling done by Wu et al. (2019), with the exception of one of the slip patches in our model occurring at a deeper depth.

Based on the estimated slip model, the stress drop distribution is calculated using the code from Okada et al. (2000) (Figure 3.2b). Maximum stress drop of 4.6 MPa occurred during the 3rd slip patch at deeper depth. The 1st, 2nd, and 4th slip patches experienced peak stress drops of 1.8, 4.2, 3.2 MPa, respectively. The average stress drop from grids with stress drop above 0.5 MPa is 1.6 MPa, which is lower than the values of 3.4 to 3.9 MPa obtained by other studies (Wu et al., 2019; Chen & Abercrombie, 2020). The slip model's stress drop values are highly dependent on the spatial resolution of the grid, and so the values of peak stress drop should be considered the lower bound of actual values.

3.6 Discussion:

3.6.1 The Role of Prior Seismicity and Injection on Rupture Propagation.

It has been observed in other swarms that the slip of prior seismicity often outlines the slip of future events (Ide, 2002). To investigate the relationship between cumulative slip from prior seismicity and the largest event, we first estimate the rupture radius of earlier earthquakes within 200 m of the modeled fault plan based on the equation: $r = (0.32\beta)/f_c$ (Eshelby, 1957; Madariaga, 1976), where f_c is the corner frequency, and β is 3.35 km/s, which is the S-wave velocity between 1.5 and 8 km depth. This assumes a simple circular rupture, which may differ from actual rupture area. Then, we calculate cumulative stress drop within the fault zone for each location by adding stress drops from events with overlapping rupture areas. The corner frequency (f_c) and stress drop ($\Delta\sigma$)

values for each event are obtained from S-wave spectral analysis in Chen and Abercrombie (2020). The results of this analysis are plotted in Figure 3.3. The key observations include:

1. Slip from previous earthquakes primarily concentrates within the gap between the deeper and shallower slip patches (Figure 3.3). The abundance of seismicity and stress release in that region likely inhibited significant amount of slip during the largest event. The accumulated stress changes from these smaller events at deeper depth may have promoted activation of the 3rd slip patch during the largest event (M. Brown & Ge, 2018).

2. Those events that do overlap with the slip model are among the earliest earthquakes to occur and have relatively lower stress drop, coinciding with the low stress drop area between the 2nd and 4th slip patches during the largest earthquake (Figure 3.3a). This is similar to findings for other swarms where stress drops are often lower for overlapping events that occur after previous earthquakes (Ide, 2002).

3. These observations suggest that slip from early events can influence the slip distribution of a later larger event, suggesting importance of earthquakes themselves in sequence evolution and rupture propagation. The median relative location errors from Chen et al. (2018) is estimated to be 10m horizontally and 20m vertically with over 90% of events having location errors within 100m. Although the absolute locations can be systematically shifted, the relatively spatial patterns shown in Figure 3.3 should be robust.

Without detailed pore pressure change modeling on the fault's surface, which is beyond the scope of this paper, it is not possible to isolate the effects of pore pressure on slip distribution of an earthquake. Certain attributes of the finite slip model can be linked to pore pressure changes based on past studies that performed modeling (Galis et al., 2017; Norbeck & Horne, 2016) and rupture directivity analysis (Lui & Huang, 2019; Folesky et al., 2016). These studies show that in general, rupture tends to propagate away from the area of injection when the absolute pore pressure perturbation is relatively low. When pore pressure perturbations are high, the rupture tends to propagate towards the injection area, for example, the 2016 M_w 5.1 Fairview earthquake propagated towards high-rate injection zones (Lui & Huang, 2019). The cause of this behavior is suggested to be due to the difference in fault strengths inside and outside the pressure front with higher fault strengths ahead of the pore-pressure front acting as a barrier to a large ruptures propagation away from the injector and therefore biasing its propagation to be back towards the injector (Dempsey & Suckale, 2016; Yoshida et al., 2019).

Due to the relatively low injection volume from nearby disposal wells (within 5 km), the cumulative pore pressure change within the Guthrie fault is only about 0.003 MPa, much lower than pressure modeling from other regions (Chen et al., 2018). Despite the relatively low-pressure change, the diffusive migration of seismicity away from earliest seismicity suggest pressure diffusion within the fault zone (Figure 3.3a). Therefore, the first sub-event is likely initiated due to accumulated pore pressure. The rupture propagation away from possibly dominating disposal well is consistent with the mechanical model proposed in Galis et al. (2017).

3.6.2 Rupture Complexity

The well separated slip patches of the Guthrie M_w4.1 earthquake resemble the finite rupture model of the 2011 Prague and one of the models of 2016 Pawnee earthquake (X. Sun & Hartzell, 2014; Grandin et al., 2017). These events all exhibit complex cascading ruptures where multiple separated slip patches combine to produce a large magnitude earthquake (Ellsworth & Beroza, 1995). Rupture complexity for global large magnitude earthquakes shows spatial coherency and correlation with local geological structures (Ye et al., 2018). While we observe the influence of prior seismicity on the slip distributions of the Guthrie earthquake, this is not well observed for the Prague and Pawnee earthquakes. We hypothesize that the complex slip patterns of Oklahoma induced earthquakes may likely be due to intraplate faults with low tectonic loading rates having higher fault zone heterogeneity.

To test this hypothesis, we compare the slip complexity observed in events in Oklahoma with other similar sized earthquakes from other tectonic environments, ideally strike-slip earthquakes that occur in swarm-like sequences. The tectonically driven events we compare them to are 7 earthquakes from 1998 Hida-Mountains Swarm sequence in Japan (Ide, 2001) and the two largest events that occurred in the 2012 Brawley swarm in Imperial Valley, California (Wei et al., 2013). These events are chosen because they are strike-slip events and occur in swarm-like sequences that were driven by static stress changes and induced or natural pore pressure change (Aoyama, 2002; Wei et al., 2015). We obtain slip models for the 9 earthquakes, which have a magnitude range of 4.1 - 5.4 from the finite fault database SRCMOD (Mai & Thingbaijam, 2014). We compared these events to the Guthrie M_w 4.1 and the Prague M_w 5.6 (L. Sun et al., 2016) slip models, but not the Pawnee $M_w5.6$ because it has multiple conflicting slip models (Grandin et al., 2017; Moschetti et al., 2019).

In order to quantify the number and the characteristics of the slip patches that occur in each model we take a similar approach to Somerville et al. (1999). First we trim the model to contain only the region where a majority of slip occurred by removing the edges of the finite fault model that have a mean slip less than half the entire model's mean slip. We then isolated the grid points that have slip values greater than or equal to the 80th percentile of the slip distribution of the trimmed fault. We then group these grid points using the method of Haralick and Shapiro (1992) and a criterion of 4-way connectivity, which means that if grid points are connected either vertically or horizontally they are grouped together. Of the final groups we remove those with fewer than 2 grid points.

The number of slip patches observed for each earthquake can be found in Table 3.1 and their individual plots in supplemental Figure 3.4. In each region the average number of slip patches observed per earthquake is roughly 7, 2, 2 for Oklahoma, Brawley Swarm and the Hida-Mountain Swarm respectively. For each slip patch we calculate its area as a fraction of the total area of the trimmed model (normalized area), and its slip as a fraction of the average slip over the trimmed fault (normalized slip). In Oklahoma, the normalized area of the slip patches is significantly smaller than what is observed in Hida and Brawley (Figure 3.5 bottom). The normalized slip of the slip patches is highest for Oklahoma (2 to 3), while relatively smaller for Brawley (1.5 to 2.5) and Hida (1 to 2) (Figure3.5 top). This suggests that the slip for Hida and Brawley earthquakes is more diffuse and covers more of the rupture area. In contrast, Oklahoma earthquakes tend to have slip concentrated in small or isolated patches. These differences between induced intraplate earthquakes in Oklahoma and induced/natural earthquakes at plate boundaries suggest that the dormant faults in intraplate regions might exhibit different behavior from plate boundary regions, and ruptures in intraplate regions may be more complex than similar magnitude non-intraplate events. We should note that the sample size is relatively small due to limited slip models for M4-5 strike-slip earthquakes and resolution of the models differs between studies, the later of which could limit the number of isolated slip patches (L. Brown et al., 2015). Future studies of more systematic comparisons can further address this hypothesis.

3.7 Conclusion:

The finite slip inversion indicates that moderate sized earthquakes in Oklahoma have complex ruptures with multiple slip patches existing in their models. In our analysis we found the following:

- The Guthrie earthquakes high slip patches are surrounded by prior seismicity indicating that the slip patches likely represent relatively stronger segments of the fault.
- Most earthquakes in Oklahoma exhibit cascading failure with multiple asperities being triggered during a rupture.
- The cascading failure of asperities in M 4.1 earthquake in Guthrie can be attributed to both fault characteristics, prior seismicity, and to injection.

We find that both pore pressure perturbations, earthquake interactions, and heterogeneity in the distribution of locked regions of fault control rupture propagation in moderate size earthquakes in Oklahoma. This heterogeneity in the distribution of locked patches appears to be more pronounced in intraplate regions. In order to properly understand the potential magnitude ranges we could expect from a fault in Oklahoma a understanding of how dormant intraplate faults differ from those at plate boundaries is required.

3.8 Acknowledgments

This work is partially supported by NSF award 1547071, and graduate student scholarship from the University of Oklahoma. The waveform data used in this study are were obtained from the IRIS Data Management Center (`https://ds.iris.edu/ds/nodes/dmc/`). The finite fault slip inversions of the Hida and Brawley earthquakes are downloaded from the SRCMOD Earthquake Finite Fault Database (Mai & Thingbaijam, 2014). The Prague earthquakes finite fault model was obtained directly from X. Sun and Hartzell (2014). The datasets for relocated catalog and stress drop estimates are available from Chen et al. (2018) and Chen and Abercrombie (2020)

References

Akaike, H. (1980, 2). Likelihood and the Bayes procedure. In J. Bernardo, M. De Groot, D. Lindley, & A. Smith (Eds.), *Bayesian statistics* (pp. 143–166). Calencia, Spain: University Press.

Aoyama, H. (2002). Evolution mechanisms of an earthquake swarm under the Hida Mountains, central Japan, in 1998. *Journal of Geophysical Research*, *107*(B8). doi: 10.1029/2001jb000540

Benz, H. M., Mcmahon, N. D., Aster, R. C., McNamara, D. E., & Harris, D. B. (2015). Hundreds of Earthquakes per Day: The 2014 Guthrie, Oklahoma, Earthquake Sequence. *Seismological Research Letters*, *86*(5), 1318–1325. doi: 10.1785/0220150019

Brown, L., Wang, K., & Sun, T. (2015). Static stress drop in the Mw 9 Tohoku-oki earthquake: Heterogeneous distribution and low average value. *Geophysical Research Letters*, *42*(24), 10595–10600. doi: 10.1002/2015GL066361

Brown, M., & Ge, S. (2018, 6). Small Earthquakes Matter in Injection-Induced Seismicity. *Geophysical Research Letters*, *45*(11), 5445–5453. doi: 10.1029/2018GL077472

Chen, X., & Abercrombie, R. E. (2020). Improved approach for stress drop estimation and its application to an induced earthquake sequence in Oklahoma. *Geophysical Journal International*, *223*(1), 233–253. doi: 10.1093/gji/ggaa316

Chen, X., Haffener, J., Goebel, T. H., Meng, X., Peng, Z., & Chang, J. C. (2018). Temporal Correlation Between Seismic Moment and Injection Volume for an Induced Earthquake Sequence in Central Oklahoma. *Journal of Geophysical Research: Solid Earth*. doi: 10.1002/2017JB014694

Chen, X., Nakata, N., Pennington, C., Haffener, J., Chang, J. C., He, X., ... Walter, J. I. (2017, 12). The Pawnee earthquake as a result of the interplay among injection, faults and foreshocks. *Scientific Reports*, *7*(1), 4945. doi: 10.1038/s41598-017-04992-z

Dempsey, D., & Suckale, J. (2016). Collective properties of injection-induced earthquake sequences: 1. Model description and directivity bias. *Journal of Geophysical Research: Solid Earth*, *121*(5), 3609–3637. doi: 10.1002/2015JB012550

Ellsworth, W. L. (2013, 7). Injection-Induced Earthquakes. *Science*, *341*(6142), 1225942–1225942. doi: 10.1126/science.1225942

Ellsworth, W. L., & Beroza, G. C. (1995, 5). Seismic Evidence for an Earthquake Nucleation Phase. *Science*, *268*(5212), 851–855. doi: 10.1126/science.268.5212.851

Eshelby, J. D. (1957). The determination of the elastic field of an ellipsoidal inclusion, and related problems. *Proc. R. Soc. London, Ser. A,*, *241*, 376–396.

Folesky, J., Kummerow, J., Shapiro, S. A., Häring, M., & Asanuma, H. (2016). Rupture directivity of fluid-induced microseismic events: Observations from an enhanced geothermal system. *Journal of Geophysical Research: Solid Earth*, *121*(11), 8034–8047. doi: 10.1002/2016JB013078

Galis, M., Ampuero, J. P., Mai, P. M., & Cappa, F. (2017). Induced seismicity provides insight into why earthquake ruptures stop. *Science Advances*. doi: 10.1126/sciadv.aap7528

Grandin, R., Vallée, M., & Lacassin, R. (2017, 7). Rupture Process of the M w 5.8 Pawnee, Oklahoma, Earthquake from Sentinel-1 InSAR and Seismological Data. *Seismological Research Letters*, *88*(4), 994–1004. doi: 10.1785/0220160226

Haffener, J., Chen, X., & Murray, K. (2018, 9). Multi-scale analysis of spatiotemporal relationship between injection and seismicity in Oklahoma. *Journal of Geophysical Research: Solid Earth*. doi: 10.1029/2018JB015512

Haralick, R. M., & Shapiro, L. G. (1992). *Computer and Robot Vision* (1st ed.). USA: Addison-Wesley Longman Publishing Co., Inc.

Hartzell, S. (1978, 1). Earthquake aftershocks as Green's functions. *Geophysical Research Letters*, *5*(1), 1–4. doi: 10.1029/GL005i001p00001

Hartzell, S., & Heaton, T. (1986). Rupture history of the 1984 Morgan Hill, California, earthquake from the inversion of strong motion records. *Bulletin of the Seismological Society of America*.

Hartzell, S., Mendoza, C., & Zeng, Y. (2013). Rupture model of the 2011 Mineral, Virginia, earthquake from teleseismic and regional waveforms. *Geophysical Research Letters*, *40*(21), 5665–5670. doi: 10.1002/2013GL057880

Ide, S. (2001). Complex source processes and the interaction of moderate earthquakes during the earthquake swarm in the Hida-Mountains, Japan, 1998. *Tectonophysics*, *334*(1), 35–54. doi: 10.1016/S0040-1951(01)00027-0

Ide, S. (2002). Estimation of radiated energy of finite-source earthquake modeling. *Bull. Seismol. Soc. Am.*, *92*(8), 2994–3005.

Keranen, K. M., Weingarten, M., Abers, G. A., Bekins, B. A., & Ge, S. (2014, 7). Sharp increase in central Oklahoma seismicity since 2008 induced by massive wastewater injection. *Science*, *345*(6195), 448–451. doi: 10.1126/science.1255802

Lawson, C. L., & Hanson, R. J. (1987). *Solving Least Squares Problems (Classics* *in Applied Mathematics)*. doi: 10.1137/1.9781611971217

Lui, S. K. Y., & Huang, Y. (2019). Do Injection-Induced Earthquakes Rupture Away from Injection Wells due to Fluid Pressure Change? *Bulletin of the Seismological Society of America*, *109*(1), 358–371. doi: 10.1785/0120180233

Madariaga, R. (1976). Dynamics of an expanding circular fault. *Bull. Seismol. Soc. Am.*, *66*(3), 639–666.

Mai, P. M., & Thingbaijam, K. K. S. (2014). SRCMOD: An Online Database of Finite-Fault Rupture Models. *Seismological Research Letters*, *85*(6), 1348–1357. doi: 10.1785/0220140077

Moschetti, M. P., Hartzell, S. H., & Herrmann, R. B. (2019, 3). Rupture Model of the M5.8 Pawnee, Oklahoma, Earthquake From Regional and Teleseismic Waveforms. *Geophysical Research Letters*, *46*(5), 2494–2502. doi: 10.1029/2018GL081364

Norbeck, J. H., & Horne, R. N. (2016, 12). Evidence for a transient hydromechanical and frictional faulting response during the 2011 M w 5.6 Prague, Oklahoma earthquake sequence. *Journal of Geophysical Research: Solid Earth*, *121*(12), 8688–8705. doi: 10.1002/2016JB013148

Okada, Y., Yamamoto, E., & Ohkubo, T. (2000). Coswarm and preswarm crustal deformation in the eastern Izu Peninsula, Centeral Japan. *J. Geophys. Res.*, *105*(1), 681–692.

Pennington, C., & Chen, X. (2017, 7). Coulomb Stress Interactions during the M w 5.8 Pawnee Sequence. *Seismological Research Letters*, *88*(4), 1024–1031. doi: 10.1785/0220170011

Qin, Y., Chen, X., Carpenter, B. M., & Kolawole, F. (2018). Coulomb Stress Transfer Influences Fault Reactivation in Areas of Wastewater Injection. *Geophysical Research Letters*. doi: 10.1029/2018GL079713

Somerville, P., Irikura, K., Graves, R., Sawada, S., Wald, D., Abrahamson, N., . . . Kowada, A. (1999). Characterizing crustal earthquake slip models for the prediction of strong ground motion. *Seismological Research Letters*, *70*(1), 59–80. doi: 10.1785/gssrl.70.1.59

Sumy, D. F., Cochran, E. S., Keranen, K. M., Wei, M., & Abers, G. A. (2014, 3). Observations of static Coulomb stress triggering of the November 2011 M 5.7 Oklahoma earthquake sequence. *Journal of Geophysical Research: Solid Earth*, *119*(3), 1904–1923. doi: 10.1002/2013JB010612

Sun, L., Zhang, M., & Wen, L. (2016). A new method for high-resolution event relocation and application to the aftershocks of Lushan Earthquake, China. *J. Geophys. Res.*, *121*, 2539–2559. doi: 10.1002/2016JB012840

Sun, X., & Hartzell, S. (2014). Finite-fault slip model of the 2011 Mw 5.6 Prague, Oklahoma earthquake from regional waveforms. *Geophysical Research Letters*, *41*(12), 4207–4213. doi: 10.1002/2014GL060410

Uchide, T., & Ide, S. (2007). Development of multiscale slip inversion method and its application to the 2004 mid-Niigata Prefecture earthquake. *Journal of Geophysical Research: Solid Earth*, *112*(6), 1–20. doi: 10.1029/2006JB004528

Uchide, T., & Song, S. G. (2018). Fault Rupture Model of the 2016 Gyeongju, South Korea, Earthquake and Its Implication for the Underground Fault System. *Geophysical Research Letters*, *45*(5), 2257–2264. doi: 10.1002/2017GL076960

Wei, S., Avouac, J. P., Hudnut, K. W., Donnellan, A., Parker, J. W., Graves, R. W., … Eneva, M. (2015). The 2012 Brawley swarm triggered by injection-induced aseismic slip. *Earth and Planetary Science Letters*, *422*, 115–125. doi: 10.1016/j.epsl.2015.03.054

Wei, S., Helmberger, D., Owen, S., Graves, R. W., Hudnut, K. W., & Fielding, E. J. (2013). Complementary slip distributions of the largest earthquakes in the 2012 Brawley swarm, Imperial Valley, California. *Geophysical Research Letters*, *40*(5), 847–852. doi: 10.1002/grl.50259

Wu, Q., Chen, X., & Abercrombie, R. E. (2019). Source Complexity of the 2015 Mw 4.0 Guthrie, Oklahoma Earthquake. *Geophysical Research Letters*, *46*(9), 4674–4684. doi: 10.1029/2019GL082690

Yabuki, T., & Matsu'ura, M. (1992). Geodetic data inversion using a Bayesian information criterion for spatial distribution of fault slip. *Geophysical Journal International*. doi: 10.1111/j.1365-246X.1992.tb00102.x

Ye, L., Kanamori, H., & Lay, T. (2018). Global variations of large megathrust earthquake rupture characteristics. *Science Advances*, *4*(3), 1–8. doi: 10.1126/sciadv.aao4915

Yoshida, K., Saito, T., Emoto, K., Urata, Y., & Sato, D. (2019, 10). Rupture directivity, stress drop, and hypocenter migration of small earthquakes in the Yamagata-Fukushima border swarm triggered by upward pore-pressure migration after the 2011 Tohoku-Oki earthquake. *Tectonophysics*, *769*. doi: 10.1016/j.tecto.2019.228184

Event	Date	Mw	Stress Drop (MPa)	Number of Slip Patches
Guthrie	04/08/2015	4.1	1.58	5
Prague	11/06/2011	5.6	1.6	10
Hida Ev 5	08/12/1998	4.7	1.19	2
Hida Ev 7	08/14/1998	4.6	1.94	1
Hida Ev 8	08/16/1998	4.5	0.54	1
Hida Ev 9	08/16/1998	5.2	1.19	3
Hida Ev 10	08/17/1998	4.7	0.92	1
Hida Ev 11	08/22/1998	4.5	0.97	3
Hida Ev 16	09/18/1998	4.6	0.81	5
Brawley Swarm Ev 1*	09/26/2012	5.4	-	1
Brawley Swarm Ev 2*	09/26/2012	5.3	-	3

Table 3.1: Earthquakes compared against the Guthrie Mw 4.1 earthquaake and their respective slip patch number. *Stress drop values not available.

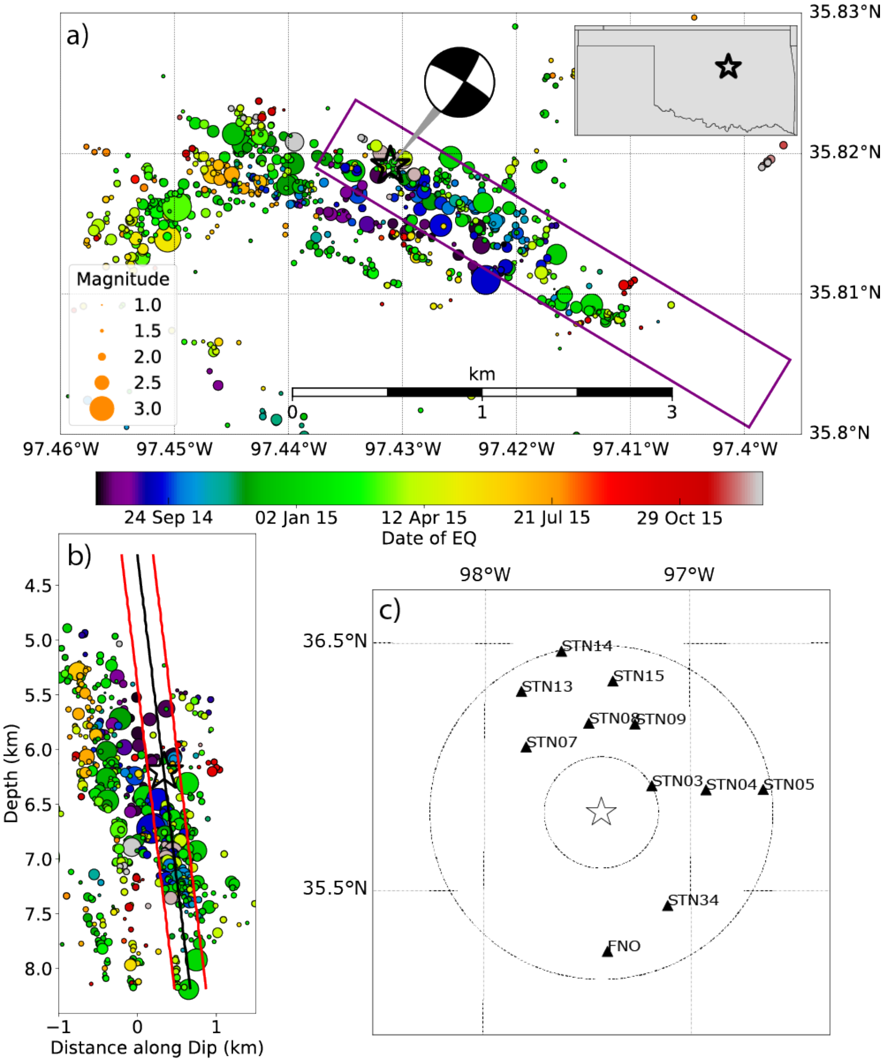

Figure 3.1: a) Map view of the Guthrie earthquake sequence with earthquakes colored by date and scaled by magnitude. The M_w 4.1 (black star) and model fault (purple box) are also shown. (b) Perpendicular cross section across modeled model fault. Model fault is shown as black line, red lines denote distance of 200 m from model fault. Earthquakes that fall within these red bars are plotted on modeled slip in Figure 3. (c) Map view of stations (black triangles) used in the inversion circles mark 25 km and 75 km distance interval from event epicenter location (black star)

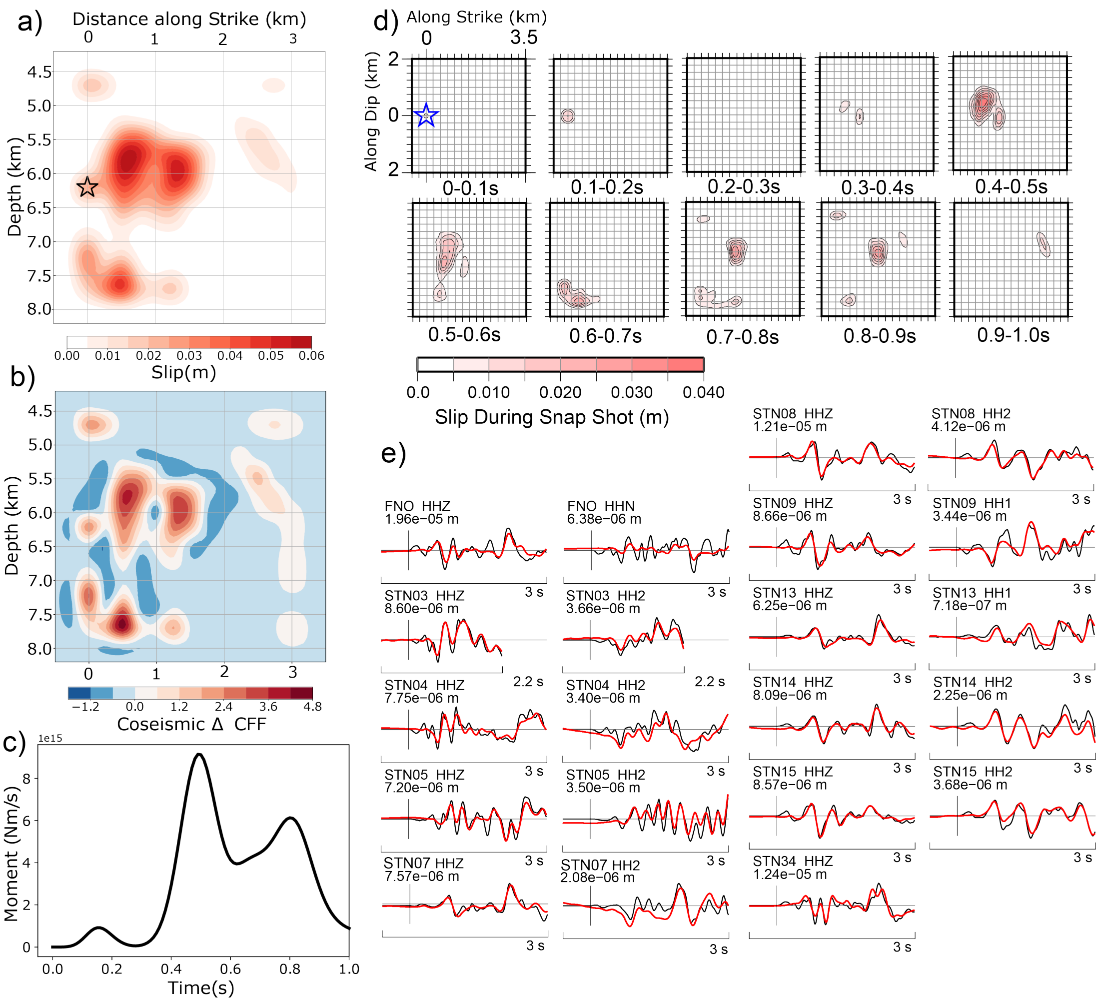

Figure 3.2: Slip inversion analysis results for the mainshock. (a) distribution of the final slip. (b) Distribution of the stress change. (c). Moment rate function. (d) Snapshots of the distribution of the slip rate as specified time intervals. (e) Comparison of between the observed (black) and synthetic waveforms (red).

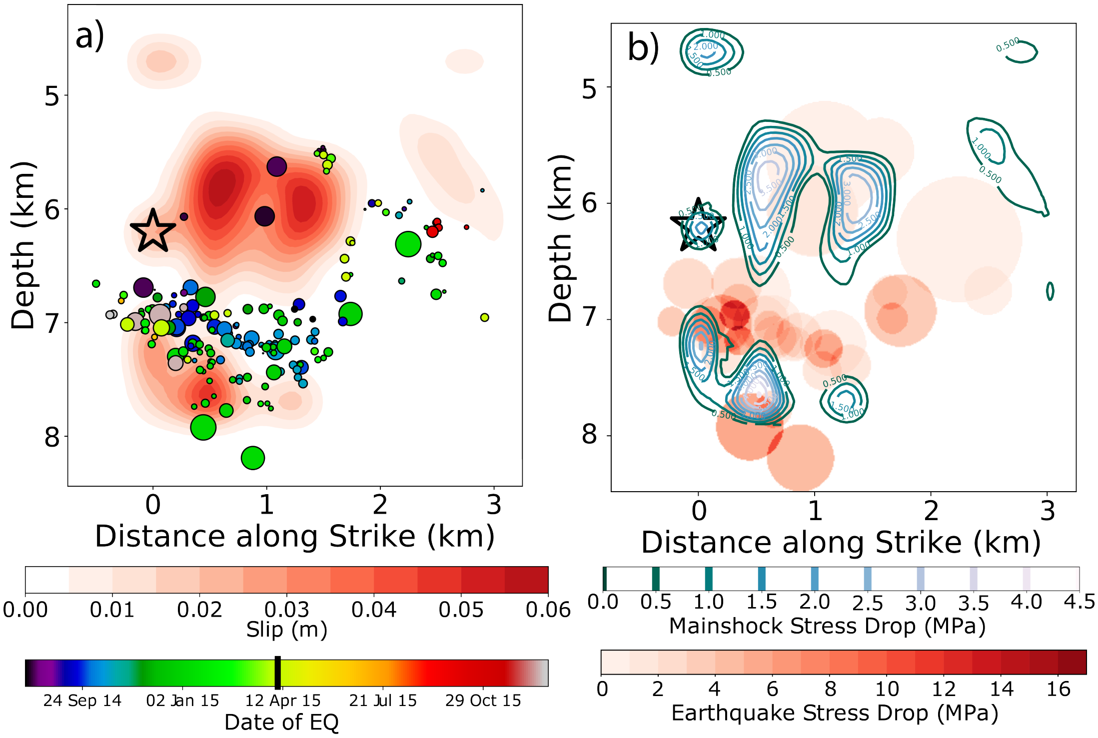

Figure 3.3: (a) Distribution of the final slip with mainshocks hypocenter (black star) and earthquakes within 200 m of modeled fault shown. Earthquakes are scaled by magnitude and colored by date.(b) Stress drop distribution of modeled earthquake (blue contours). Cumulative stress drop along the model fault caused by previous seismicity.

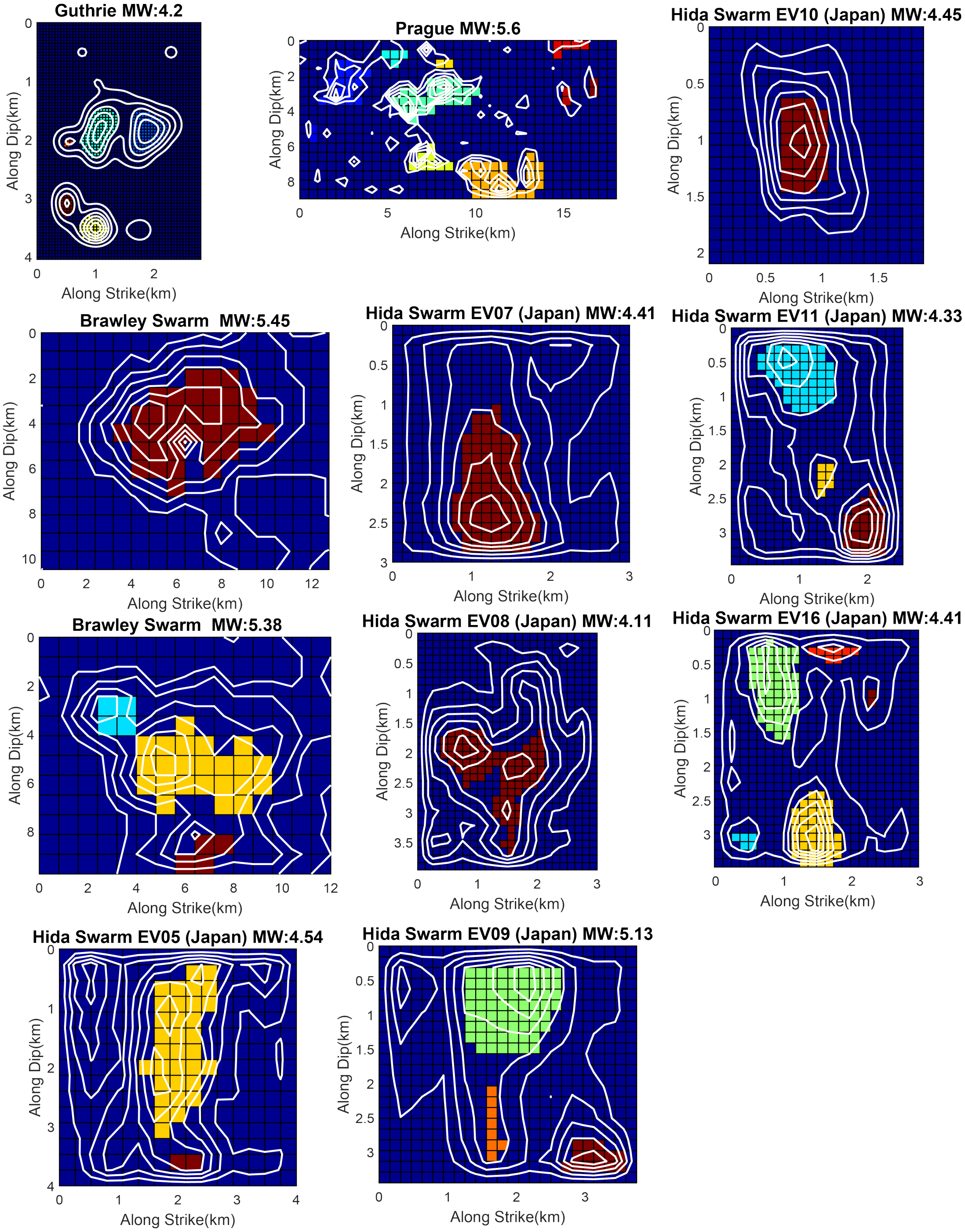

Figure 3.4: Slip distributions for each earthquake compared in the study and their identified individual slip patches. Slip contours have been normalized to maximum slip for each event and contours represent 15% increments. Slip patches are colored based upon group and non-grouped grids are blue.

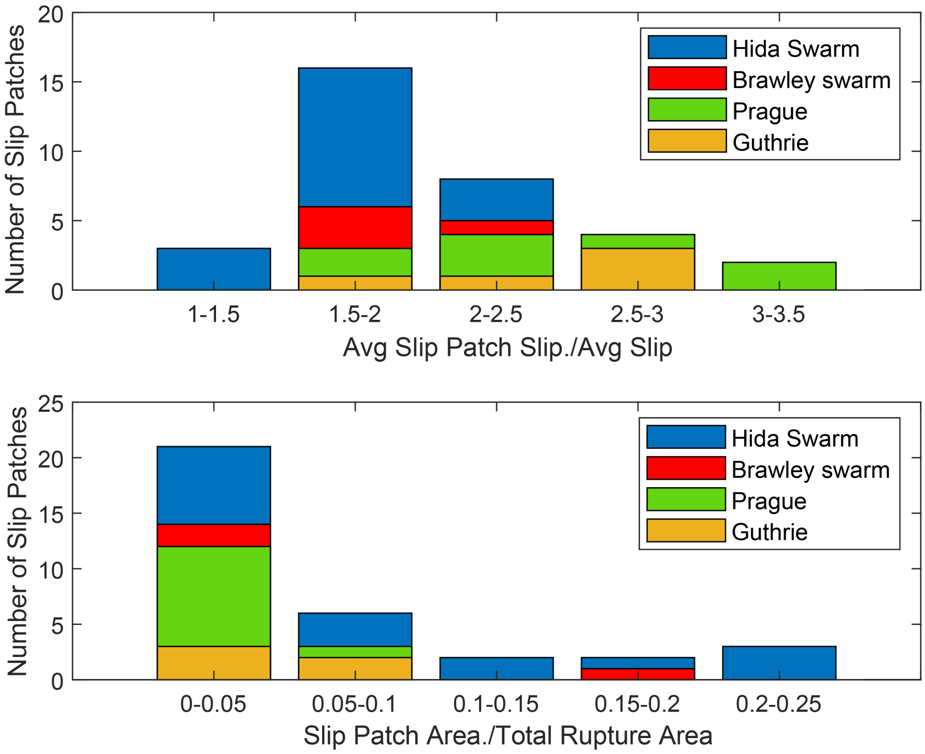

Figure 3.5: Histogram of the normalized slip (top) and normalized area (bottom) for the slip patches observed in each region. Note that Prague and Guthrie have higher concentrations of slip within slip patches (top) and they also have smaller slip patches (bottom).

Chapter 4

Control Factors of Earthquake Rupture Complexity from a Global Perspective

4.1 Abstract

Previous studies of earthquake rupture complexity have primarily been focused on large earthquakes (i.e., M≥7). However, with the improvement of network coverage and data processing, recent studies suggest that small to moderate earthquakes can be complex. In this study, we seek to further understand the regional and global patterns of earthquake rupture complexity using the SCARDEC source time function database,(Vallée & Douet, 2016), which would help to understand the control factors of earthquake rupture. We quantify the complexity of the source time function (STF) for each earthquake in the database by calculating a roughness parameter, which is defined as the ratio of the measured radiated energy from STF to the calculated minimum radiated energy for an STF with

the same seismic moment and duration. Earthquakes with relatively high (≥4) roughness estimates indicate more complex source processes that likely include multiple pulses or sub-events. We hereby refer to those events with high roughness estimates (≥4) as complex and those with low estimates (≤4) as simple. The 3395 events with roughness estimates show systematic regional variations, which suggests that rupture complexity may be strongly linked to regional geology. We also find that complexity varies with faulting type, and depth. We are able to correlate these observations to observed geologic or structural complexities for select regions. These observations indicate that the processes that control rupture complexity are not random, but instead vary regionally and these variations can be related to changes in coupling, stress heterogeneity, lithology, and other geologic phenomenon.

4.2 Introduction

Understanding what controls earthquake rupture processes for large magnitude earthquakes is vital to our estimation of earthquake hazard. The application of one single model to represent ruptures however has been elusive. This is due to the fact that rupture characteristics of larger earthquakes often vary significantly from one another. Assuming that the distributions of slip patches, where a majority of slip for these events occurs, represent asperities (e.g. locked segments of the fault) then earthquake rupture characteristics is controlled by asperity distribution and interactions (Lay & Kanamori, 1981; Lay et al., 1982). The final rupture size and magnitude of a large event is controlled by the size of the asperity and the number of asperities that fail simultaneously during a single event. These two factors can result in earthquakes having heterogeneous ruptures due to the failure of multiple asperities like what occurred during the Mw 9.2 2004 Sumatra earthquake (Yoshimoto & Yamanaka, 2014), or ruptures characterized by a single large asperity such as the Mw 9.1 2011 Tohoku, Japan (Lay et al., 2011; Miyazaki et al., 2012).

The factors that control large earthquake complexity are still debated, but certain fault regions exhibit consistent rupture behavior indicating that it is caused by a persistent phenomenon and is not random (Ye et al., 2018). The cause of this consistent behavior is not well known. Studies suggested asperities themselves are fixed geologic structures that rupture repeatedly (Igarashi et al., 2003; Yamanaka & Kikuchi, 2004), however these asperities' ruptures do not always rupture in the same way from one earthquake cycle to another (Thatcher, 1990; Tanioka et al., 1996; Schwartz, 1999; Hirose & Hirahara, 2002). This varying temporal behavior also appears in the triggering of multiple asperities that requires equivalent stresses on neighboring asperities and such a scenario might take multiple seismic cycles to reoccur (e.g., Ruff, 1996). If observations of self-similarity in earthquakes is correct, then theoretically the small earthquakes in the region should exhibit similar levels of complexity as large events (Allmann & Shearer, 2009; Prieto et al., 2004; Trugman et al., 2017). Previous studies that have examined smaller magnitudes have found that they are complex, but to a lesser degree, and therefore are an inappropriate analog for rupture complexity for larger events (Danré et al., 2019). No study has attempted to examine the spatial patterns of these smaller M>6.0 events, but instead focused the larger M>8.0 events.

We take advantage of existing Source Time Function (STF) catalogs (Vallée & Douet, 2016)to expand the analysis of Ye et al. (2018). Our findings are that event complexity varies with faulting regime, magnitude, depth and region.

Reverse faulting events exhibit a consistent level of rupture complexity across magnitudes for certain regions, while in others only the largest events are complex. For strike-slip events we find faults that consistently display complex or simple failure indicating that geology likely strongly controls complexity. These findings indicate that for certain regions the complexity levels of small events mimic those of large events, while in others either the temporal stress state or the spatial distributions of asperities causes rupture complexity to only manifest in larger events.

4.3 Data

For our analysis we utilize the SCARDEC (Seismic source ChActeristics Retrieved from DEConvoling teleseismic body waves,(Vallée & Douet, 2016)) source time functions (STF) database, which contains 3,395 STF's for earthquakes from M5.5 to M9.0 between 1992 and 2017. For each of these events we utilize the Global Centroid Moment Tensor (GCMT) catalogs hypocentral location in our analysis (Dziewonski & Anderson, 1981; Ekström et al., 2012). The SCARDEC catalog's STFs are created through deconvolving a synthetic theoretical Green's function computed using a radially symmetric and an elastic earth model from the observed teleseismic P waves. The synthetic EGF's are accurate down to 1 Hz, and therefore lower magnitude events complexity might not entirely be captured. The STFs of this catalog have been found to have comparable shapes to those of the United States Geological Survey (USGS) STF database (Hayes, 2017), events (Meier et al., 2017).

We utilize the average STF's from the catalog, which are created by stacking the apparent source time functions (ASTF) obtained from each station that have good agreement between the real and modeled waveforms. To stack the ASTF's for an event it's estimated good ASTFs are cut as they approach zero near the average duration obtained from all ASTF for an event. These cut ASTFs are then aligned through cross-correlation and the average STF in the SCARDEC catalog are obtained from this aligned stack.

The averaged STFs from the SCARDEC catalog often have large leading and trailing tails that have a significant impact on roughness estimates (Figure 4.1). The following criteria was used to cut the data to focus analysis on the peaks of the STF. To remove the leading tail, we cut the start of the STF where the slope is ≥ 0.01 and ≤ 0.3 based upon a sliding window. We also require that the amplitude at this point has to be $\leq 20\%$ of the max peak and $\geq 1\%$ of the overall moment. To remove the trailing tail of the STF we cut the STF at the trough that follows last peak that is $\geq 20\%$ of maximum peak of the STF. If there is no trough then we use the same criteria that was used to find starting location but require $\geq 98\%$ moment.

4.4 Method

We quantify the complexity of the Source Time Functions (STF) using a roughness parameter following the method described in Ye et al. (2018). Where the roughness of a STF is obtained by comparing it to a parabolic source with the same seismic moment and duration. The parabolic source duration is calculated using:

$$\dot{u} = 6M_0/T^3 \cdot t \cdot (T - t) \tag{4.1}$$

where $\dot{u}$ is the time-derivative of the parabolic moment-rate function, T is the duration of the STF, and t are the time samples. Examples of estimated parabolic rate functions are shown in Figure 4.1. The roughness(γ) of the STF is calculated using:

$$\gamma = \frac{\int_0^T \ddot{M}(t)^2 dt}{\int_0^T \dot{u}(t)^2 dt} = \frac{E_R^M}{E_M^{R_{min}}} \tag{4.2}$$

Here, $\ddot{M}$ is time derivative of the observed STF, E_R^M is the measured STF radiated energy and $E_M^{R_{min}}$ is the calculated minimum radiated energy for a parabolic moment-rate function. It should be noted that γ is not the same as the REEF value used by Ye et al. (2018). REEF includes high frequency energy, while γ is based on the STF's which are obtained using only low frequency data.

4.5 Results and Interpretation

We obtain roughness estimates for 3395 earthquakes with magnitude ranges from M5.5-9. Based upon the visual inspection of the results a roughness estimate $\geq$4 indicates a more complex source process that could include multiple energy release pulses (aka sub-events) (Figure 4.1) We hereby refer to those events with roughness estimates $\geq$4 as complex and those with low estimates as simple. The spatial patterns of smoothed roughness values are shown in Figure 4.2. The overall spatial patterns of rupture complexity for broad subduction zones remains fairly uniform with simple events being the majority in most regions. Regions that contain transform faults often exhibit higher levels of complexity.

When examining the roughness parameters statistical trends, we find 3 major findings.

- The percentage of events that are considered complex increases with magnitude (Figure 4.3 a). This observation supports similar findings by Danré et al. (2019) that found that SCARDEC STF's of magnitudes $\geq$M7 exhibit more subevents than smaller magnitudes. It should be noted that the high percentage of low roughness estimates for earthquakes below 6.5M are likely due to the deconvolution method only being able to capture subevents with a pulse width of 1s. Due to this resolution limit it is possible that these lower magnitude events are also complex, but such complexity is not resolvable.

- The percentage of complex events depends on faulting type. Strike-slip events have a higher percentage of complex events (Figure 4.3 c). This is likely caused by strike-slip faults having more complex fault geometry such as bends and steps that occur over smaller spatial scales compared to suduction zones, and often contain multiple faults which can lead to significant complexity in a earthquakes rupture such as the 2016 Mw 7.8 Kaikōura earthquake (Hamling et al., 2017). The likelyhood of strike slip faults interacting with complex fault geometry also higher due to them having higher aspect ratios compared to subduction earthquakes, which means they often propagate over longer lengths, and therefore are more likely to reach a bend or step (Weng & Yang, 2017). It should be noted that offshore strike slip events might have complexity estimates that are over estimated due to contamination of direct seismic phases by water multiples (Yue et al., 2017).
- The distribution of complex events depends on event depth (Figure 4.3 b). The shallowest earthquakes ($\leq$35 km) are found to be the most complex, with deeper events often being simpler. The high roughness estimates for shallow events can partially be attributed to the abundance of strike

strike-slip events in this depth range as well as water multiples being included in the STF for oceannic earthquakes. Previous studies of the same STF catalog have found that the number of sub-events does not change significantly with depth (Danré et al., 2019), which might indicate that the depth-dependence in roughness level could be attributed to a change in the characteristics of the sub-event gaussian pulses (e.g., delay time, width). Past attempts at characterizing STF complexity with depth disagree as to whether there is a depth dependence, with some finding a decrease in complexity (Houston, 2001), while others found an increase (Persh & Houston, 2004). Due to the number of STFs we examine, our results should be more statistically robust than previous studies.

4.5.1 Subduction Zone Reverse Faulting Earthquakes

Figures 4.4 shows multiple regions and the non-smoothed complexity measures of reverse faulting earthquakes (aka thrust earthquakes) that occur near the slab interface (Hayes et al., 2018). Comparing our results for these regions to those of (Ye et al., 2018), we find generally consistent patterns, but also more diversity. Based upon our observations we find 3 types of patterns. The first type exhibits alternating patterns of complex and simple earthquakes. Examples of this patterns are the Japan and Kuril subduction zone and South America region (Figure 4.4 a-b). The second type contains ruptures that are primarily one type of rupture. An example of this is the predominantly simple ruptures in Central America region, which is bookended by two large complex ruptures (Figure 4.4 c). The last style exhibits a single predominant style like type two, but intermittently a large complex rupture will occur. An example of this is the

Aleutian Islands shown in Figure 4.4 d.

Many properties of the subduction zone could influence the observed patterns for complex reverse faulting earthquakes. Past studies have made correlations between maximum earthquake size and subducted sediment thickness (Heuret et al., 2012; Scholl et al., 2015), seamount or seafloor roughness (Bassett & Watts, 2015), seismic coupling (Scholz & Campos, 2012), gravity anomaly (Ammon et al., 2008), and slab dip angle (Bletery et al., 2016). Ye et al. (2018) found that spatial heterogeneity in the observed interseismic coupling is often correlated with complex rupture (high REEF), and more uniform coupling correlated correlated to simple ruptures (low REEF). Our findings support this interpretation. We also find that sea floor roughness generally correlates with our results (Lallemand et al., 2018). Where simple STF's occur in regions with smooth sea floor while complex events occur in regions with moderately rough to rough seafloor.

4.5.2 Normal Faulting Earthquakes

Normal faulting type earthquakes in the SCARDEC catalog occur predominantly in two types of regions: (1) within a subducting slab; (2) within the fore-arc or back-arc basins around subducting plates. In order to remove the effects of water multiples we examine 345 deep events (> 35 km), since deep events have been observed to have clean P phase arrivals (Fan & Shearer, 2018; Tibi et al., 2003). When examining these events, we find that normal faulting events increase in complexity with depth (Figure 4.5). This is the opposite pattern observed from the finding for all events (Figure 4.3 b). The reason for this opposite finding is due to normal faulting events representing a small portion of the total events in the SCARDEC catalog, so their pattern was hidden by those of reverse and strike-slip events. Our observations in general align with the observations of increasing STF complexity observed by Houston et al. (1998); Persh and Houston (2004) and we also observe the decrease in complexity after 550 km of depth found by Persh and Houston (2004).

There are many explanations for the mechanisms that produce the deep normal earthquake rupture complexity that we are observing, however they are in general based on observations from all deep earthquakes. For the events between 35-350 km depth two possible explanations are the reactivation of faults (Jiao et al., 2000) and dehydration embrittlement (Raleigh & Paterson, 1965; Silver et al., 1995), however both mechanisms are found to have less impact below 300-400 km (Green & Houston, 1995; Kirby et al., 1996). For events in the depth range of 350-550 km past modeling has shown the possibility of a wedge of metastable olivine often occurs in this region (Devaux et al., 1997). Faulting initiated by this type of transformational faulting might also explain the increase of fault zone heterogeneity and rupture complexity (Frohlich, 1987). The events past this depth range (>550 km) are more difficult to explain. (Persh & Houston, 2004) explained the rupture of these events as possibly caused by transformational faulting of enstatite to ilmenite (Hogrefe et al., 1994). However other alternatives could be that at such depths shear instability is becoming the driver(Ogawa, 1987; Hobbs & Ord, 1988; Fan et al., 2019). This could be due to the increase of heat, high strain rates and large amounts of latent heat release that could promote thermal runaway at these depths (Wiens, 2001; Tibi et al., 2003; Karato et al., 2001).

4.5.3 Strike-Slip Earthquakes

To examine the spatial patterns of strike slip earthquakes, we examine the earthquakes that occur along in the Gulf of California fault systems. This region is chosen because of its abundance of strike slip events and the lack of water multiples being found during previous moment tensor and finite fault analysis of events in the region (e.g., Doser, 1992; Ortega et al., 2014; Rodríguez-Lozoya et al., 2008)). When examining earthquakes that occur on separate fault groups, we can see that certain fault segments exhibit a consistent STF roughness level (Figure 4.6). Examples of a segment of simple events are events 4 and 5 that occur on Ballenas Transform Fault. Examples of complex events are 6 and 7, which occur on a transform fault between the Carmen and Farallon spreading centers, and event 8 that occurs along a transform fault that links the Farallon and Pescadero spreading centers. The uniformity of complexity level observed in across different fault segments indicates that that a larger regional change has occurred that might be effecting fault properties.

Possible large scale regional changes that occur between the intracontental faults in the north and the oceanic transform Ballenas Fault can most directly be related lithological, and rheological properities of the rocks they propagate through. This change in rock properties is reflected in each faults relative slip rate with Ballenas Transform Fault having a slip rate of 47.3 ± 0.8 mm/yr, which accommodates almost all of the Baja California-North America plate relative motion far exceeding the rate of individual intracontinental strike-slip faults of the San Andreas (Plattner et al., 2015). This difference in accommodation of slip indicates changes in frictional properties or fault structure that allows for slip to be accommodated predominately aseismically. The cause of the differences between the Ballenas Transform Fault and the southern region likely has to do with the orientation of strain, the Ballenas Transform Fault (EV 4 and 5) is experiencing only northwest-directed transtensional deformation, while the southern region (EV 6-8) is experiencing both northwestern and NE to ENE extension (Fletcher & Munguia, 2000; Dorsey & Umhoefer, 2012; Umhoefer et al., 2020). The northern region is also found to have a higher heat flow, when compared to the southern region (Di Luccio et al., 2014). This higher heat flow could mean the transition from brittle to ductile deformation is shallower, which could lead to more aseismic creep in this region. These factors as well as the different ages of these fault segments likely attributes somewhat to the different levels of complexity their ruptures exhibit.

4.6 Conclusions

The estimation of complexity of the SCARDEC catalogs STFs and its analysis has allowed us to make the following major observations:

- Earthquake ruptures change based upon earthquake faulting type, magnitude, and depth.
- Rupture complexity of reverse earthquakes appears to be dominantly controlled by regional factors that remain constant through the observed time period.
- Normal faulting earthquakes increase in complexity with depth. The drivers of this complexity for the depth range of 35-550km are likely dehydration embrittlement, the reactivation of preserved faults and/or transformational faulting of metastable olivine. The deepest event drivers are less well known

and could be a different transformational faulting or thermally driven shear instabilities.

- Strike-slip earthquakes show consistent ruptures, which change over small spatial distances compared to thrust and normal faulting. These ruptures' complexities are controlled by lithology, age, heat flow, and heterogeneity of the stress field.

The above observations indicate that the processes that control rupture complexity are not random, but instead are due to persistent fault properties that vary with faulting regime and regional geology.

4.7 Acknowledgments

The SCARDEC database is open to the public `http://scardec.projects.sismo.ipgp.fr/` and free to use. Figures in this paper were made with GeoMapApp (`www.geomapapp.org`) and GRMT data by Ryan et al. (2009). Earthquake information plotted on figures is from International Seismological Centre (2020), On-line Bulletin, `https://doi.org/10.31905/D808B830`.

References

Allmann, B. P., & Shearer, P. M. (2009, 1). Global variations of stress drop for moderate to large earthquakes. *Journal of Geophysical Research*, *114*(B1), B01310. Retrieved from `http://doi.wiley.com/10.1029/2008JB005821` doi: 10.1029/2008JB005821

Ammon, C. J., Kanamori, H., & Lay, T. (2008). A great earthquake doublet and seismic stress transfer cycle in the central Kuril islands. *Nature*. doi: 10.1038/nature06521

Bassett, D., & Watts, A. B. (2015). Gravity anomalies, crustal structure, and seismicity at subduction zones: 1. Seafloor roughness and subducting relief. *Geochemistry, Geophysics, Geosystems*. doi: 10.1002/2014GC005684

Bird, P. (2003). An updated digital model of plate boundaries. *Geochemistry, Geophysics, Geosystems*. doi: 10.1029/2001GC000252

Bletery, Q., Thomas, A. M., Rempel, A. W., Karlstrom, L., Sladen, A., & De Barros, L. (2016). Mega-earthquakes rupture flat megathrusts. *Science*. doi: 10.1126/science.aag0482

Danré, P., Yin, J., Lipovsky, B. P., & Denolle, M. A. (2019). Earthquakes Within Earthquakes: Patterns in Rupture Complexity. *Geophysical Research Letters*, *46*(13), 7352–7360. doi: 10.1029/2019GL083093

Devaux, J. P., Schubert, G., & Anderson, C. (1997). Formation of a metastable olivine wedge in a descending slab. *Journal of Geophysical Research: Solid Earth*. doi: 10.1029/97jb02334

Di Luccio, F., Persaud, P., & Clayton, R. W. (2014). Seismic structure beneath the Gulf of California: A contribution from group velocity measurements. *Geophysical Journal International*. doi: 10.1093/gji/ggu338

Dorsey, R. J., & Umhoefer, P. J. (2012). Influence of Sediment Input and Plate-Motion Obliquity on Basin Development Along an Active Oblique-Divergent Plate Boundary: Gulf of California and Salton Trough. In *Tectonics of sedimentary basins: Recent advances.* doi: 10.1002/9781444347166.ch10

Doser, D. I. (1992). Faulting processes of the 1956 San Miguel, Baja California, earthquake sequence. *Pure and Applied Geophysics PAGEOPH*. doi: 10.1007/BF00876824

Dziewonski, A. M., & Anderson, D. L. (1981). Preliminary reference Earth model. *Physics of the Earth and Planetary Interiors*, *25*(4), 297–356. doi: 10.1016/0031-9201(81)90046-7

Ekström, G., Nettles, M., & Dziewoński, A. M. (2012). The global CMT project 2004-2010: Centroid-moment tensors for 13,017 earthquakes. *Physics of the Earth and Planetary Interiors*. doi: 10.1016/j.pepi.2012.04.002

Fan, W., & Shearer, P. M. (2018). Coherent Seismic Arrivals in the P Wave Coda of the 2012 Mw 7.2 Sumatra Earthquake: Water Reverberations or an Early Aftershock? *Journal of Geophysical Research: Solid Earth*. doi: 10.1002/2018JB015573

Fan, W., Wei, S. S., Tian, D., McGuire, J. J., & Wiens, D. A. (2019, 3). Complex and Diverse Rupture Processes of the 2018 M w 8.2 and M w 7.9 Tonga-Fiji Deep Earthquakes. *Geophysical Research Letters*, *46*(5), 2434–2448. doi: 10.1029/2018GL080997

Fletcher, J. M., & Munguia, L. (2000). Active continental rifting in southern Baja California Mexico: Implications for plate motion partitioning and the transition to seafloor spreading in the Gulf of California. *Tectonics*. doi: 10.1029/1999TC001131

Frohlich, C. (1987). Aftershocks and temporal clustering of deep earthquakes. *Journal of Geophysical Research: Solid Earth*. doi: 10.1029/jb092ib13p13944

Green, H. W., & Houston, H. (1995, 5). The Mechanics of Deep Earthquakes. *Annual Review of Earth and Planetary Sciences*, *23*(1), 169–213. Retrieved from `http://www.annualreviews.org/doi/10.1146/annurev.ea.23.050195.001125` doi: 10.1146/annurev.ea.23.050195.001125

Hamling, I. J., Hreinsdóttir, S., Clark, K., Elliott, J., Liang, C., Fielding, E., ... Stirling, M. (2017). Complex multifault rupture during the 2016 Mw 7.8 Kaikōura earthquake, New Zealand. *Science*. doi: 10.1126/science.aam7194

Hayes, G. P. (2017). The finite, kinematic rupture properties of great-sized earthquakes since 1990. *Earth and Planetary Science Letters*. doi: 10.1016/j.epsl.2017.04.003

Hayes, G. P., Moore, G. L., Portner, D. E., Hearne, M., Flamme, H., Furtney, M., & Smoczyk, G. M. (2018). Slab2, a comprehensive subduction zone geometry model. *Science*. doi: 10.1126/science.aat4723

Heuret, A., Conrad, C. P., Funiciello, F., Lallemand, S., & Sandri, L. (2012). Relation between subduction megathrust earthquakes, trench sediment thickness and upper plate strain. *Geophysical Research Letters*. doi: 10.1029/2011GL050712

Hirose, H., & Hirahara, K. (2002). A model for complex slip behavior on a large asperity at subduction zones. *Geophysical Research Letters*. doi: 10.1029/2002gl015825

Hobbs, B. E., & Ord, A. (1988). Plastic instabilities: implications for the origin of intermediate and deep focus earthquakes. *Journal of Geophysical Research*. doi: 10.1029/jb093ib09p10521

Hogrefe, A., Rubie, D. C., Sharp, T. G., & Seifert, F. (1994). Metastability of enstatite in deep subducting lithosphere. *Nature*. doi: 10.1038/372351a0

Houston, H. (2001). Influence of depth, focal mechanism, and tectonic setting on the shape and duration of earthquake source time functions. *Journal of Geophysical Research: Solid Earth*. doi: 10.1029/2000jb900468

Houston, H., Benz, H. M., & Vidale, J. E. (1998). Time functions of deep earthquakes from broadband and short-period stacks. *Journal of Geophysical Research: Solid Earth*. doi: 10.1029/98jb02135

Igarashi, T., Matsuzawa, T., & Hasegawa, A. (2003). Repeating earthquakes and interplate aseismic slip in the northeastern Japan subduction zone. *Journal of Geophysical Research: Solid Earth*. doi: 10.1029/2002jb001920

Jiao, W., Silver, P. G., Fei, Y., & Prewitt, C. T. (2000). Do intermediate- and deep-focus earthquakes occur on preexisting weak zones? An examination of the Tonga subduction zone. *Journal of Geophysical Research: Solid Earth*. doi: 10.1029/2000jb900314

Karato, S., Riedel, M. R., & Yuen, D. A. (2001). Rheological structure and deformation of subducted slabs in the mantle transition zone: Implications for mantle circulation and deep earthquakes. *Physics of the Earth and Planetary Interiors*. doi: 10.1016/S0031-9201(01)00223-0

Kirby, S. H., Stein, S., Okal, E. A., & Rubie, D. C. (1996). Metastable mantle phase transformations and deep earthquakes in subducting oceanic lithosphere. *Reviews of Geophysics*. doi: 10.1029/96RG01050

Lallemand, S., Peyret, M., van Rijsingen, E., Arcay, D., & Heuret, A. (2018). Roughness Characteristics of Oceanic Seafloor Prior to Subduction in Relation to the Seismogenic Potential of Subduction Zones. *Geochemistry, Geophysics, Geosystems*, *19*(7), 2121–2146. doi: 10.1029/2018GC007434

Lay, T., Ammon, C. J., Kanamori, H., Xue, L., & Kim, M. J. (2011, 7). Possible large near-trench slip during the 2011 M w 9.0 off the Pacific coast of Tohoku Earthquake. *Earth, Planets and Space*, *63*(7), 687–692. Retrieved from `http://link.springer.com/10.5047/eps.2011.05.033` doi: 10.5047/eps.2011.05.033

Lay, T., & Kanamori, H. (1981). An asperity model of large earthquake sequences. *Earthquake prediction: an international review*.

Lay, T., Kanamori, H., & Ruff, L. (1982). The asperity model and the nature of large subduction zone earthquakes. *Earthquake Prediction Research*.

Meier, M. A., Ampuero, J. P., & Heaton, T. H. (2017). The hidden simplicity of subduction megathrust earthquakes. *Science*. doi: 10.1126/science.aan5643

Miyazaki, S., McGuire, J. J., & Segall, P. (2012). Seismic and aseismic fault slip before and during the 2011 off the Pacific coast of Tohoku Earthquake.

Earth Planets and Space, *63*(7), 637–642. doi: 10.5047/eps.2011.07.001

Ogawa, M. (1987). Shear instability in a viscoelastic material as the cause of deep focus earthquakes. *Journal of Geophysical Research: Solid Earth*. doi: 10.1029/jb092ib13p13801

Ortega, R., Quintanar, L., & Rivera, L. (2014). Full Moment Tensor Variations and Isotropic Characteristics of Earthquakes in the Gulf of California Transform Fault System. *Pure and Applied Geophysics*, *171*(10), 2805–2817. doi: 10.1007/s00024-013-0758-7

Persh, S. E., & Houston, H. (2004). Deep earthquake rupture histories determined by global stacking of broadband P waveforms. *Journal of Geophysical Research: Solid Earth*. doi: 10.1029/2003JB002762

Plattner, C., Malservisi, R., Amelung, F., Dixon, T. H., Hackl, M., Verdecchia, A., ... Gonzalez-Garcia, J. (2015). Space geodetic observation of the deformation cycle across the Ballenas Transform, Gulf of California. *Journal of Geophysical Research: Solid Earth*. doi: 10.1002/2015JB011959

Prieto, G., Shearer, P., Vernon, F., & Kilb, D. (2004). Earthquake source scaling and self-similarity estimation from stacking P and S spectra. *J. Geophys. Res.*, *109*(8), 1–13. Retrieved from `http://dx.doi.org/10.1029/2004JB003084` doi: 10.1029/2004jb003084

Raleigh, C. B., & Paterson, M. S. (1965). Experimental deformation of serpentinite and its tectonic implications. *Journal of Geophysical Research*. doi: 10.1029/jz070i016p03965

Rodríguez-Lozoya, H. E., Quintanar, L., Ortega, R., Rebollar, C. J., & Yagi, Y. (2008). Rupture process of four medium-sized earthquakes that occurred in the Gulf of California. *Journal of Geophysical Research: Solid Earth*. doi: 10.1029/2007JB005323

Ruff, L. J. (1996). Large earthquakes in subduction zones: Segment interaction and recurrence times. In *Geophysical monograph series*. doi: 10.1029/GM096p0091

Ryan, W. B., Carbotte, S. M., Coplan, J. O., O'Hara, S., Melkonian, A., Arko, R., ... Zemsky, R. (2009). Global multi-resolution topography synthesis. *Geochemistry, Geophysics, Geosystems*. doi: 10.1029/2008GC002332

Scholl, D. W., Kirby, S. H., von Huene, R., Ryan, H., Wells, R. E., & Geist, E. L. (2015). Great (Mw8.0) megathrust earthquakes and the subduction of excess sediment and bathymetrically smooth seafl oor. *Geosphere*. doi: 10.1130/GES01079.1

Scholz, C. H., & Campos, J. (2012). The seismic coupling of subduction zones revisited. *Journal of Geophysical Research: Solid Earth*. doi: 10.1029/2011JB009003

Schwartz, S. Y. (1999). Noncharacteristic behavior and complex recurrence of large subduction zone earthquakes. *Journal of Geophysical Research: Solid Earth*. doi: 10.1029/1999jb900226

Silver, P. G., Beck, S. L., Wallace, T. C., Meade, C., Myers, S. C., James, D. E., & Kuehnel, R. (1995). Rupture characteristics of the deep Bolivian earthquake of 9 June 1994 and the mechanism of deep-focus earthquakes. *Science*. doi: 10.1126/science.268.5207.69

Tanioka, Y., Ruff, L., & Satake, K. (1996). The Sanriku-oki, Japan, earthquake of December 28, 1994 (Mw 7.7): Rupture of a different asperity from a previous earthquake. *Geophysical Research Letters*. doi: 10.1029/96GL01132

Thatcher, W. (1990). Order and diversity in the modes of circum-Pacific earthquake recurrence. *Journal of Geophysical Research*. doi: 10.1029/JB095iB03p02609

Tibi, R., Bock, G., & Wiens, D. A. (2003). Source characteristics of large deep earthquakes: Constraint on the faulting mechanism at great depths. *Journal of Geophysical Research: Solid Earth*. doi: 10.1029/2002jb001948

Trugman, D. T., Dougherty, S. L., Cochran, E. S., & Shearer, P. M. (2017). Source Spectral Properties of Small to Moderate Earthquakes in Southern Kansas. *Journal of Geophysical Research: Solid Earth*, *122*(10), 8021–8034. doi: 10.1002/2017JB014649

Umhoefer, P. J., Plattner, C., & Malservisi, R. (2020). Quantifying rates of "rifting while drifting" in the southern Gulf of California: The role of the southern Baja California microplate and its eastern boundary zone. *Lithosphere*. doi: 10.1130/L1132.1

Vallée, M., & Douet, V. (2016). A new database of source time functions (STFs) extracted from the SCARDEC method. *Physics of the Earth and Planetary Interiors*, *257*, 149–157. doi: 10.1016/j.pepi.2016.05.012

Weng, H., & Yang, H. (2017, 3). Seismogenic width controls aspect ratios of earthquake ruptures. *Geophysical Research Letters*, *44*(6), 2725–2732. doi: 10.1002/2016GL072168

Wiens, D. A. (2001). Seismological constraints on the mechanism of deep earthquakes: Temperature dependence of deep earthquake source properties. *Physics of the Earth and Planetary Interiors*. doi: 10.1016/S0031-9201(01)00225-4

Yamanaka, Y., & Kikuchi, M. (2004). Asperity map along the subduction zone in northeastern Japan inferred from regional seismic data. *Journal of Geophysical Research: Solid Earth*. doi: 10.1029/2003JB002683

Ye, L., Kanamori, H., & Lay, T. (2018). Global variations of large megathrust earthquake rupture characteristics. *Science Advances*, *4*(3), 1–8. doi: 10.1126/sciadv.aao4915

Yoshimoto, M., & Yamanaka, Y. (2014). Teleseismic inversion of the 2004 Sumatra-Andaman earthquake rupture process using complete Green's functions. *International Aquatic Research*, *66*(1), 1–8. doi: 10.1186/s40623-014-0152-4

Yue, H., Castellanos, J. C., Yu, C., Meng, L., & Zhan, Z. (2017). Localized water reverberation phases and its impact on backprojection images. *Geophysical Research Letters*. doi: 10.1002/2017GL073254

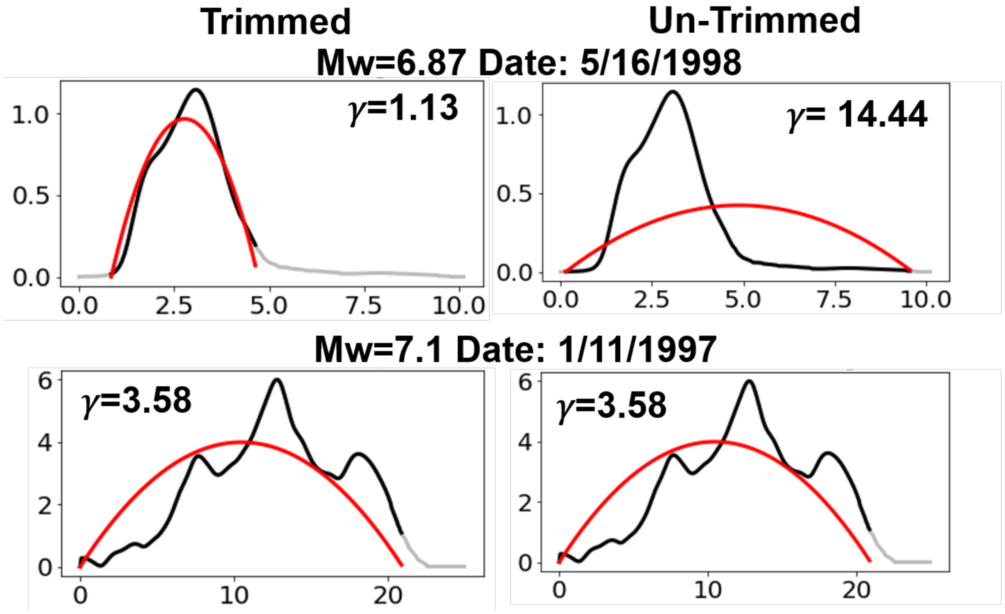

Figure 4.1: Examples of trimmed and untrimmed STFs. Portion cut during trimming are gray, while portion used in the analysis is shown in black and parabolic source time function is red. As you can see for some events (top) trimming will change the roughness significantly.

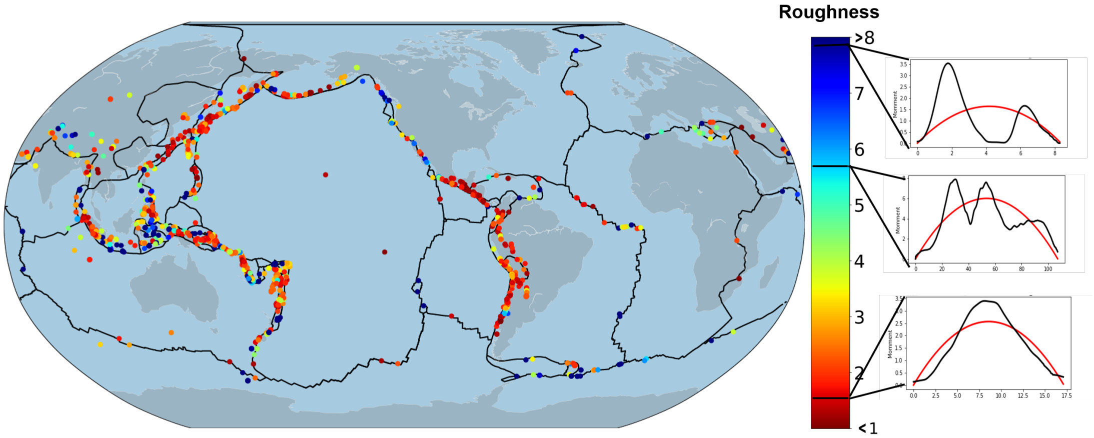

Figure 4.2: Plot of weighted average roughness values for the SCARDEC catalog earthquakes with a magnitude of >6.5. The averaged value is obtained using the weighted average of the log of roughness of the 10 closest events with the values being weighted by their distance from the event. Events within 25 km are weighted 1 while those further away are given the weight of their distance divided by 25. Example source time functions and the color associated with them are provided next to the color bar. Plate boundaries are denoted by black lines (Bird, 2003).

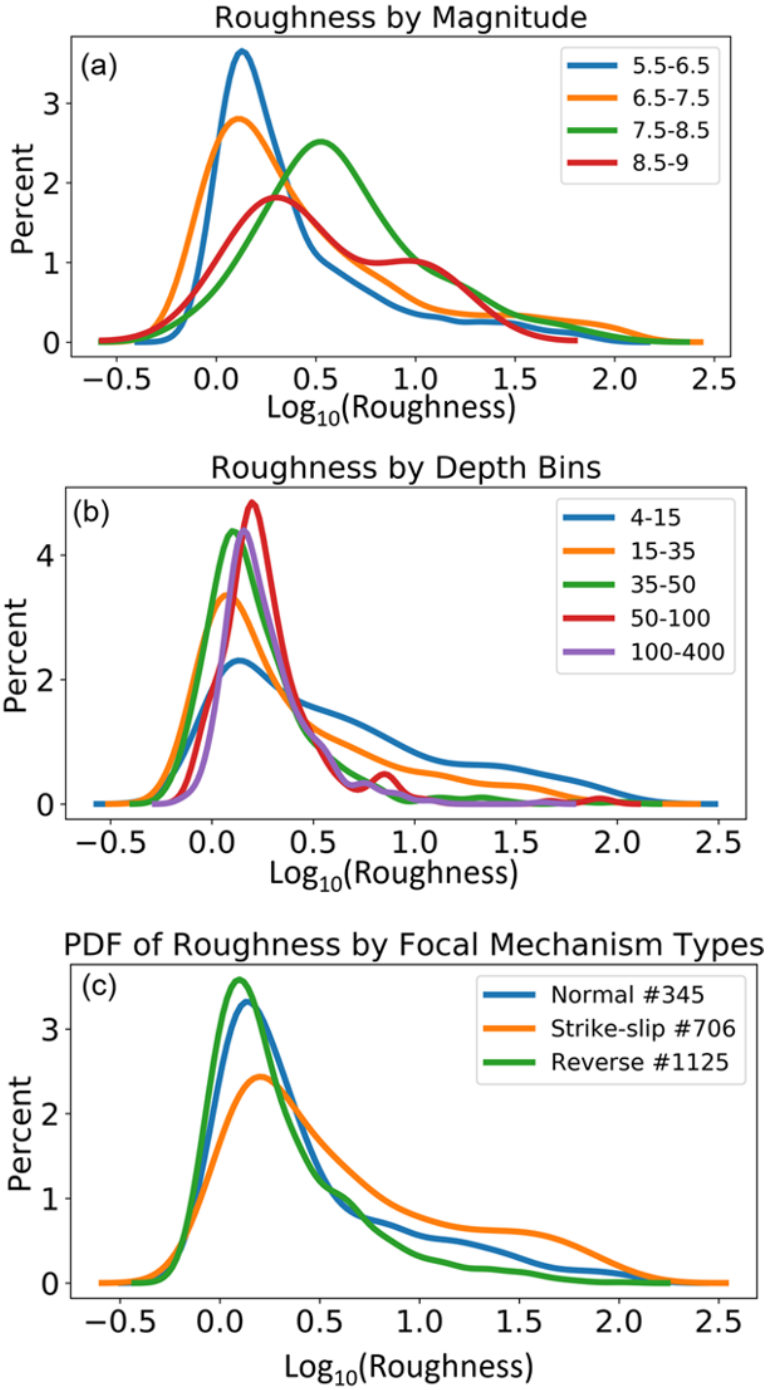

Figure 4.3: Percent of total population based upon probability density functions determined using kernel density estimate. Plots of the roughness vs magnitude(a), depth(b), focal mechanism type(c). This statistical analysis is from the non-weighted average trimmed source time function roughness estimates.

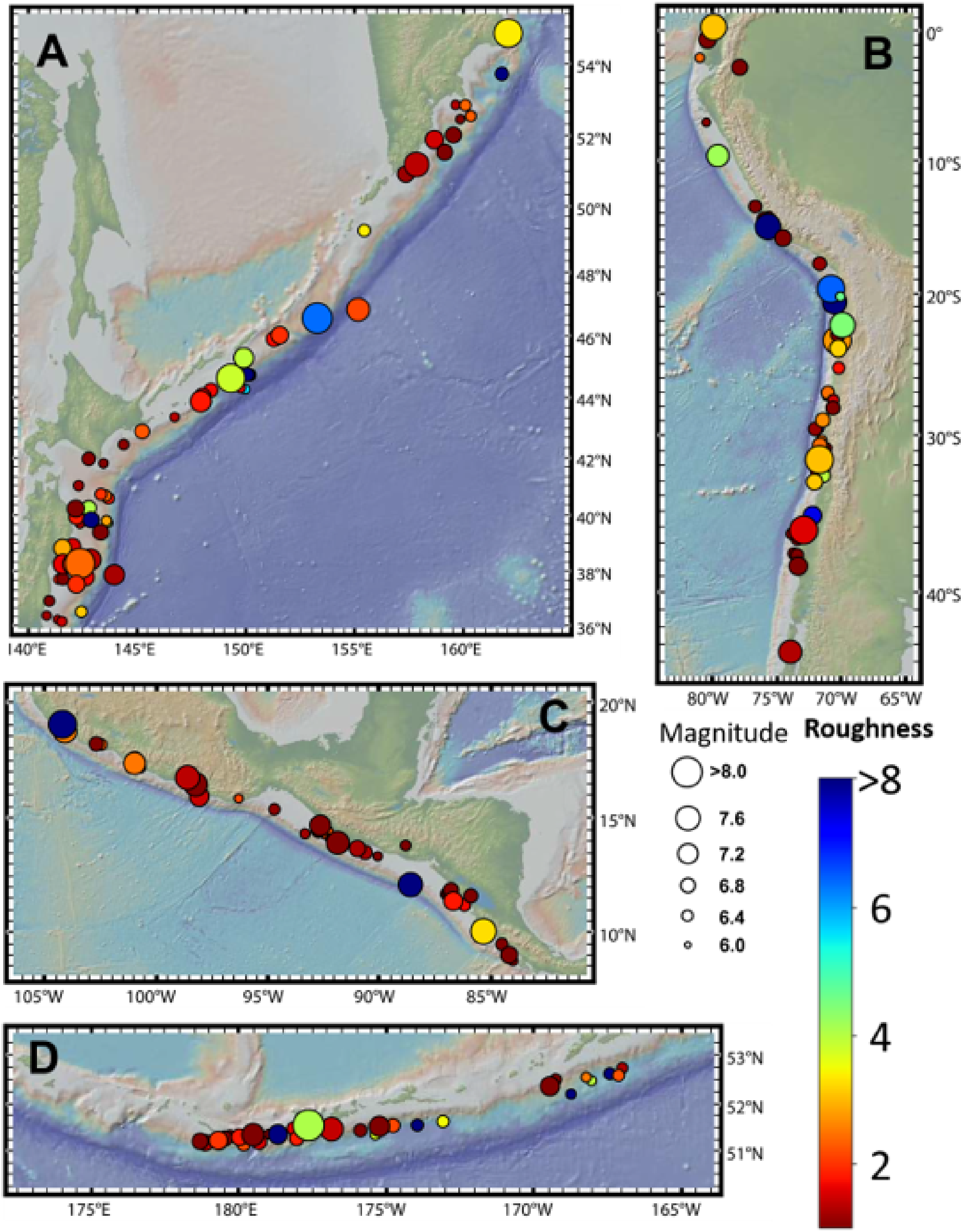

Figure 4.4: Map views of roughness estimates for different regions of the world for reverse style earthquakes that are within 20 km of the slab interface (± unc of slab). Non-weighted average roughness estimates are shown. A) Japan and Kuril Islands, B) South America, C) Central America, and D Aleutian Islands.

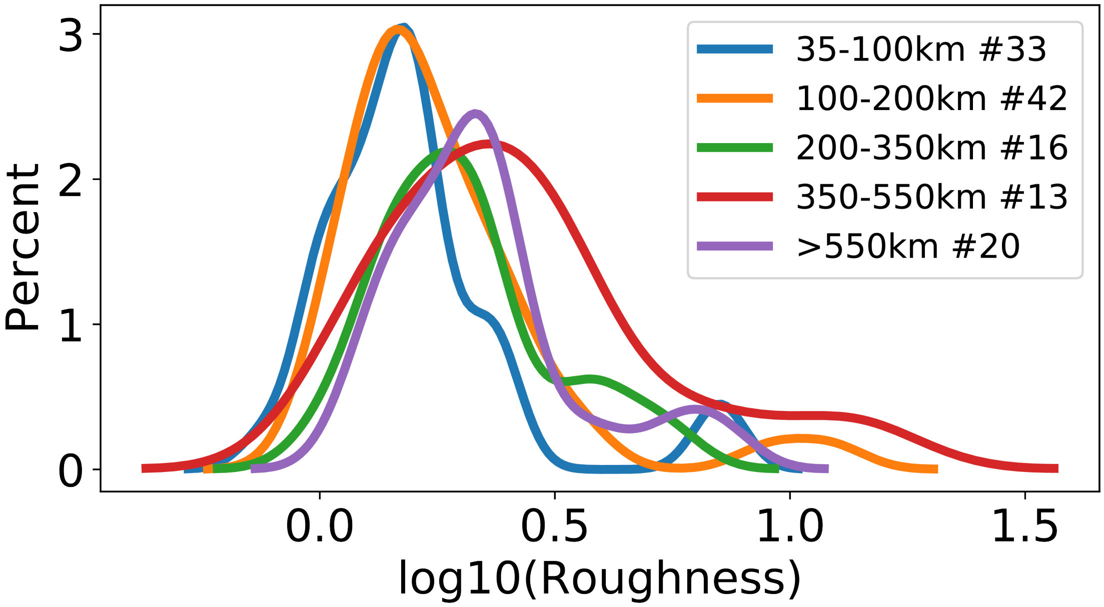

Figure 4.5: Roughness distribution of deep normal faulting events for different depth bins (see legend) determined using kernel density estimates. Non-weighted average roughness estimates are shown.

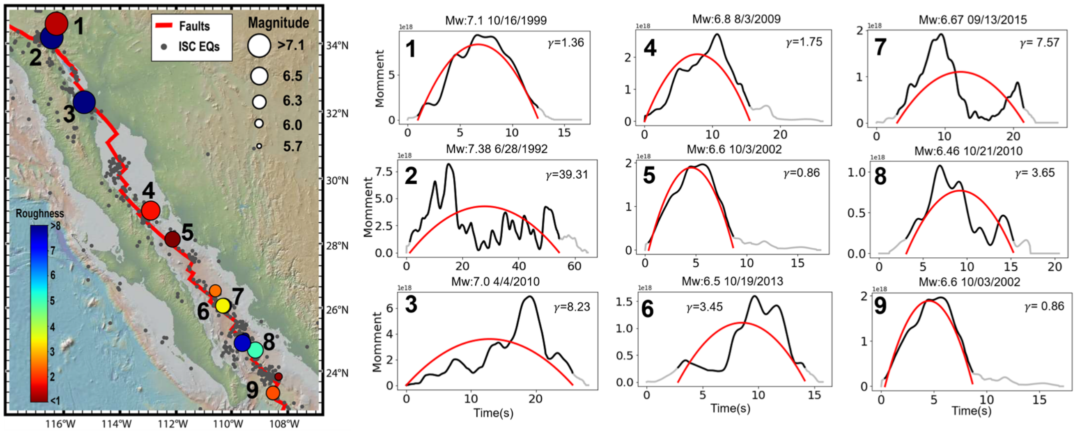

Figure 4.6: Mapview of the strike slip events non-weighted average roughness values in the Gulf of California. ISC earthquake events are plotted in gray and faults are plotted in red (Bird, 2003). Source time functions for numbered events are shown to the right (see figure 2 for description of STFs).

Chapter 5

Quantifying Rupture Characteristics of Microearthquakes in the Parkfield Region

5.1 Abstract

It is well known that large earthquakes often exhibit significant rupture complexity such as well separated subevents and directivity. With improved recording and data processing techniques, small earthquakes have been found to exhibit rupture complexity as well (e.g., Wang et al., 2014). Studying these small earthquakes offer the opportunity to better understand the possible causes of rupture complexities. Specifically, if they are random or are related to fault properties. To better understand the factors that influence rupture complexity behaviors, we examine microearthquakes in the Parkfield area that are recorded by a high-

resolution borehole network. The Parkfield area is chosen because it is a densely studied region with well documented structural and lithological features that the results of this work can be compared to. We quantify earthquake complexity using Source Time Functions (STF) and by their source spectra deviation from Brune-type source models following the method of Uchide and Imanishi (2016). We then compare the spatial distributions of complexity observations and we find good agreement between the two methods. For M>2.6 events, a majority of them are complex for both methods. The spatial locations of complex and simple events tend to concentrate in regions with different creeping rates and fault structure.

5.2 Introduction

Accurate characterization of earthquake rupture processes provides useful information for the understanding of not only the physics of earthquakes, but also fault properties and stress regime. For small to moderate earthquakes, one of the most common methods to characterize their ruptures is through the fitting of their source spectra with a theoretical model. For a simple circular rupture, the farfield displacement spectrum can be explained by omega-square models with a single corner frequency (Brune, 1970). With a few assumptions, it is fairly trivial to obtain estimates of rupture duration, rupture radius, and stress drop based on the corner frequency measured from spectral fitting (Abercrombie, 1995; Ide & Beroza, 2001; Imanishi & Ellsworth, 2006; Baltay et al., 2010; Abercrombie, 2014). A well-known limitation of this method is that it cannot be accurately applied to events that are not simple circular ruptures such as large earthquakes (Atkinson, 1996; Boatwright et al., 1991). If a simple source model is applied to an event with a complex rupture, the estimated source parameter will be biased (Shearer et al., 2019) and the interpretation will likely hinder the advancement of our understanding of rupture processes.

If an earthquakes rupture is complex then the approach most often utilized to estimate its source parameters is finite fault source inversion (Mai & Thingbaijam, 2014). Through these inversions it is possible to obtain the slip distribution for an event in space and time (Hartzell & Heaton, 1986, 1983). In the time domain the temporal evolution of the slip distribution (source-time function) will capture the complexity of the slip distribution to a certain degree by showing multiple pulses, each of which represent different episodes of rupture (Kikuchi & Kanamori, 1982; Vallée & Douet, 2016; Danré et al., 2019). Due to recording limitations and resolution limits due to frequency limitations these methods are usually only be applied to large events. When these methods are applied to small magnitude earthquakes, they reveal levels of complexity similar to those observed for large magnitudes (Ide, 2001; Dreger et al., 2007; Fischer, 2005a; Wang et al., 2014).

Complex rupture processes have been observed to cause these earthquakes' source spectra to deviate from a simple circular model that is commonly used for spectral fitting (McGuire et al., 2002; Atkinson & Silva, 1997; Schneider et al., 1993; Silva et al., 1998). A study by Uchide and Imanishi (2016) found events M3.2-4.0 consistently deviated from the simple model, indicating that some form of rupture complexity exist for small magnitude events. The connection of spectral complexity and complexity observed in the source-time function for a Mw 4 earthquake was recently made by Wu et al. (2019). However, this was only done for a single event, making the link of spectral complexity and time-domain complexity not statistically conclusive, which would require that such observations be made on a sample size of at a minimum 100-250 events depending on the desired confidence level and margin of error.

To better understand the factors that influence rupture complexity behaviors, we examine microearthquakes in the Parkfield area that are recorded by a high-resolution borehole network from 2001-2011. The Parkfield area is chosen because it is a densely studied region with well documented structural and lithological features that the results of this work can be compared to. We characterize events both by their source spectral deviation from a simple model (Uchide & Imanishi, 2016) and by their relative source-time functions (Wang et al., 2014; Wu et al., 2019). In order to better understand the connection between complexity in the time domain and the complexity observed in spectra. We apply the empirical Green's function (EGF) technique in both the time and frequency domains. We then compare the spatial distributions of complexity observations and we find good agreement between the two methods. For M>2.6 events, a majority of them are complex from both methods. Simple events are observed to align with regions where the creeping rate increases and lithology changes have been observed, while complex events tend to occur in regions with more complex fault structures.

5.3 Data

We analyze earthquakes between 2001 and 2011 that are located along a 80 km-long Parkfield fault segment of the San Andreas Fault system (Figure 5.1). We identify target and EGF event pairs using the double difference relocated catalog of Northern California (Waldhauser & Schaff, 2008; Waldhauser, 2009). We treat each cataloged earthquake as a potential target event, and search for suitable EGF events within 400 m radius of the hypocenter and more than 1 magnitude unit lower. The magnitudes are from a spectral-calibrated moment magnitude catalog (Zhang et al., 2019, AGU abstract). We identify 4528 target earthquakes and 7180 EGF events, which will be used for further analysis. For all the selected events, we download triggered waveforms from the 13 borehole stations with 250 Hz sampling rate in the High-Resolution Seismic Network (HRSN) from Northern California Earthquake Data Center (NCEDC). Instrument gain corrections are applied according to the simple instrument response table from NCEDC database. P-wave arrival times are either from catalog phase picks or an auto picker based on 1-D velocity model (Li & Peng, 2016).

5.4 Method

5.4.1 Multiple Spectral Ratio Analysis

One popular method to obtain earthquake source parameters is through analysis of event source spectra. If an earthquake is a simple circular rupture, then its spectra should not significantly deviate from the omega-square source spectra model. To understand if such deviations are common for small magnitude earthquakes, we perform multiple spectral ratio analysis following Uchide and Imanishi (2016) and fit the spectral ratios with an omega-square model (Boatwright, 1978):

$$R_i(f) = \frac{M_0^{Target}}{M_0^{EGF[i]}} \left[\frac{1 + (f/f_c^{EGF[i]})^4}{1 + (f/f_c^{Target})^4} \right]^{1/2} \tag{5.1}$$

in which f is the frequency, f_c is the corner frequency and M_0 is the moment of the "Target" or the ith "EGF" event respectively.

For the P-wave, we calculate event displacement spectra for the vertical channel that begins 0.1 s before the P arrival and extends to 0.5-1 s depending on the

S-arrival time. A noise window of similar length is selected before the P-wave to be used for an estimation of the Signal-to-Noise Ratio (SNR). Only spectra with a minimum SNR $\geq$ 5 between 2 and 60 Hz are used to calculate spectral ratio. EGF and Target event pairs that have spectral ratios from 6 or more stations are used in the following analyses.

For each event pair, corner frequencies and moment ratios are estimated using a grid-search method to minimize the misfit between the observed median stack of the individual ratios (R_i^{obs}) and predicted (R_i^{syn}) ratio obtained from equation 5.1 . We only include those EGF pairs that obtain a 85% variance reduction following Uchide and Imanishi (2016). For target events with 6 or more EGFs that pass this criterion, we estimate the misfit from the omega-square model by taking the median of the residual between the (R_i^{obs}) and predicted (R_i^{syn}) of all EGF pairs (Figure 5.2 a-d). The median misfit emphases the deviations from the predicted model that are common across all EGFs, which can be attributed to the target events source spectra, and suppresses the deviations due to a single EGF's source spectra.

To quantify the misfit observed for each target event, we calculate the peak-to-peak residual ratio, which is defined as ratio of the maximum and minimum residuals of the stack median misfit. The peak to peak ratio is calculated across the frequency range of 2- 50Hz. Based upon the visual inspection of results we find that events with peak-to-peak ratios $\geq$1.6 indicates low misfit from the omega-square model (e.g Figure 5.2 g-h), and are classified as "SR_{Dev} simple". Events with a peak-to-peak ratio of greater than $\geq$1.8 indicates significant deviation from the model (e.g Figure 5.2 e-f), and are classified as "SR_{Dev} complex". Events with peak-to-peak ratios between 1.6 and 1.8 are difficult to attribute to either group and therefore are unclassified.

5.4.2 Relative Source Time Functions

Deconvolution in the time domain results in the moment rate functions of the target event relative to the EGF event at each seismic station, and are commonly referred to as the Relative Source Time Function (RSTF). An event with a simple rupture should have a single pulse RSTF for all stations, with possible pulse width variations due to directivity. If an event contains more than one pulse across multiple stations, this indicates that the rupture could contain multiple subevents and can be referred to as a complex (referred to as compound in Wang et al. (2014)). To estimate RSTF for each target event, we utilize the EGF based time domain forward modeling approach outlined in (Wu et al., 2019). This method, which is fundamentally based on the work of Kikuchi and Kanamori (1982), assumes that the source time function of the target event can be represented as the superposition of multiple Gaussian pulses that can have varying amplitudes and time lags. The method of Wu et al. (2019) is utilized here because it does not limit the number of pulses like other approaches (Tan & Helmberger, 2010; Wang et al., 2014), instead it fits multiple pulses and evaluates their inclusion by the variance reduction in waveform fitting.

In order to prevent the overfitting of the data or the fitting of noise, we place constraints on the frequency range examined through bandpass filtering, window length of data, and duration (T_d) of the RSTF. Due to the varying magnitude range examined in this study, we utilize different constraints for different magnitude ranges, which are presented in Table 5.1. We estimate the RSTF for each event pair examined in the spectral analysis section. We constrain the pulse width based on a theoretical corner frequency estimate from the circular crack model (Eshelby, 1957; Brune, 1970):

$$\Delta\sigma = \frac{7M_0}{16}(\frac{f_c}{k\beta})^3 \tag{5.2}$$

and using the event seismic moment M_0, a constant rupture velocity (β) of 3 km/s, constant stress drop ($\Delta\sigma$) of 2 MPa, and k is 0.372 for the Brune model (Brune, 1970). We set the maximum possible pulse double the theoretical source duration estimated, which is based on the theoretical corner frequency of the target event. We set the smallest possible pulse width to be half the theoretical source duration based on the corner frequencies of the EGF. If either of these values surpass the width allowed by the bandpass filter, we constrain it to that value instead. We allow the pulse width to vary within the constrained range for the first 3 iterations, after which we constrain it to the smallest pulse width observed in first 3 iterations. The maximum number of iterations is 20, and convergence is reached if the following criteria are meet: (1) The first pulse produces a variance reduction of 80%. (2) The next iteration does not improve the overall variance reduction by more than 1.5%.(3) The relative variance reduction improvement is <1.5%. We define relative variance reduction as $VR_n/VR_{n-1} \times 100$ with VR_n representing the variance reduction of the n_{th} iteration.

If the RSTF duration is not well constrained and is set to an excessively long time period RSTF estimates have the possibility to include anomalous pulses due to noise later in the waveform. To prevent this the optimal RSTF duration for each station is found by grid search and testing RSTF durations between 20% and 80% of the time window selected for the data. The RSTF is then calculated for each of these possible durations. The longest duration that improves the overall variance reduction by more than 5% is selected as the optimal RSTF duration.

The RSTF obtained for this duration for that specific station is then used in the analysis. In this analysis we only examine those RSTF that obtain a variance reduction $VR \geq 70\%$.

To measure the complexity of RSTF, we use the variance reduction ratio (R_{VR}) defined as:

$$R_{VR} = VR_{1st}/VR_{final} \tag{5.3}$$

where VR_{1st} is the variance reduction of the first iteration and VR_{last} is the variance reduction of the final iteration. To determine if a target event is complex or simple, we first select the optimal EGF that has the maximum number of stations with valid RSTF among all available EGFs in order to maximize azmithal coverage and exclude EGFs that may have a high number opposite first motions. If more than one EGF fits this criteria we select the EGFs with average overall variance reductions within the top 5%. This is done when possible in order to reduce effects of a station having an anomalous result for a single EGF. Due to the limited number of stations a single anomalous station can led to an event being unclassified. If there is no EGF with more than 5 RSTFs, the target event is considered as unresolvable. We allow target events that have a single EGF that pass this criteria to be analyzed for complexity and therefore obtain more RSTF complexity estimates than the spectral deviation analysis, due to us requiring events analyzed in that method to have ≥ 6 EGFs. The RSTF and its associated variance reduction acts as a measure of similarity between the two. In the spectral analysis we have no such measure, so require more EGFs in order to suppress the possible effects of an EGF with a non-similar radiation pattern to the target.

Then, we use the percentage of RSTF with a $R_{VR} \geq 0.9(\mathrm{R}_{VR90})$ and/or $R_{VR} \geq 0.8(\mathrm{R}_{VR80})$ out of all RSTFs (stations) to classify simple or complex events based on the following criteria:

- Simple events: the percentage of $R_{VR90} \geq 80\%$ and$R_{VR80} \geq 90\%$
- Complex events: the percentage of $R_{VR90} \leq 30\%$ or $R_{VR80} \leq 50\%$

Events that do not meet these criteria are considered unclassified. Four example results obtained from the RSTF analysis are plotted in Figure 5.3.

5.5 Results

From our spectral ratio analysis, we obtain results for 337 events, among them, 186 events are simple, 85 events are complex, and 66 events are unclassified. From the RSTF analysis, we obtain results for 481 events, among them, 222 are simple, 101 are complex and 158 are unclassified. 291 common events are found between the two methods. Of the 114 simple events from RSTF analysis, 99 are classified as SR_{Dev} simple and 15 are classified SR_{Dev} complex. Of the 49 complex events from RSTF analysis, 27 are classified SR_{Dev} complex. This disagreement is reduced when only larger events (M>2) that are within the network are considered: only 2 out of 18 RSTF complex events are classified as SR_{Dev} simple; and only 8 out of the 72 RSTF simple are classified as SR_{Dev} complex. The disagreement for lower magnitude events could be attributed to the lack of resolution. The disagreement of events that fall outside the network could be due to the lack of good azimuthal coverage and example of a unclassified event with this problem is shown in Figure 5.4.

5.6 Discussion

5.6.1 Complexity from spectral and RSTF analyses

The primary limitation of our results is the frequency range being examined. The frequency range where the peak to peak ratio of deviation reaches 1.8 ($PtP_{1.8f}$) increases as the target events magnitude decreases (Figure 5.5 a). At magnitudes of 2.1, $PtP_{1.8f}$ reaches the limit of our observable frequency range, and then remains close to this boundary. In contrast, the $PtP_{1.4f}$ range for a peak to peak ratio of 1.4 continues to steadily decrease with magnitude. This indicates that $PtP_{1.8f}$ for lower magnitudes is beyond our frequency limit and our resolution range, so the capability to classify an event as complex decreases with decreasing magnitude for spectral analysis.

Our resolvable pulse width range has a similar resolution problem. The theoretical pulse width of the EGF event falls below our observable range of 0.02 due to the requirement of 5 samples needed to represent a Gaussian pulse (Figure 5.5 b). We are still able to resolve complexity for the target event, until we pass 2.0-2.2 M range where the target events pulse width is now just 0.03s larger in width than our observable range.

Figure 5.5 assumes a constant stress drop of 3.5 MPa. If a higher stress drop of 10MPa is assumed10 MPa is assumed (Zhang et al. 2019, AGU abstract), then the f_c and our target events pulse width can be even narrower. Based upon these observations, we restrict our results used in the interpretation to be those with $\geq$M2.0 and within the network.

The spectral deviations we observe in our SR_{Dev} results can have multiple causes, but their agreement with those obtained by the RSTF results for >2.0 implies that the bumps on the omega square model are the signatures of the incoherent rupture due to heterogeneities in fault properties and applied stress (e.g., Koyama, 1994). Our findings support those of the previous observations of similar spectral deviations found for larger events M3.2-4.0 by (Uchide & Imanishi, 2016) in the Hamadori are of Japan. The RSTF results also support the findings of events with multiple subevents by Wang et al. (2014) and Fischer (2005b). This indicates that these observations are not unique to the Parkfield region.

At magnitude ranges higher than 2.6M, complex events make up 60-80% percent of all the events that we were able to classify as either complex or simple. This is observed for both RSTF and spectral ratio results (Figure 5.5 c), and indicates that even small magnitude events exhibit surprising levels of complexity. This percentage of simple to complex events is similar to those resolved by Fischer (2005b). These results also place the complexity observed at 2.4-3.5M at Parkfield at similar levels to those observed for >8M events around the world (Danré et al., 2019). The observation of high percentage of complex events for M2-3 events strongly suggest that the assumption that small earthquakes can be described using a single corner frequency (e.g., Boatwright et al., 1991; Atkinson, 1996) is not a reliable assumption.

5.6.2 Spatial patterns of simple and complex events

When examining the spatial pattern of the SR_{Dev} or RSTF classified simple or complex events at Parkfield, certain segments of the fault system often contain more complex events than others (Figure 5.6). Previous observations of spectral complexity in Japan by (Uchide & Imanishi, 2016) found that the deviations in spectra might be due to the event having two corner frequencies. When examining one of our SR_{Dev} complex events we observe similar behavior, which could be interpreted as the occurrence of two corner frequencies in Figure 5.2i. Previous interpretations of events with two corner frequencies in earthquake clusters in Parkfield are predicted by the asperity model to be evidence that an earthquake is caused by the failure of an isolated strong patch that is surrounded by an already broken and preslipped area (e.g., Boatwright, 1988; Johnson & Nadeau, 2002, 2005). The RSTF for these events usually have impulsive initiation representing the slip on the asperity patch and a long tail due to the slip occurring on the preslip region (Johnson & Nadeau, 2005; Dreger et al., 2007). We also find similar behavior for the example event as shown in Figure 5.3 a.

When examining the spatial patterns of complex and simple events between SR_{Dev} (Figure 5.6 a) and RSTF (Figure 5.6 b), similar patterns of complexity across both can be observed. The non-common events between the two methods cause the most divergence between results. This can be due to an event being unclassified in the RSTF results or SR_{Dev} results (e.g. Figure 5.4). The reason for this can be due to directivity making a number of stations appear to be simple, while stations in the direction opposite to directivity will observe complexity. Alternatively, the complexity observed in the event source spectra is due to the failure of a preslip region. To observe such a failure the preslip region needs to produce enough radiated energy to be observed as a second pulse, and then that pulse must account must account for over 10% of the waveform on 70% of stations or over 20% of the waveform on 50% in order for it be classified as complex according to our criteria for RSTF. If it does not produce observable complexity in the waveform then it will not be present in the RSTF model. Due to these reasons, the RSTF will only capture the complexity of events with strong abrupt changes in slip history. All of these factors make it difficult to definitively determine the cause of the contrasting results. That being said the complex events found by the spectral deviation method represent events whose estimated corner frequencies might be erroneously estimated using a simple circular model.

The common events with the same classification from the two methods provide the most stable set of results to interpret (Figure 5.6 c-e). A region with a high level of simple events occurs in a concentrated area roughly 5 km long, located at about 2.5 km SE of the 1966 M6 earthquake (Figure 5.6 c-e orange box). A change in lithology to serpentine and talc of on the eastern side of the fault have been observed to start to occur around this area or to the NW of it (Irwin & Barnes, 1975; Moore & Rymer, 2007) and this area is also where silica-saturated hydrothermal fluids have been interpreted to be migrating (Becken et al., 2008, 2011). This region is also where high levels of stress are being concentrated with the fault segment to the NW of it experiencing long term deformation (Perrin et al., 2019). This cluster contains a large number of repeating earthquakes indicating that these events are consistently occurring on the same fault patches, so they likely could represent single asperity failures (Rubinstein et al., 2012). This area is also the location of a transition from a high post seismic creep of 70 cm to its SW to a 20 cm at the clusters location by (Barbot et al., 2009) after the 2004 Mw6. This indicates that this area was likely concentrating a large amount of stress, which was being released by these events. The complex events within this area are separated from one another by a 100-200 m lateral distance and occur on two separate faults (Figure 5.6 c,e). The spacing between them could be a constraint based upon geology or a structural constraint such as the location of asperities and the spacing between them. The temporal patterns of these events we could not interpret due to do not having a significant number of classified events after 2006 to examine.

5.7 Conclusion

The findings of this study indicate that rupture complexity exists in small (M<3) magnitude events. This complexity can be observed both in the slip history of the event and in its source spectra. This has important implications for the study of source processes of earthquakes, since it reveals that use of simple circular rupture model for small events might not be accurate assumption. What controls the spatial pattern of this complexity appears to be related to geologic and structural features observed by past studies. Future research should focus on better linking frequency and time domain analysis of complexity and understanding how geologic or specific rupture processes manifest in each of them.

5.8 Acknowledgments

We are grateful to J. Zhang and R. Abercrombie for information about their work on these Parkfield earthquakes and the HRSN data. The HRSN data used in this study were accessed through the NCEDC (http://ncedc.org/hrsn/).

References

Abercrombie, R. (1995). earthquake source scaling relationships from -1 to 5 Ml using seismograms recorded at 2.5-km depth. *J. Geophys. Res.*, *100*(B12), 24015–24036.

Abercrombie, R. (2014). Stress drops of repeating earthquakes on the San Andreas Fault at Parkfield. *Geophysical Research Letters*, *41*(24), 8784–8791. doi: 10.1002/2014GL062079

Atkinson, G. M. (1996). The high-frequency shape of the source spectrum for earthquakes in eastern and western Canada. *Bulletin of the Seismological Society of America*, *86*(1 SUPPL. A), 106–112.

Atkinson, G. M., & Silva, W. (1997). An empirical study of earthquake source spectra for California earthquakes. *Bulletin of the Seismological Society of America*, *87*(1), 97–113.

Baltay, A., Prieto, G., & Beroza, G. C. (2010). Radiated seismic energy from coda measurements and no scaling in apparent stress with seismic moment. *Journal of Geophysical Research: Solid Earth*, *115*(8), 1–12. doi: 10.1029/2009JB006736

Barbot, S., Fialko, Y., & Bock, Y. (2009, 7). Postseismic deformation due to the M w 6.0 2004 Parkfield earthquake: Stress-driven creep on a fault with spatially variable rate-and-state friction parameters. *Journal of Geophysical Research*, *114*(B7), B07405. doi: 10.1029/2008JB005748

Becken, M., Ritter, O., Bedrosian, P. A., & Weckmann, U. (2011). Correlation between deep fluids, tremor and creep along the central San Andreas fault. *Nature*. doi: 10.1038/nature10609

Becken, M., Ritter, O., Park, S. K., Bedrosian, P. A., Weckmann, U., & Weber, M. (2008). A deep crustal fluid channel into the San Andreas Fault system near Parkfield, California. *Geophysical Journal International*. doi: 10.1111/j.1365-246X.2008.03754.x

Boatwright, J. (1978). Detailed spectral analysis of two small New York State earthquakes. *Bulletin of the Seismological Society of America*.

Boatwright, J. (1988). The Seismic Radiation From Composite Models of Faulting. *Society*, *78*(2), 489–508.

Boatwright, J., Fletcher, J. B., & Fumal, T. E. (1991). AA general inversion scheme for source, site, and propagation characteristics using multiply recorded sets of moderate-sized earthquakes. *Bulletin of the Seismological Society of America*, *81*(5), 1754–1782.

Brune, J. N. (1970, 9). Tectonic stress and the spectra of seismic shear waves from earthquakes. *J. Geophys. Res.*, *75*(26), 4997–5009. Retrieved from `http://doi.wiley.com/10.1029/JB075i026p04997` doi: 10.1029/JB075i026p04997

Danré, P., Yin, J., Lipovsky, B. P., & Denolle, M. A. (2019). Earthquakes Within Earthquakes: Patterns in Rupture Complexity. *Geophysical Research Letters*, *46*(13), 7352–7360. doi: 10.1029/2019GL083093

Dreger, D., Nadeau, R. M., & Chung, A. (2007). Repeating earthquake finite source models: Strong asperities revealed on the San Andreas fault. *Geophysical Research Letters*, *34*(23), 1–5. doi: 10.1029/2007GL031353

Eshelby, J. D. (1957). The determination of the elastic field of an ellipsoidal inclusion, and related problems. *Proc. R. Soc. London, Ser. A,*, *241*, 376–396.

Fischer, T. (2005a). Modelling of multiple events using empirical Green's functions: Method, application to swarm earthquakes and implications for their rupture propagation. *Geophysical Journal International*, *163*(3), 991–1005. doi: 10.1111/j.1365-246X.2005.02739.x

Fischer, T. (2005b). Modelling of multiple events using empirical Green's functions: Method, application to swarm earthquakes and implications for their rupture propagation. *Geophysical Journal International*, *163*(3), 991–1005. doi: 10.1111/j.1365-246X.2005.02739.x

Hartzell, S., & Heaton, T. (1983). Inversion of strong ground motion and teleseismic waveform data for the fault rupture history of the 1979 Imperial Valley, California, earthquake. *Bulletin of the Seismological Society of America*.

Hartzell, S., & Heaton, T. (1986). Rupture history of the 1984 Morgan Hill, California, earthquake from the inversion of strong motion records. *Bulletin of the Seismological Society of America*.

Ide, S. (2001). Complex source processes and the interaction of moderate earthquakes during the earthquake swarm in the Hida-Mountains, Japan, 1998. *Tectonophysics*, *334*(1), 35–54. doi: 10.1016/S0040-1951(01)00027-0

Ide, S., & Beroza, G. (2001). Does apparent stress vary with earthquake size? *Geophys. Res. Lett.*, *28*(17), 3349–3352.

Imanishi, K., & Ellsworth, W. L. (2006). Source scaling relationships of microearthquakes at Parkfield, CA, determined using the SAFOD Pilot Hole Seismic Array. *Earthquakes: Radiated Energy and the Physics of Faulting, Geophys. Monogr. Ser.,*, *170*, 81–90. doi: 10.1029/170GM10

Irwin, W. P., & Barnes, I. (1975). Effect of geologic structure and metamorphic fluids on seismic behavior of the San Andreas fault system in central and northern California. *Geology*. doi: 10.1130/0091-7613(1975)3⟨713:EOGSAM⟩2.0.CO;2

Johnson, L. R., & Nadeau, R. M. (2002). Asperity model of an earthquake: Static Problem. *Bulletin of the Seismological Society of America*, *92*(2), 672–686.

Johnson, L. R., & Nadeau, R. M. (2005). Asperity model of an earthquake: Dynamic problem. *Bulletin of the Seismological Society of America*, *95*(1), 75–108. doi: 10.1785/0120030093

Kikuchi, M., & Kanamori, H. (1982). Inversion of complex body waves. *Bull. Seismol. Soc. Am.*, *72*(2), 491–506. doi: 10.1016/0031-9201(86)90048-8

Koyama, J. (1994). General Description of the Complex Faulting Process and Some Empirical Relations in Seismology. *Journal of Physics of the Earth*, *42*(2), 103–148. Retrieved from `http://joi.jlc.jst.go.jp/JST.Journalarchive/jpe1952/42.103?from=CrossRef` doi: 10.4294/jpe1952.42.103

Li, Z., & Peng, Z. (2016). An Automatic Phase Picker for Local Earthquakes with Predetermined Locations: Combining a Signal-to-Noise Ratio Detector with 1D Velocity Model Inversion. *Seismol. Res. Lett.*, *87*(6). doi: 10.1785/0220160027

Mai, P. M., & Thingbaijam, K. K. S. (2014). SRCMOD: An Online Database of Finite-Fault Rupture Models. *Seismological Research Letters*, *85*(6), 1348–1357. doi: 10.1785/0220140077

McGuire, J. L., Zhao, L., & Jordan, T. H. (2002). Predominance of unilateral rupture for a global catalog of large earthquake. *Bulletin of the Seismological Society of America*, *92*(8), 3309–3317. doi: 10.1785/0120010293

Moore, D. E., & Rymer, M. J. (2007). Talc-bearing serpentinite and the creeping section of the San Andreas fault. *Nature*, *448*(7155), 795–797. doi: 10.1038/nature06064

Perrin, C., Waldhauser, F., Choi, E., & Scholz, C. H. (2019). Persistent fine-scale fault structure and rupture development: A new twist in the Parkfield, California, story. *Earth and Planetary Science Letters*, *521*, 128–138. Retrieved from `https://doi.org/10.1016/j.epsl.2019.06.010` doi: 10.1016/j.epsl.2019.06.010

Rubinstein, J. L., Ellsworth, W. L., Chen, K. H., & Uchida, N. (2012). Fixed recurrence and slip models better predict earthquake behavior than the time- and slip-predictable models: 1. Repeating earthquakes. *Journal of Geophysical Research: Solid Earth*, *117*(2), 1–23. doi: 10.1029/2011JB008724

Schneider, J. F., Silva, W. J., & Stark, C. (1993). Ground Motion Model for the 1989 M 6.9 Loma Prieta Earthquake Including Effects of Source, Path, and Site. *Earthquake Spectra*. doi: 10.1193/1.1585715

Shearer, P. M., Abercrombie, R. E., Trugman, D. T., & Wang, W. (2019). Comparing EGF Methods for Estimating Corner Frequency and Stress Drop From P Wave Spectra. *Journal of Geophysical Research: Solid Earth*, *124*(4), 3966–3986. doi: 10.1029/2018JB016957

Silva, W. J., Wong, I. G., & Darragh, R. B. (1998). Engineering characterization of earthquake strong ground motions in the Pacific Northwest. *US Geological Survey Professional Paper*.

Tan, Y., & Helmberger, D. (2010). Rupture directivity characteristics of the 2003 big bear sequence. *Bulletin of the Seismological Society of America*, *100*(3), 1089–1106. doi: 10.1785/0120090074

Uchide, T., & Imanishi, K. (2016). Small earthquakes deviate from the omega-square model as revealed by multiple spectral ratio analysis. *Bulletin of the Seismological Society of America*, *106*(3), 1357–1363. doi: 10.1785/0120150322

Vallée, M., & Douet, V. (2016). A new database of source time functions (STFs) extracted from the SCARDEC method. *Physics of the Earth and Planetary Interiors*, *257*, 149–157. doi: 10.1016/j.pepi.2016.05.012

Waldhauser, F. (2009). Near-real-time double-difference event location using long-term seismic archives, with application to northern California. *Bulletin of the Seismological Society of America*. doi: 10.1785/0120080294

Waldhauser, F., & Schaff, D. P. (2008). Large-scale relocation of two decades of Northern California seismicity using cross-correlation and double-difference methods. *Journal of Geophysical Research: Solid Earth*. doi: 10.1029/2007JB005479

Wang, E., Rubin, A. M., & Ampuero, J.-P. (2014, 5). Compound earthquakes on a bimaterial interface and implications for rupture mechanics. *Geophysical Journal International*, *197*(2), 1138–1153. Retrieved from `http://academic.oup.com/gji/article/197/2/1138/620011/Compound-earthquakes-on-a-bimaterial-interface-and` doi: 10.1093/gji/ggu047

Wu, Q., Chen, X., & Abercrombie, R. E. (2019). Source Complexity of the 2015 Mw 4.0 Guthrie, Oklahoma Earthquake. *Geophysical Research Letters*, *46*(9), 4674–4684. doi: 10.1029/2019GL082690

Magnitude	Filter (Hz)	Window Length (s)	Pulse Width (s)
> 3.5	0.5-20	1.2	0.4-0.02
$3.5 - 3$	0.5-20	1	0.4-0.02
$3 - 2.5$	0.5-50	0.8	0.2-0.02
< 2.5	0.5-50	0.6	0.2-0.02

Table 5.1: Parameters used in the ASTF inversion process.

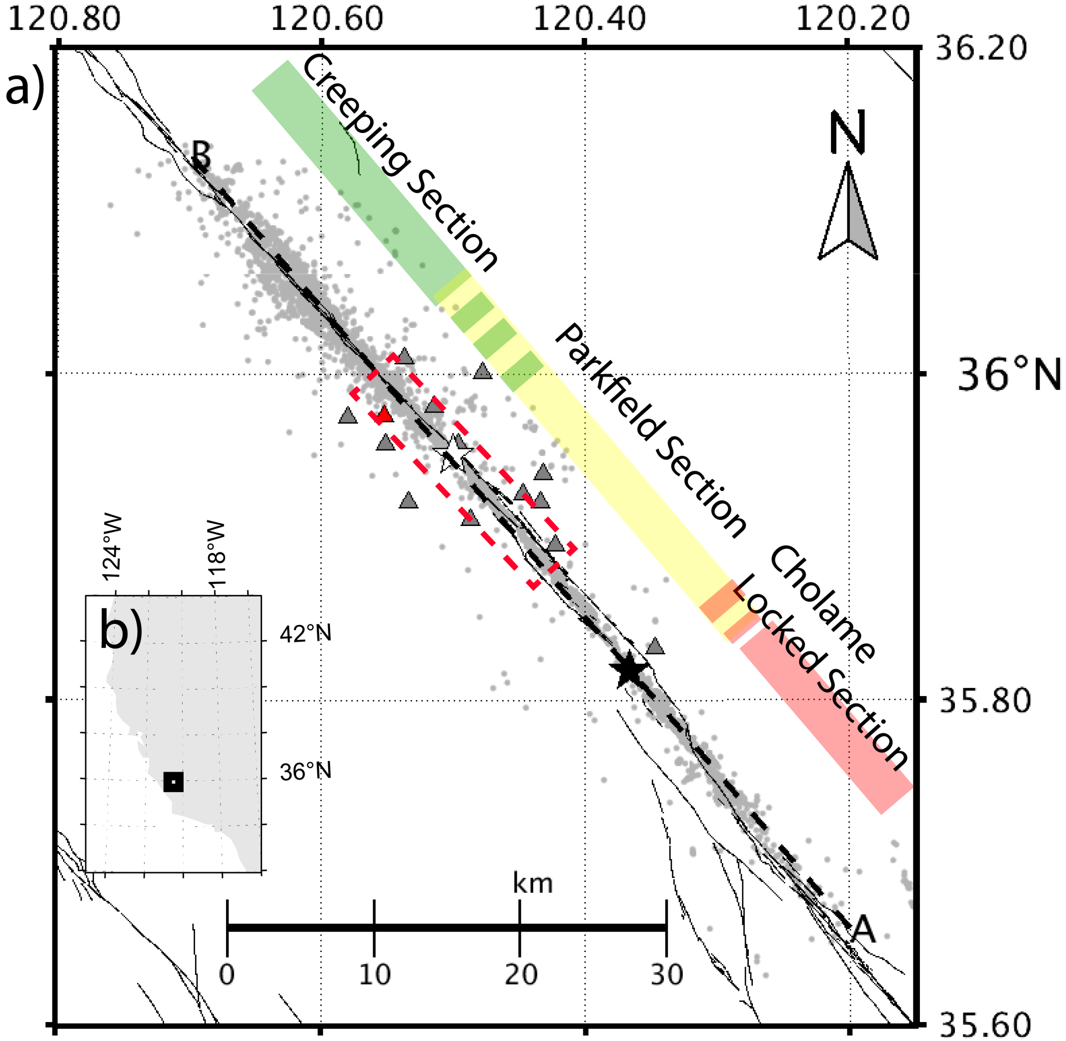

Figure 5.1: (a) Parkfield study area with (b) inset map of overall region with study area marked by black box. All earthquakes in the relocated catalog are shown as gray dots and thin black lines are are Quaternary fault traces from the (U.S. Geological Survey and California Geological Survey, 2006). Full cross section length is shown as dashed black line between points A and B. The 1966 M6 earthquake (black star), 2004 M6 earthquake (white star) and stations used in the analysis are plotted (gray triangles) with SAFOD also being shown (red triangle). Area considered to be within the network is shown by red dashed box.

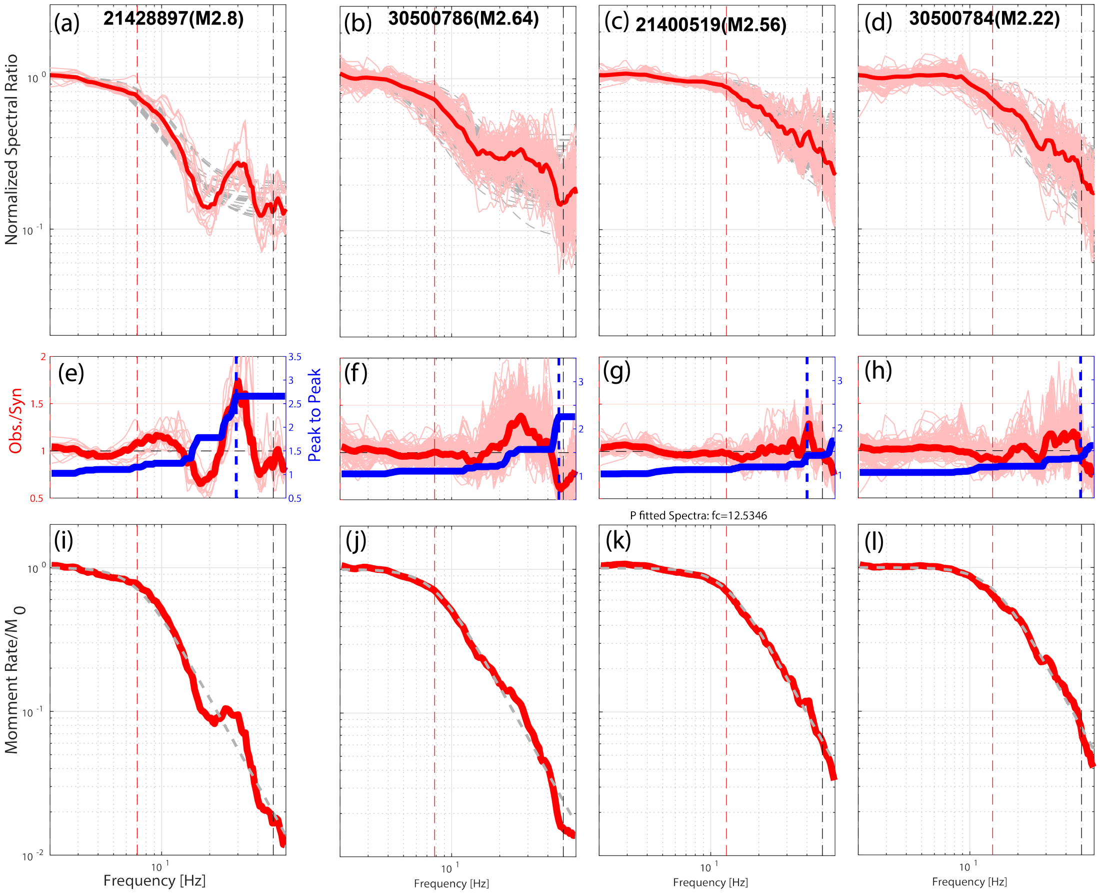

Figure 5.2: Results of the spectral ratio analysis for four selected earthquakes. (a-d) Spectral ratios of individual empirical Green's function events (thin light red lines), and their medium stack (dark red line), which are normalized by the moment ratio. Synthetic fits to each EGF spectral ratio are plotted in gray. (a-b) are considered complex events, while (c-d) are considered complex.) (e-h) Ratios of the spectral ratios from the observed data to the synthetic curves (thin-light red lines) and their median stack (dark red line). The peak to peak ratio calculated from 2 to each frequency range is plotted in blue, maximum value obtained is shown as blue dashed line. (i)-(l) Gray line is the synthetic omega square model for the target event based median fc estimate from all EGFs. Red line is the synthesized source spectra created by multiplying omega-square model by the median of the residual spectra in (e-h) and then normalizing it by the target events moment.

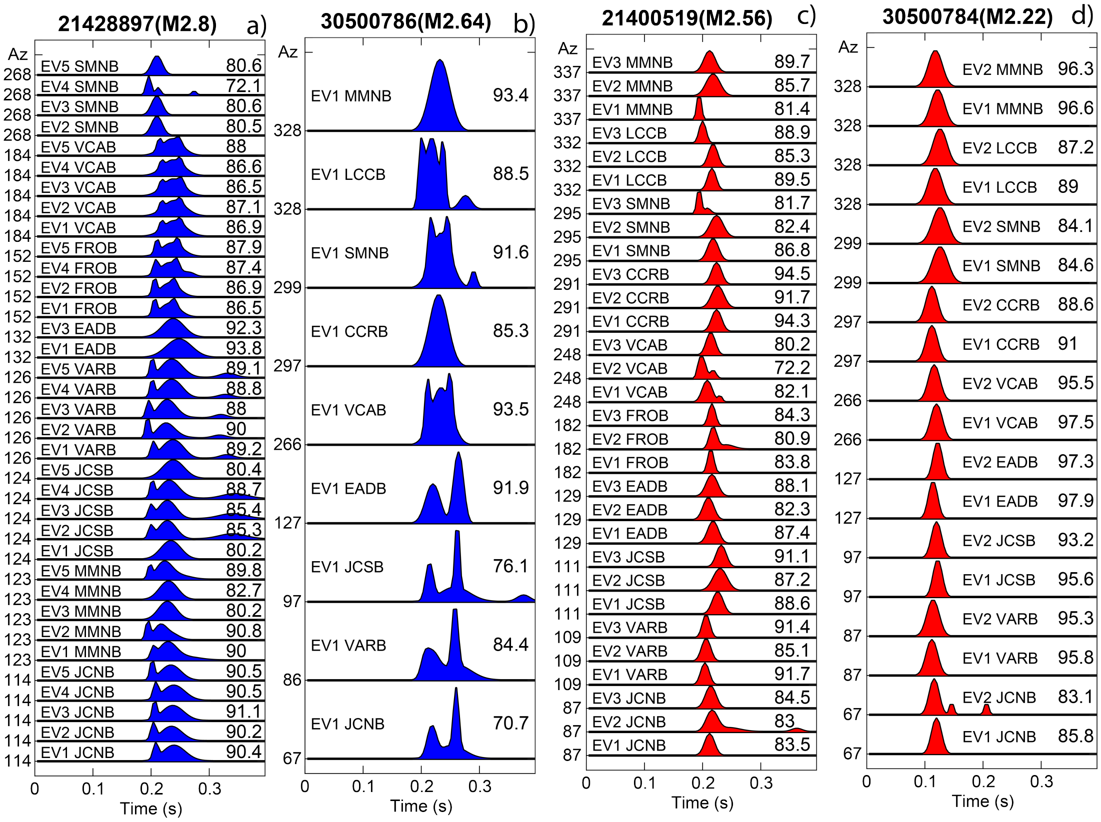

Figure 5.3: (a-d) RSTF's sorted by azimuth that were obtained for 4 events with (a-b) defined as complex and (c-d) defined as simple. Values at the far right of the figure are the final variance reductions obtained for each RSTF and the text in each box denotes the EGF and the station.

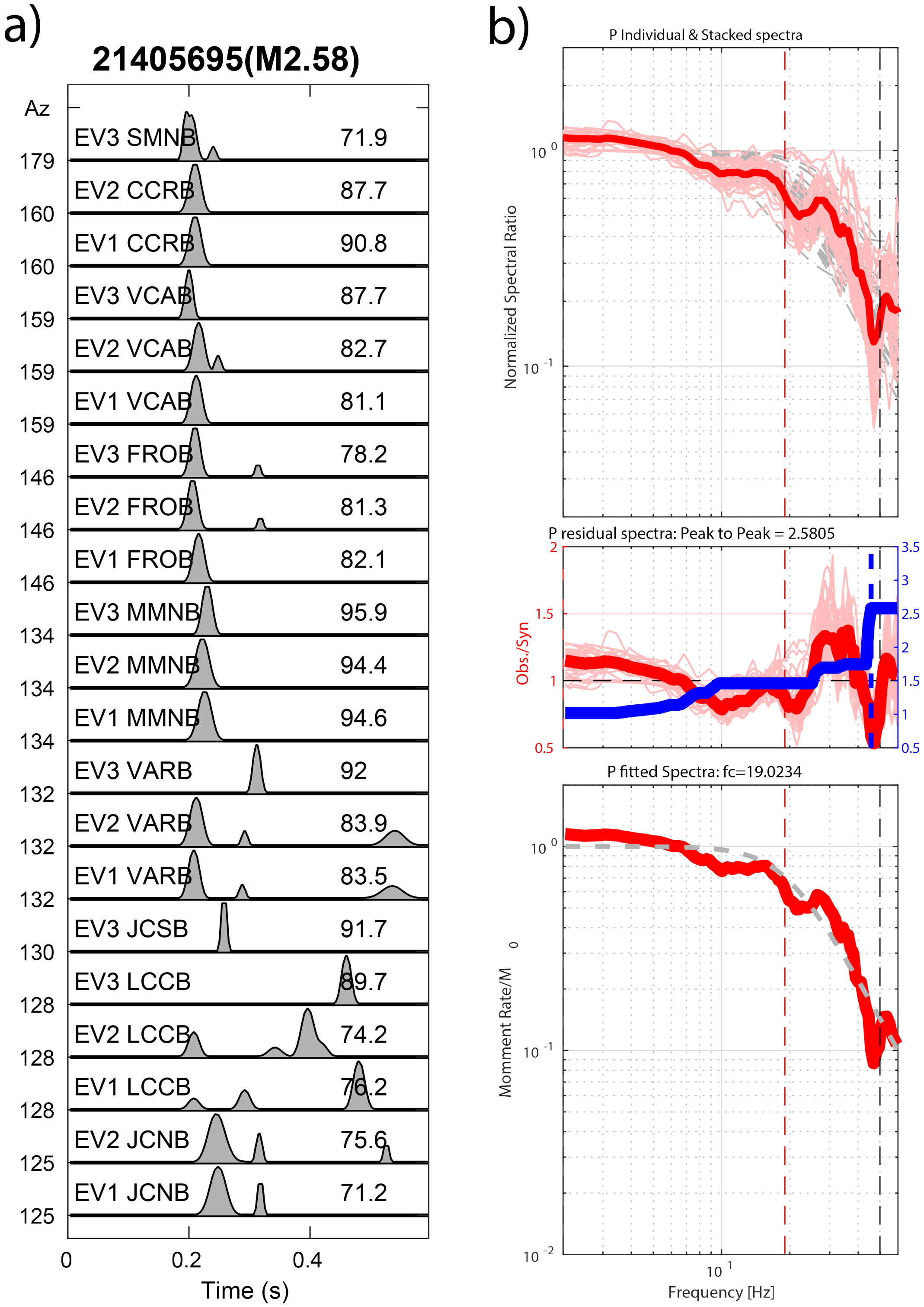

Figure 5.4: Example of a poorly constrained RSTF event. (a) RSTF (see description in Figure 5.3) and (b) spectral analysis (see description in Figure 5.3) .

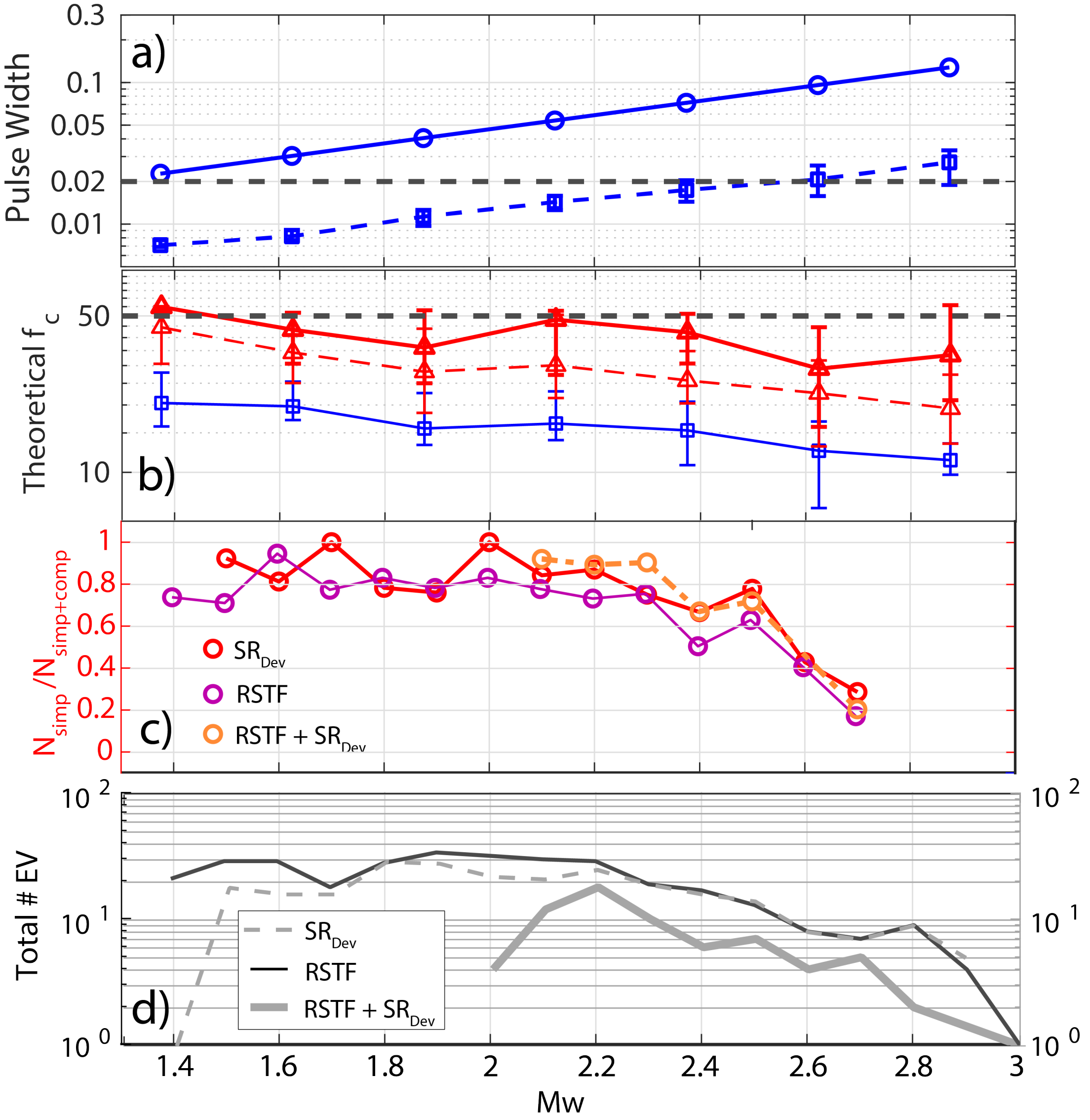

Figure 5.5: a) Resolution of detecting complexity in spectra for different magnitude bins. Fc estimates obtained from spectral ratios (blue line), frequency where peak to peak ratio reaches 1.4 (red dashed line), and 1.9 (solid red line) in relation to the limit of fitted frequency range at 50 Hz (black dashed line). 80th and 20th percentiles of each magnitude bin are denoted by error bars. (b) Pulse width resolution limits. Theoretical pulse width of target events in magnitude bin (solid blue line) and of EGFs (dashed blue line) used for those target events in based upon theoretical corner frequency obtained from event magnitude, assumed stress drop of 3.5 MPa and rupture velocity of 2 km/s.(c) Ratio of simple to simple+complex estimates for the different methods. (d) Total number of events that have a estimate of complextity (e.g. Simple, complex, unclassified).

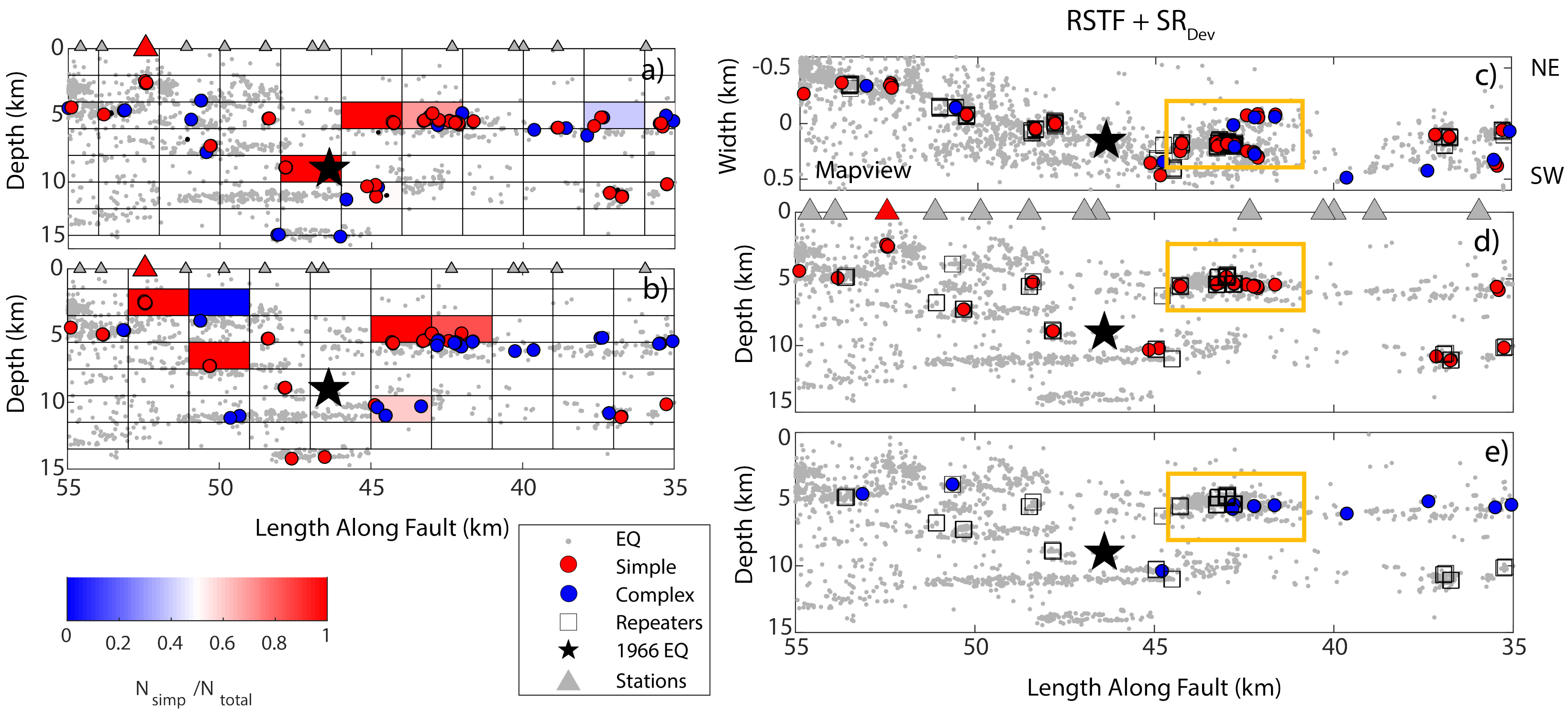

Figure 5.6: Classified earthquakes from (a) RSTF (>M2.0), SR_{Dev} (>M2.0) (b), and those who's classification agrees across both (c-e). Grids with 5 or more classified events are filled in according to ratio of simple events to the total number of classified events in a-b, and individual events are plotted as colored dots. In the common results the mapview and the simple depth(d) and complex (e) depth views are shown separately. All earthquakes in the relocated catalog are shown as gray dots. The 1966 M6 earthquake (black star), and stations used in the analysis are plotted (gray triangles) with SAFOD also being shown (red triangle) and repeating events from Rubinstein et al. (2012) are shown as squares. Group of events discussed in the paper are outlined by orange box

Chapter 6

Conclusion

6.1 Main Results

This thesis has examined earthquake source processes across a broad spectrum of magnitude ranges in order to deepen our understanding of the factors that control them and if such controls extend across magnitude scales. In the previous chapters I have presented the following findings:

- Through the usage of multiple methods and data types it is possible to isolate the effects of fault structure and past events on earthquake source proprieties from those due to method. The usage of multiple methods instead of trusting the results of a single method, which is what is currently done, should become common practice in order to avoid erroneous interpretations.
- Earthquake ruptures for both large and small magnitude show consistent rupture behaviors that vary by region and depth.
- Complex multi-phase ruptures occur across magnitudes and can be observed

> in small magnitude earthquakes. What controls these complexities stays consistent across magnitudes, though their scale changes.

As explained in the introduction understanding the source processes of earthquakes is vital to our ability to quantify hazard. Being able to study small earthquake ruptures and using them as analogs for large earthquakes gives us a wider array of data to examine.

In **Chapter 1**, I analyze the 2011 induced earthquake sequence in Prague, OK. Using a variety of methods I am able to resolve those patterns in source parameter estimates that can be attributed to fault properties or triggering behavior from those that are due to data and method. I find that prior slip on a fault reduces the observed stress drops for aftershocks. Different faults within the sequence exhibit differing stress drop levels indicating fault structure playing an important role in controlling source parameters. The most important finding is that certain patterns I observe can be attributed to method and without using multiple methods for verification such observations would have been presented as being geologically or source related. This suggests that the usage of multiple methods for source parameter verification needs to be encouraged.

In **Chapter 2**, I study the rupture processes of a 2015 Mw 4.1 earthquake in Guthrie, Oklahoma. From the analysis of this event I observe that its rupture is highly heterogeneous and is affected by the locations and rupture areas of prior seismicity. In order to understand the role that fault properties might play in controlling the rupture I compare my results to events within the same region and to those outside of it with similar styles of rupture and triggering process. Our findings from this analysis indicate that earthquake ruptures in the Central U.S. have significantly more heterogeneous slip distributions than other regions. This consistency within the Central U.S region indicates that fault properties and their heterogeneity varies by region and this variation has an impact on earthquake rupture.

In **Chapter 3**, I examine the rupture complexity of earthquakes around the world by measuring the roughness of their Source Time Functions. Through this analysis I find that ruptures vary in complexity by fault type, depth and region. Observations of reverse faulting complexity align with the coupling of faults, which is partially controlled by the subducted plates seafloor roughness. The change in complexity for deep normal events is controlled by changes in rock behavior with depth. Strike slip earthquakes are controlled by both geologic features, and stress heterogeneity within the region I examined. All of these observations support fault properties as one of the major drivers of rupture complexity, but the cause of this complexity varies by region.

In **Chapter 4**, I examine microearthquake rupture complexity at the San Andreas Parkfield fault segment. I find that methods based in the time domain and in the frequency domain are both able to observe rupture complexity, but this accuracy is highly dependent on the bandwidth of the recorded waveforms. I observe high levels of rupture complexity for events above our resolution limit, but almost none for those below it. The most important finding of this study is that small events can have complex ruptures and I can observe them in both the time and frequency domain. Another is that they appear to have preferred location along the fault surface, which are likely linked to changes in fault properties.

6.2 Future Research Directions

The findings presented in this study have important implications for estimates of source parameters and the study of earthquake ruptures. They offer a number of future research directions that could help in verifying results or deepening our understanding of earthquake ruptures.

The accuracy of source parameter estimates obtained from an events source spectra depends at the very core that they fit the simple circular rupture model. Our analysis of small earthquakes at Parkfield seems to indicate that a large number of small events are complex and therefore don't fit these assumption. Attempts to fit such events with a simple model will likely produce source estimates with a high degree of error. Due to these events being so small and limited station coverage available detailed analysis like Finite Fault models might be out of reach at this point and time.

A potential alternative for estimating fault geometry could be based on Source Time Functions and the modeling of the subevents observed within them as presented in Wu et al. (2019). One could determine the stress drop for each of the subevents independently based upon their moment and duration and then see if their combined synthetic spectrum matches the observed complex spectrum. Another possible method for an accurate source parameter estimate would be the second moment method detailed in McGuire (2017) and McGuire and Kaneko (2018). The second moment method has been shown to allow the direct estimation of an earthquakes length, width, duration and rupture directivity. It does require a Green's Function for the estimation of a set of apparent durations and then knowledge of the local velocity structure to obtain estimates of an earthquakes second moment from these durations. This method has been shown to be effective at estimating the source properties of events as low as magnitude 2.0 (e.g., Fan & McGuire, 2018). Recently attempts have been made to make this sort of analysis semiautomated and has been able to perform estimates on M3.5-5.2 earthquakes (Meng et al., 2020).

These type of studies are going to be highly dependent on the geometry of the seismic recording network. However with the increase in dense nodal deployments (e.g., F.-C. Lin et al., 2013; Fan & McGuire, 2018; Dougherty et al., 2019) and the development of fiber optic recording networks (Lindsey et al., 2017) in the future dense station coverage maybe become more widely available. The increase of station coverage and the increasing recording rates of seismic stations will increase our ability to observe complexity for even smaller events. Studies are already being performed using incredibly high sample rates to study small earthquakes (e.g. The DOEs Enhanced Geothermal System Project), which are recording events with 100kHz sampling rate stations (Schoenball et al., 2019). Due to these developments in near future the application of more precise measurements of earthquake source parameters could be applied to even smaller magnitudes.

Even with advancements in our ability to observe rupture processes our current analysis of small complex events is rather lacking. The repeating events observed at Parkfield which were observed to have varying stress drop or moments for the same asperity have been the subject of intense modeling. These modeling studies have primarily focused on reproducing these earthquakes observed moment, stress drop, and occurrence interval (Y. Y. Lin & Lapusta, 2018; Chen & Lapusta, 2009; Lui & Lapusta, 2018). What has not been extensively studied is if the behavior modeled for such events mimics the observed spectra or Source Time Functions for these earthquakes. The connection of these two observations to models might help improve our understanding of what behavior is responsible for the observed behavior in each.

The connection of source parameters and modeling will only go so far in verifying the cause of observed source parameters or rupture complexity. For this reason lab scale studies might offer a unique opportunity to study the rupture properties of small earthquakes and their sub-events. These experiments will provide information that in the real world I often due not have such as direct field measurements of relevant fault properties such as stress state and friction. Such analyses could be done with lab scale machines that allow for only the partial propagation of a rupture in a rock block (Ke et al., 2018; Mclaskey & Yamashita, 2017). Applying source parameter estimation to lab scale studies will also help expose the deficiencies in our current methods to a greater degree and allow for their improvement. It will also help define which features of a rupture these methods can actually observe, and might help limit the over interpretation of source parameter results.

References

Chen, T., & Lapusta, N. (2009). Scaling of small repeating earthquakes explained by interaction of seismic and aseismic slip in a rate and state fault model. *Journal of Geophysical Research-Solid Earth*, *114*, 12. doi: B0131110.1029/2008jb005749

Dougherty, S. L., Cochran, E. S., & Harrington, R. M. (2019, 8). The LArge-n Seismic Survey in Oklahoma (LASSO) Experiment. *Seismological Research Letters*, 1–7. Retrieved from `https://pubs.geoscienceworld.org/ssa/srl/article/572987/The-LArgen-Seismic-Survey-in-Oklahoma-LASSO` doi: 10.1785/0220190094

Fan, W., & McGuire, J. J. (2018, 8). Investigating microearthquake finite source attributes with IRIS Community Wavefield Demonstration Experiment in Oklahoma. *Geophysical Journal International*, *214*(2), 1072–1087. doi: 10.1093/gji/ggy203

Ke, C. Y., McLaskey, G. C., & Kammer, D. S. (2018). Rupture Termination in Laboratory-Generated Earthquakes. *Geophysical Research Letters*, *45*(23), 784–12. doi: 10.1029/2018GL080492

Lin, F.-C., Li, D., Clayton, R. W., & Hollis, D. (2013, 7). High-resolution 3D shallow crustal structure in Long Beach, California: Application of ambient noise tomography on a dense seismic array. *GEOPHYSICS*, *78*(4), Q45-Q56. doi: 10.1190/geo2012-0453.1

Lin, Y. Y., & Lapusta, N. (2018). Microseismicity Simulated on Asperity-Like Fault Patches: On Scaling of Seismic Moment With Duration and Seismological Estimates of Stress Drops. *Geophysical Research Letters*, *45*(16), 8145–8155. doi: 10.1029/2018GL078650

Lindsey, N. J., Martin, E. R., Dreger, D. S., Freifeld, B., Cole, S., James, S. R., … Ajo-Franklin, J. B. (2017). Fiber-Optic Network Observations of Earthquake Wavefields. *Geophysical Research Letters*. doi: 10.1002/2017GL075722

Lui, S. K. Y., & Lapusta, N. (2018). Modeling high stress drops, scaling, interaction, and irregularity of repeating earthquake sequences near Parkfield. *Journal of Geophysical Research: Solid Earth*(1), 854–879. Retrieved from `http://doi.wiley.com/10.1029/2018JB016472` doi: 10.1029/2018JB016472

McGuire, J. J. (2017). A MATLAB Toolbox for Estimating the Second Moments of Earthquake Ruptures. *Seismological Research Letters*, *88*(2A), 371–378. doi: 10.1785/0220160170

McGuire, J. J., & Kaneko, Y. (2018). Directly estimating earthquake rupture area using second moments to reduce the uncertainty in stress drop. *Geophysical Journal International*, *214*(3), 2224–2235. doi: 10.1093/GJI/GGY201

Mclaskey, G. C., & Yamashita, F. (2017). Slow and fast ruptures on a laboratory fault controlled by loading characteristics. *Journal of Geophysical Research: Solid Earth*, *122*(5), 3719–3738. doi: 10.1002/2016JB013681

Meng, H., McGuire, J. J., & Ben-Zion, Y. (2020, 4). Semiautomated Estimates of Directivity and Related Source Properties of Small to Moderate Southern California Earthquakes Using Second Seismic Moments. *Journal of Geophysical Research: Solid Earth*, *125*(4), 1–21. doi: 10.1029/2019JB018566

Schoenball, M., Ajo-Franklin, J., Blankenship, D., Cook, P., Dobson, P., Guglielmi, Y., . . . the EGS Collab Team (2019). Microseismic monitoring of meso-scale stimulations for the DOE EGS Collab project at the Sanford Underground Research Facility. In *44th workshop on geothermal reservoir engineering.*

Wu, Q., Chen, X., & Abercrombie, R. E. (2019). Source Complexity of the 2015 Mw 4.0 Guthrie, Oklahoma Earthquake. *Geophysical Research Letters*, *46*(9), 4674–4684. doi: 10.1029/2019GL082690